ISSN 2744-2640
e-ISSN 2744-2659
JST&M, Vol. 5
www.fipn.unze.ba
08

Journal of **Sustainable Technologies and Materials**

Zenica, June 2025

Journal of Sustainable Technologies and Materials (ISSN 2744-2640)
Vol. 5, No. 8(2024), 1 – 66

Published by
The University of Zenica, Faculty of Engineering and Natural Sciences

Editorial office
Travnička cesta 1,72000 Zenica
Bosnia and Herzegovina
Phone: +387 32 403 468
Email: jstm@unze.ba
Website: https://www.fipn.unze.ba

For submission instructions, manuscript submission, and additional information, please visit https://www.fipn.unze.ba/.

Computer design
Safet Hamedović, University of Zenica, Faculty of Engineering and Natural Sciences

Cover design:
Admir Velić

Printed by „Štamparija Fojnica" D.D.
Fojnica, B&H, in June 2025

Journal of Sustainable Technologies and Materials

JSTM

CONTENTS

JST&M 8(2025), 1 – 4
DOI: 10.57131/jstm.2025.8.1

Original scientific paper

CHANGE IN pH AND CONDUCTIVITY DURING THE RINSING AND THE BIOSORPTION OF COPPER IONS ONTO PUMPKIN PEEL

Marina Marković, Milan Gorgievski, Miljan Marković, Vesna Grekulović, Nada Štrbac, Milica Zdravković, Kristina Božinović

University of Belgrade – Technical faculty in Bor, Bor, Serbia

ABSTRACT

The changes in pH and conductivity during the rinsing of the pumpkin peel, and the biosorption of Cu^{2+} ions, were the subject of this work. The obtained data showed that the pH value of the solutions increased during the rinsing of the biosorbent, as a result of the transfer of H^{+} ions from the aqueous phase into the structure of the pumpkin peel. An increase in the conductivity value was observed in the initial period of rinsing the pumpkin peel, followed by a decrease. The increase in conductivity in the initial phase contributed to the self-leaching of the alkali and alkaline earth metal ions from the structure of the pumpkin peel, which were transferred into the aqueous phase. The further decrease in conductivity is a result of the dilution of the aqueous phase. The pH value decreased during the biosorption of Cu^{2+} ions, as hydrogen ions were transferred from the pumpkin peel structure into the solution, and then exchanged with Cu^{2+} ions. The conductivity value increased during the biosorption process, with a rapid increase in the initial period of 5 minutes, due to the transfer of alkali and alkaline earth metal ions into the solution.

Keywords: biosorption, pumpkin peel, pH, conductivity

Corresponding Author:
Marina Marković,
University of Belgrade – Technical Faculty in Bor
Vojske Jugoslavije 12, Bor, Serbia
Tel.: +381637061451
E-mail address: marina.markovic@tfbor.bg.ac.rs

1. INTRODUCTION

Water pollution is one of the most significant problems facing the modern world. It is caused by the unselective discharge of various pollutants into bodies of water. One of the main causes of this problem is industry, which is responsible for the discharge of large quantities of toxic heavy metals into the environment. The rapidly growing development of industrial activities, including mining and metal processing industries, in the 21st century, has led to an increase in the amount of wastewater produced [1,2]. Heavy metals are treated on an industrial scale using conventional methods, such as chemical precipitation, cementation, ion exchange, solvent extraction, electro-extraction, reverse osmosis, etc [3]. However, these conventional methods also have disadvantages, such as: insufficient degree of metal removal, large amounts amounts of sludge and the need for further processing, high investment costs, etc. Biosorption has emerged as a potential alternative to conventional methods for wastewater treatment. Biosorption has been proven on the laboratory scale to be the most effective alternative to conventional methods of removing heavy metals from wastewater. It is an efficient and cost-effective alternative that allows the application of inexpensive

and locally available biomaterials such as agricultural and industrial by-products, which have natural metal binding capabilities, as biosorbents. Biosorption can be described as the ability of the active sites present in the structure of biomaterials to bind heavy metals. The process of binding metal ions consists of many complex physicochemical processes, including ion exchange, complexation, electrostatic interactions, micro-deposition, and others [4,5].

2. EXPERIMENTAL

The pumpkin peel used as a biosorbent for the biosorption experiments was firstly ground and then sieved on a set of laboratory sieves. The fraction (-1+0.4) mm was used for further experiments. Before the biosorption experiments, the samples were rinsed with 400 mL of distilled water, to remove the physical impurities and free the active sites in the biosorbent structure.

The Cu^{2+} solutions used for the biosorption experiments were prepared with $CuSO_4 \cdot 5H_2O$ (LACHEMA, Czech Republic). The pH and conductivity values were measured during the rinsing of the pumpkin peel samples.

The biosorption experiments were performed in a batch system. 1 g of the pumpkin peel sample was brought into contact with 50 mL Cu^{2+} solutions, for different contact times. The pH and conductivity values were monitored during the biosorption process.

3. RESULTS AND DISCUSSION

3.1. Change in pH value during the rinsing of the pumpkin peel

Figure 1 shows the change in the pH of the aqueous phase during rinsing of the pumpkin peel sample. The sample was rinsed in 10 portions of 40 mL. The obtained results show that the pH value increases rapidly during rinsing with the first 80 mL, after which the increase continues, but at a slower rate. The increase in pH during rinsing of the biosorbent occurs due to the transfer of H^+ ions from the aqueous phase into the structure of the pumpkin peel sample, where they are exchanged with the alkali and alkaline earth metal ions. The H^+ concentrations were calculated from the obtained pH values, and the results showed that 0.00294 mmol g^{-1} of H^+ ions were transferred into the pumpkin peel structure. This means that about 63 % of the H^+ ions were adsorbed during the rinsing of the pumpkin peel sample.

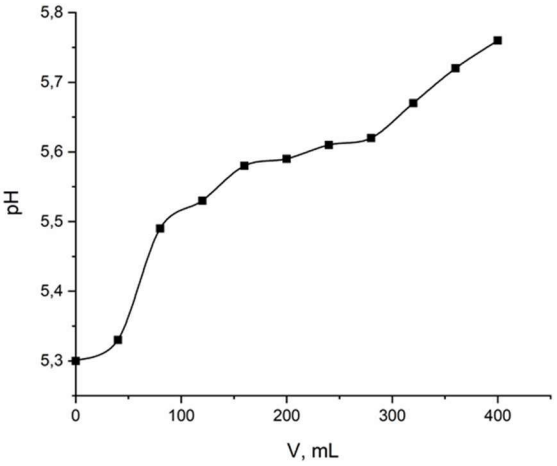

Figure 1. Change in pH value during the rinsing of the pumpkin peel sample

3.2. Change in conductivity during the rinsing of the pumpkin peel

The conductivity (k) of aqueous solutions indicates their ability to conduct electricity. The conductivity of aqueous solutions depends on the ions present, their concentration, mobility, and charge, as well as on the temperature at which it is determined [6].

The change in conductivity during rinsing of the biosorbent is shown in Figure 2. It can be seen that the conductivity increases in the first period, up to about 50 mL of passed distilled water, after which there is a decrease. The increase in conductivity in the first period occurs due to the transfer of alkali and alkaline earth metal ions from the pumpkin peel structure into the aqueous phase. The subsequent decrease in conductivity after the first period is the result of the decrease in the concentrations of alkali and alkaline earth metal ions, as the rinsate is diluted.

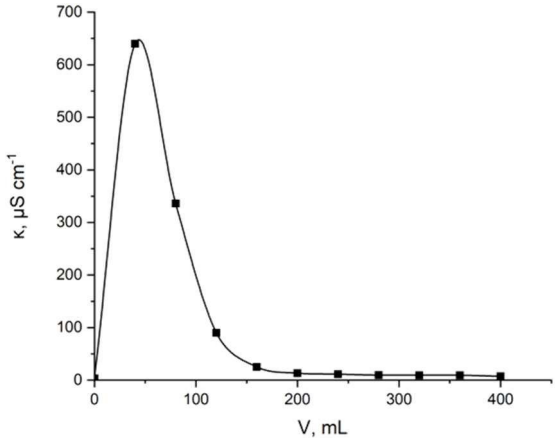

Figure 2. Change in conductivity during the rinsing of the pumpkin peel sample

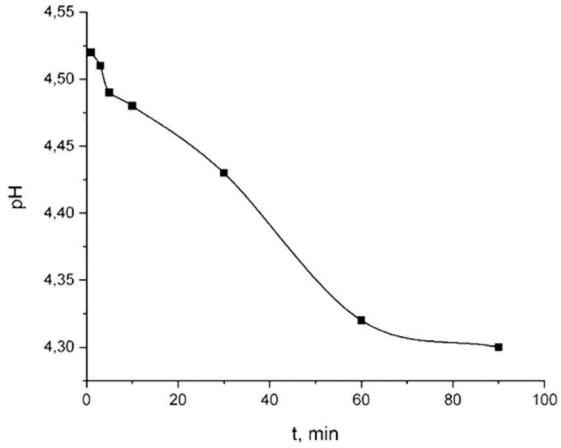

Figure 3. Change in pH value during the biosorption process

3.3. Change in pH during the biosorption of Cu^{2+} ions onto pumpkin peel

The change in pH of the solution during the biosorption of Cu^{2+} ions using pumpkin peel as a biosorbent is shown in Figure 3. As can be seen, the pH of the solution decreases during the biosorption process, in contrast to the change of the same parameter during the rinsing of the biosorbent. It is hypothesised that the decrease in pH is observed due to the deprotonation of the functional groups in the pumpkin peel sample and the transfer of H^+ ions from the sample structure into the solution where they are exchanged with Cu^{2+} ions.

3.4. Change in conductivity during the biosorption of Cu2+ ions onto pumpkin peel

Figure 4 shows the change in conductivity during the biosorption of copper ions using pumpkin peel as a biosorbent. It can be seen that the conductivity of the solution increases during the biosorption process. The rapid increase in conductivity is observed in the initial phase (first 5 minutes). This increase occurs due to the transfer of alkali and alkaline earth metal ions from the pumpkin peel structure into the aqueous phase.

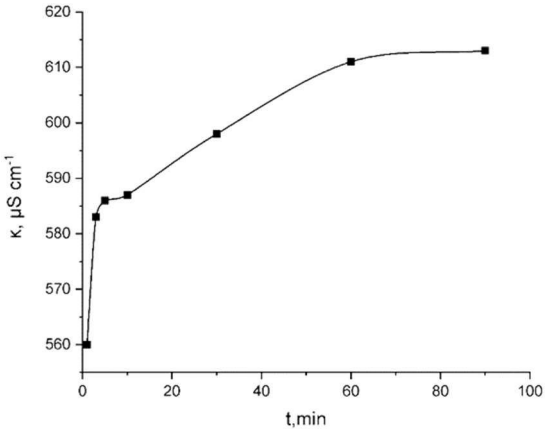

Figure 4. Change in conductivity during the biosorption process

4. CONCLUSIONS

The changes in pH and conductivity during the rinsing of the pumpkin peel and the biosorption of copper ions were monitored and presented in this paper. During the rinsing of the biosorbent, the pH of the solution increases due to the transfer of H^+ ions from the aqueous phase into the structure of the pumpkin peel. The conductivity of the solution initially increases until about 50 mL of distilled water has passed, where it reaches its maximum value. Further rinsing leads to a decrease in the conductivity of the solution. The increase in conductivity occurs due to the increase in the concentration of alkali and alkaline earth metal ions in the solution,

which are transferred from the pumpkin peel structure to the aqueous phase. With further rinsing, the conductivity decreases as the concentration of these ions decreases due to the dilution of the solution. During the biosorption experiments, the pH decreases due to the deprotonation of the functional groups present in the pumpkin peel structure and the transfer of H^+ ions into the solution, where they are exchanged with copper ions. The conductivity of the solution increases during the biosorption process. This increase occurs due to the increase in the concentration of alkali and alkaline earth metal ions in the solution, which are exchanged with copper ions during the biosorption process.

Acknowledgments

The research presented in this paper was done with the financial support of the Ministry of Science, Technological Development and Innovation of the Republic of Serbia, with the funding of the scientific research work at the University of Belgrade - Technical Faculty in Bor, according to the contract with registration number 451-03-137/2025-03/200131.

Conflicts of Interest

The authors declare no conflict of interest.

4. REFERENCES

[1] F. Fu, Q. Wang, Removal of heavy metal ions from wastewaters, A review, *Journal of Environmental Management*, 92 (2011), pp. 407-418

[2] T.V. Ramachandra, N. Ahalya, R. D. Kanamadi, Biosorption, Techniques and Mechanisms, *CES Technical Report*, 110 (2005) 7, pp. 1-34

[3] V. Stanković, D. Božić, M. Gorgievski, G. Bogdanović, Heavy metal ions adsorption from mine waters by sawdust, *Chemical Industry & Chemical Engineering Quarterly*, 15 (2009) 4, pp. 237-249

[4] S. H. Acheampong, I. M. Ismail, T. M. Mostafa, A. H. Sulaymon, Biosorption of Heavy Metals: A Review, Journal of Chemical Science and Technology, 3 (2014) 4, pp. 74-102

[5] Witek-Krowiak, R. Szafran, Biosorption of heavy metals from aqueous solutions onto peanut shell as a low-cost biosorbent, *Desalination*, 265 (2001), pp. 126-134

[6] M. Gorgievski, D. Božić, V. Stanković, N. Štrbac, S. Šerbula, Kinetics, equilibrium and mechanism of Cu^{2+}, Ni^{2+} and Zn^{2+} ions biosorption using wheat straw, *Ecological Engineering*, 58 (2013), pp. 113-122

JST&M 8(2025), 5 – 16
DOI: 10.57131/jstm.2025.8.2

Original scientific paper

COMPARATIVE NUMERICAL ANALYSIS OF COAL AND BIOMASS PARTICLE DISTRIBUTION IN AERO-MIXTURE CHANNELS

Amel Mešić

University of Tuzla – Faculty of Mechanical Engineering

ABSTRACT

To analyze the co-combustion process of coal and biomass in a steam boiler furnace originally designed for pulverized coal combustion, it is crucial to first investigate the dynamic behavior of particles within the aero-mixture channels. Due to differences in material properties and particle size distributions, the behavior of coal and biomass particles can vary significantly. This study numerically models particle dynamics using a simulation approach based on a previously validated Euler-Lagrange computational fluid dynamics (CFD) model. The simulation results reveal key differences in the trajectories and velocities of coal and biomass particles, primarily caused by variations in their density and size. The main objective of this research is to identify and quantify the factors influencing particle dynamics, as well as to determine the interdependencies between them. The findings aim to provide valuable insights for optimizing burner design and enhancing the efficiency of the co-combustion process. Furthermore, the results contribute to a broader understanding of biomass particle behavior in multiphase flows, which is particularly important in the context of transitioning towards sustainable and low-emission energy systems.

Keywords: Aero mixture; biomass; coal; co-combustion.

Corresponding Author:
Amel Mešić
Univerzitet u Tuzli – Mašinski fakultet
Urfeta Vejzagića br.4, Tuzla, BiH
Tel.: +38762181333
E-mail address: amel.mesic.msf@gmail.com

1. INTRODUCTION

Environmental pollution (air, water, soil, etc.), resulting from the accelerated industrial development of modern society, has severe and far-reaching consequences for the health of humans as well as other living organisms. Thermal power plants that produce electricity by burning coal are among the major local polluters, and in many cases, they also exert regional environmental impacts. In numerous developing countries, coal remains the most commonly used resource for electricity generation, due to its stable reserves and economic viability. Coal-fired thermal power plants emit by-products of the combustion process (solid particles and flue gases) into the atmosphere. The possibilities for reducing pollutant emissions and increasing the efficiency of thermal power plants using conventional methods have reached their maximum, and in such a situation, even the slightest improvements in efficiency lead to a better position and higher competitiveness [1]. The goal of reducing greenhouse gas emissions has prompted the development of low-emission technologies such as combined cycles, carbon capture and storage, and co-firing of coal with alternative fuels. The increasing

integration of intermittent renewable energy sources into power systems may cause grid stability issues and impose operational challenges on conventional power plants connected to the same system. Due to such fluctuations, a growing number of coal-fired power plants no longer operate solely at base load but are required to frequently adjust output, perform more frequent cold and warm starts, and operate at partial loads to reduce shutdown and restart costs. The energy efficiency, and thereby the environmentally friendly operation of a boiler, primarily depends on the aerodynamic characteristics of the furnace. One potential solution lies in the reconstruction and optimization of existing pulverized coal-fired plants. This strategy would involve running the plants on biomass, waste, or coal within a system that has been optimized specifically for those fuels. It is important to consider that different granulometric and chemical properties of these fuels significantly influence the aerodynamic behavior of the combustion process in the furnace. Numerous numerical and experimental studies support these findings, particularly those focusing on the distribution of fuel material with different particle sizes across milling lines. For example, in the study [2], a mathematical model was developed and validated to describe the flow of a gas-coal two-phase mixture in the aeromixture ducts of the OP650b boiler. In the study [3], numerical modeling was used to analyze the spatial distribution of coal and biomass in the separator, along with the impact of the separator on particle distribution. Study [4] investigates the influence of particle density on the operational characteristics of coal preparation systems. The authors of the study [5] use a numerical model to analyze the impact of mill load on the distribution of coal dust particles. Additional numerical and experimental research on the behavior of biomass particles in turbulent flows was conducted in studies [6,7] and [8]. Belošević et al. provide a comprehensive analysis of methods for predicting the co-combustion of coal and biomass in the study [9]. In the study [10], the aerodynamics of burner jets in tangentially-fired boilers are analyzed using CFD modeling and experiments to optimize combustion efficiency. Furthermore, CFD modeling is employed in [11] to investigate the distribution of pulverized coal within the mill-duct system of the As Pontes Power Plant, to improve coal flow and combustion efficiency. A 3D simulation of gas-solid flow in a coal powder separator was conducted by Babić [12], while Kozić et al. [13] analyzed flow behavior in the ventilation mill and aeromixture channel of the lignite-fired Kostolac B power plant, providing valuable insights for system optimization.

As shown in previous research, numerical modeling software plays a significant role as a leading tool for describing the phenomena and processes associated with these mechanisms. The OP650b boiler in Thermal Power Plant Tuzla faces similar, previously defined challenges. Therefore, before any experimental or numerical investigation of coal and biomass co-firing is carried out within the scope of this work, a numerical analysis of the aerodynamic behavior of the combined distribution of coal and biomass particles in the aero mixture channels was conducted. This research extends the numerical model from reference [2], which accurately captured the behavior of

coal dust particles in aeromixture channels. The current level of knowledge regarding the co-firing process leads to the conclusion that co-firing coal with biomass is considered an important step in reducing environmental emissions. While fuel variation alone is not the only solution for reducing harmful emissions, it is among the most cost-effective options. A review of previous studies mainly focused on coal distribution reveals the existence of certain issues during the process that negatively impact combustion efficiency. Inadequate and imprecise information regarding fuel distribution within the boiler furnace can

result in abnormal combustion, steam and material overheating, as well as slagging and fouling. Therefore, before investigating flame aerodynamics, it is essential to first determine the proper distribution of the fuel mixture and identify the influencing parameters that affect the co-firing process.

2. NUMERICAL MODEL

The simulations in this study were performed using the commercial CFD software Siemens STAR CCM+, due to its advanced capabilities in modeling turbulent multiphase flows with two-way coupling between the gas and particle phases. The computational model is based on the Euler–Lagrange approach, where the continuous phase (air) is treated in an Eulerian framework and the dispersed phase (coal and biomass particles) in a Lagrangian framework, allowing for individual particle tracking.

The gas phase equations are solved using the Reynolds-Averaged Navier–Stokes (RANS) method, with turbulence modeled via the standard k−ε model. The interaction between the gas and particle phases is fully coupled, allowing momentum exchange. The particle motion is governed by Newton's second law, incorporating drag and gravity, while collisions with walls are modeled using restitution coefficients (0.9 tangential and 1.0 normal). Particle-particle interactions are neglected. The physical model assumes the following for the gas phase:

- the concept of the continuum is used to describe the flow;
- it is a single-component gas;
- the gas flow is steady;
- the gas flow is three-dimensional,
- the gas flow is incompressible;
- the gas flow is isothermal;
- the gas flow is chemically inert;
- the gas flow is turbulent.

For the particle phase, the assumptions include:

- two distinct materials (coal and biomass) with constant but different densities (1200 kg/m³ for coal and 600 kg/m³ for biomass);
- fixed particle shapes approximated as spheres;
- coal particles following a Rosin-Rammler size distribution (mean diameter D = 178 µm, spread parameter n = 2.23) based on validated data from previous research [2];
- biomass particles modeled with fixed cylindrical diameters of 3.6 mm, 1 mm, 0.7 mm, and 0.45 mm, chosen through an iterative simulation process and prior experimental data;
- no heat or mass transfer (particles retain constant temperature and mass);
- stochastic particle trajectories with partial kinetic energy loss upon wall collisions;
- the effect of the secondary phase on the primary phase is considered.
- particles lose a certain amount of kinetic energy upon impact with the internal walls;
- the particles move stochastically.

The computational domain was discretized using tetrahedral meshes, with mesh sizes ranging from 352,272 to 490,231 cells depending on the damper angle configuration. A visualization of the domain and boundary labels is shown in Figure 1.

Boundary conditions were defined as follows:

- Inlet: Uniform velocity of 23 m/s for the gas phase; particles are injected with the same velocity. Mass flow rates were 5.5 kg/s for coal and 1.488 kg/s for biomass.
- Outlet: Defined as pressure outlets with reference pressure set to 0 Pa. For particles, the “escape” condition was applied, terminating tracking at the domain exit.
- Walls: Reflective boundaries using restitution coefficients to account for energy loss upon particle collision.

An overview of all simulations and corresponding boundary conditions is presented in Table 1.

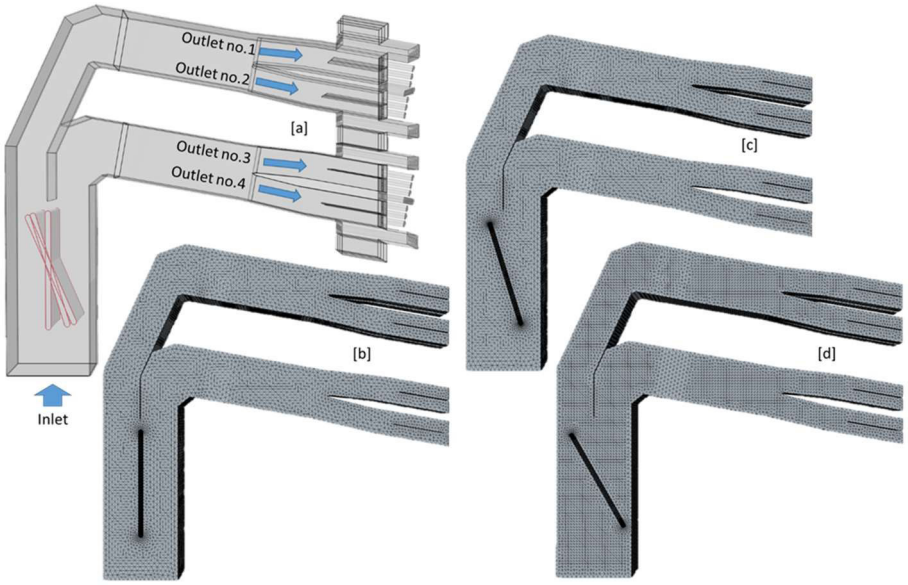

Figure 1. Air-fuel mixture channel with indicated inlet and outlet boundaries (a), and visualization of the discretized computational domain for different control damper angles (b, c, and d)

Table 1. Overview of Boundary Conditions for the Conducted Simulations

Type of Boundary Condition	Velocity of Aeromixture [m/s]	Inlet Particle Velocity [m/s]	Mass Flow Rade of Coal Particles [kg/s]	Mass Flow Rate of Biomass Particles [kg/s]	Coal Particle Size (Rossin-Rammler distribution) and Density [kh/m³]	Biomass Particle Size [mm] and Density [kg/m³]	Inlet Fluid Temperature [°C]	Control Damper Angle [°]	Tangential Restitution Coefficient	Normal Restitution Coefficient
Simulation No. 1										
Inlet Boundary	23	23	5.5	1.488	D=178µm n=2.23 σ=1200	**3.6** σ=600	190		/	
Wall Boundary					/			0	0.9	1
Simulation No. 2										
Inlet Boundary	23	23	5.5	1.488	D=178µm n=2.23 σ=1200	**1** σ=600	190		/	
Wall Boundary					/			0	0.9	1
Simulation No. 3										
Inlet Boundary	23	23	5.5	1.488	D=178µm n=2.23 σ=1200	**0.7** σ=600	190		/	
Wall Boundary					/			0	0.9	1
Simulation No. 4										
Inlet Boundary	23	23	5.5	1.488	D=178µm n=2.23 σ=1200	**0.45** σ=600	190		/	
Wall Boundary					/			**0**	0.9	1

Type of Boundary Condition	Velocity of Aeromixture [m/s]	Inlet Particle Velocity [m/s]	Mass Flow Rade of Coal Particles [kg/s]	Mass Flow Rate of Biomass Particles [kg/s]	Coal Particle Size (Rossin-Rammler distribution) and Density [kh/m³]	Biomass Particle Size [mm] and Density [kg/m³]	Inlet Fluid Temperature [°C]	Control Damper Angle [°]	Tangential Restitution Coefficient	Normal Restitution Coefficient
Simulation No. 5										
Inlet Boundary	23	23	5.5	1.488	D=178μm n=2.23 σ=1200	0.45 σ=600	190		/	
Wall Boundary					/			**17.24**	0.9	1
Simulation No. 6										
Inlet Boundary	23	23	5.5	1.488	D=178μm n=2.23 σ=1200	0.45 σ=600	190		/	
Wall Boundary					/			**29.8**	0.9	1

Since the validation process of the aero mixture channel process was carried out in the study [2] with a satisfactory degree of accuracy, the validation of the current problem will not be presented in this work. instead, the validated model from study [2] will be further developed by observing biomass particles in the aero mixture channel.

Simulating and analyzing the biomass distribution complements the lack of data related to the aerodynamic behavior of biomass particles within the aero mixture channel. This primarily involves comparing the dynamics of biomass and coal particles, their velocity values at the exits of the burners, as well as the distribution along the height of the burner itself.

3. RESULTS OF NUMERICAL SIMULATIONS

For the same position of the manual control damper, an initial analysis was conducted on the distribution of biomass particles of various fixed sizes and coal particles defined by the rossin-rammler (rr) distribution. Through an iterative investigation of biomass particle sizes ranging from 3.6 mm to 0.45 mm, it was determined that only biomass particles with a diameter of 0.45 mm exhibit aerodynamic characteristics comparable to those of coal particles.

This similarity is particularly significant in the context of fuel substitution in combustion systems originally designed for coal, as it suggests the potential for using fine biomass particles without the need for major modifications to existing infrastructure.

A visual inspection of the flow field (Figure 2) revealed a pronounced deviation in the aerodynamic behavior of larger biomass particles compared to coal particles, highlighting their reduced ability to follow the fluid streamlines and distribute uniformly within the flow channel.

This behavior underscores the critical role of particle size in achieving stable and efficient fuel transport, as only sufficiently small biomass particles can achieve the necessary flow conformity for reliable performance in coal-adapted systems. Consequently, ensuring proper particle size distribution during biomass preprocessing becomes essential to optimize flow dynamics and maintain combustion efficiency in retrofitted coal-fired systems.

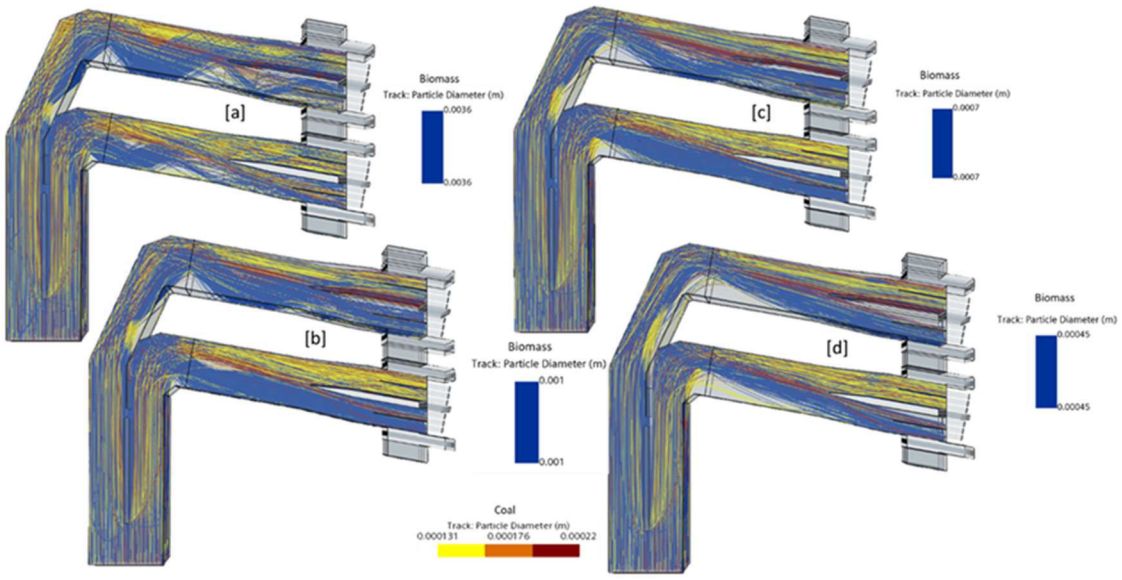

Figure 2. Comparative visualization of the trajectories of biomass particles with different fixed sizes about the trajectories of coal particles whose sizes are defined by the Rossin-Rammler distribution: a) biomass particle size is 3.6 mm, b) biomass particle size is 1 mm, c) biomass particle size is 0.7 mm, d) biomass particle size is 0.45 mm

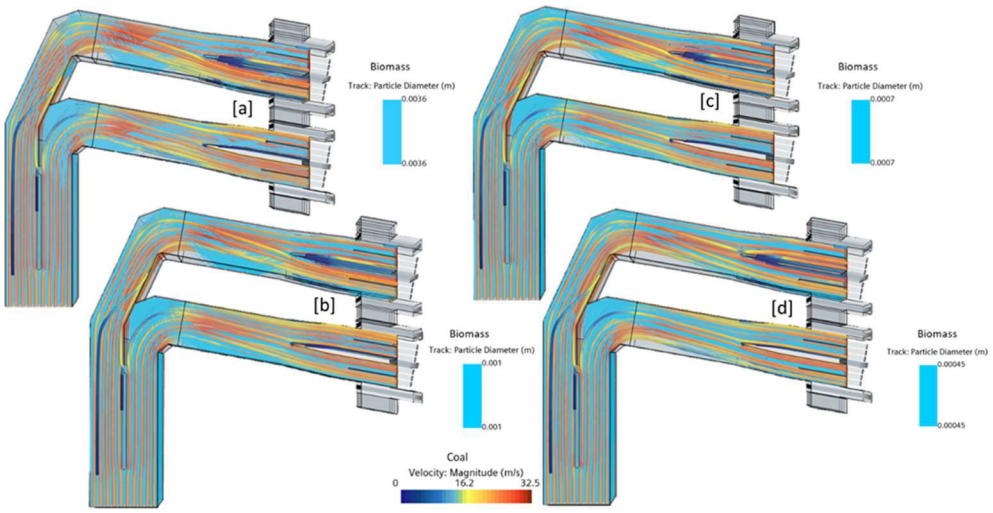

Figure 3. Comparative visualization of the trajectories of biomass particles with different fixed sizes about the gas-phase flow: a) biomass particle size is 3.6 mm, b) biomass particle size is 1 mm, c) biomass particle size is 0.7 mm, d) biomass particle size is 0.45.

Figure 3 presents a comparative illustration of the trajectories of biomass particles of varying sizes and their deviations from the primary gas flow path. The images underscore the importance of achieving dynamic equilibrium between the flow patterns of the primary and secondary phases within the aero mixture channel to ensure uniform biomass distribution along the burner height. This figure also illustrates

the relationship between particle size and the resulting flow fields, clearly demonstrating that the inertia of biomass particles decreases proportionally with particle size reduction.

Although the flow simulations were performed using a fully three-dimensional computational domain, selected results are presented as two-dimensional fields for visualization purposes, a shown in Figures 4, 6, and 7. These 2D visualizations facilitate clearer presentation and allow for easier comparison of certain flow characteristics. However, they do not fully capture the spatial complexity of particle behavior, particularly phenomena such as secondary vortices, cross-flow dispersion, and interactions between particles and bounding surfaces. The three-dimensional geometry, along with the angle of particle impact, can significantly influence particle trajectories, causing dispersion not only in the direction of the primary flow but also transversely.

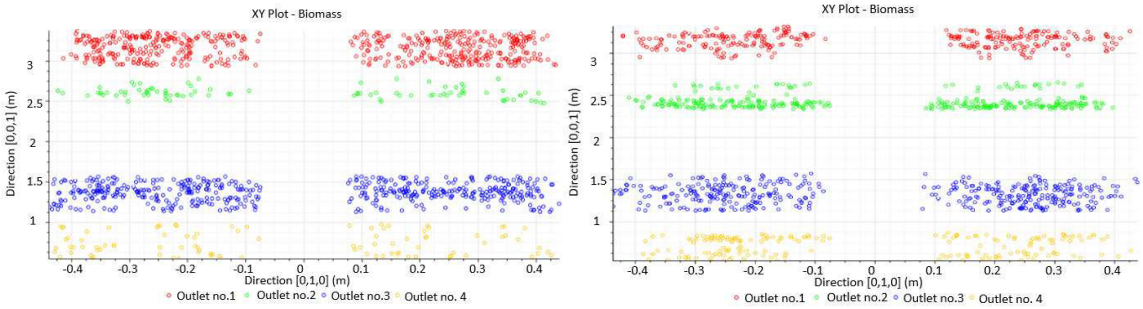

Figure 4. Visualization of biomass particle concentration along the burner height: (left) for particle size of 3.6 mm, (right) for particle size of 0.45 mm.

Consequently, two-dimensional simulations provide only a partial representation of these complex transport phenomena. While 2D representations are useful for identifying general trends and facilitating comparisons, the interpretation of results ultimately relies on the full three-dimensional simulations from which these sections are derived.

A detailed view of the outlet distribution of biomass particles along the burner height is provided in Figure 4, which displays two-particle distribution diagrams corresponding to different particle diameters. The left diagram in Figure 4, representing biomass particles with a diameter of 3.6 mm, clearly illustrates a disproportionately higher concentration of particles exiting through the upper sections of the burner. This uneven distribution suggests that larger particles, due to their higher inertia, tend to resist changes in direction and are less capable of following the intended flow paths within the burner structure.

In contrast, the right diagram in Figure 4, which depicts the distribution of 0.45 mm particles, shows a significantly more uniform distribution across all four burner levels. This uniformity is attributed to the lower mass and increased fluid responsiveness of the smaller particles, which allows them to be more evenly entrained by the carrier gas and distributed more symmetrically throughout the burner outlets.

Such differences in outlet distribution are not merely geometrical but directly influence combustion dynamics within the furnace chamber. Uneven particle loading can lead to localized temperature imbalances, incomplete combustion, and increased emissions, whereas a uniform distribution of fine particles promotes stable flame formation, consistent heat release, and improved overall efficiency of the combustion process.

Figure 5 presents a diagram showing the percentage load of each burner level for different biomass particle sizes, aimed at performing a statistical analysis of particle dispersion along the burner height. In the

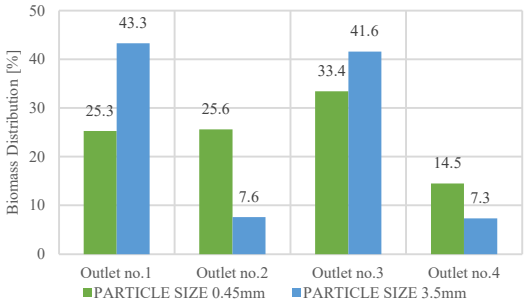

Figure 5. Diagram of biomass particle concentration along the burner height for different particle sizes.

case of biomass particles with a diameter of 3.5 mm, the diagram indicates a significant distribution imbalance, with a higher concentration observed at outlets No. 1 and No. 3. Conversely, a more uniform distribution is evident for cases involving finer particle granulation. If we examine the diagram illustrating the variation of particle velocity for biomass along the vertical axis of the burner (Figure 6), comparing both coarse and fine granulations, a clear distinction emerges in the range and behavior of particle velocities. Specifically, Figure 6 (left) presents the velocity profile for biomass particles with a diameter of 3.6 mm, where the recorded velocities reach up to approximately 21 m/s. This velocity range is notably lower than that observed for coal particles under comparable conditions, as illustrated in Figure 6-right. In Figure 6-right, it can be seen that coal particles attain considerably higher velocities, indicating a greater degree of acceleration and momentum transfer from the carrier fluid. This contrast highlights a fundamental aerodynamic discrepancy between coal and coarse biomass particles. The higher density and more favorable aerodynamic properties of coal enable it to be more effectively accelerated by the airflow, whereas larger biomass particles, with their lower density and higher drag coefficient, exhibit a reduced response to the flow field. As a result, the motion intensity, which reflects the dynamic behavior of particles within the flow, is significantly higher for coal particles. From an aerodynamic perspective, this discrepancy suggests a lag in response time and reduced entrainment efficiency for larger biomass particles. This lag not only affects particle transport and distribution but may also lead to undesirable combustion outcomes, such as delayed ignition, inconsistent flame propagation, or incomplete combustion. These findings underscore the importance of considering particle velocity profiles in the design and optimization of biomass injection systems, particularly when adapting existing coal combustion infrastructure. Ensuring that biomass particles can reach velocities comparable to those of coal is essential for maintaining stable combustion and minimizing performance losses in co-firing or biomass-only scenarios.

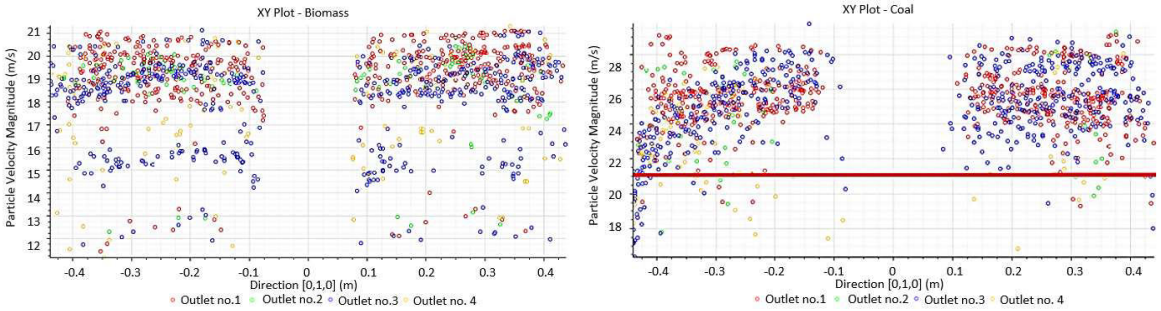

Figure 6. Visualization of biomass particle velocity variation (left) and coal particle velocity variation (right) along the burner height for a fixed biomass particle size of 3.6 mm.

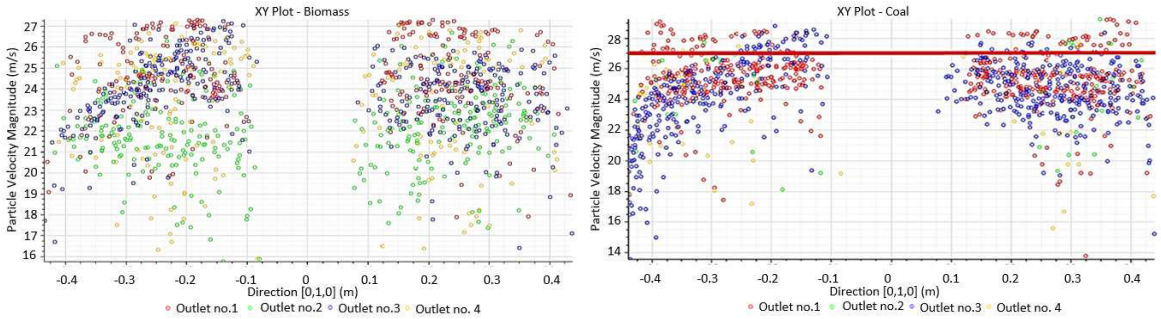

Figure 7. Visualization of biomass particle velocity variation (left) and coal particle velocity variation (right) along the burner height for a fixed biomass particle size of 0.45 mm.

Figure 7 (left) illustrates the velocity intensity distribution of biomass particles with a diameter of 0.45 mm at the burner outlet, while Figure 7-right provides a comparative visualization of the velocity distribution for coal particles under similar flow conditions. Upon analysis, these diagrams reveal a noticeable improvement in the velocity characteristics of biomass particles, with the 0.45 mm particles exhibiting a more balanced and consistent velocity profile in comparison to the more variable distribution observed in the case of coal particles. This relative improvement in flow dynamics suggests that with appropriate particle sizing, biomass can achieve a flow performance that closely aligns with that of coal, particularly in terms of momentum transfer and entrainment behavior within the burner geometry. However, while the 0.45 mm biomass particles demonstrate improved behavior, achieving a near-dynamic equivalence with coal particles particularly crucial for co-firing applications requires even finer granulation.

Based on the comprehensive flow and velocity analyses conducted, a particle diameter of approximately 0.45 mm has been identified as the critical size at which biomass particles begin to closely mimic the aerodynamic properties of pulverized coal.

At this size, the difference in behavior between coal and biomass becomes minimal, with an acceptable deviation of around 7% in aerodynamic performance parameters.

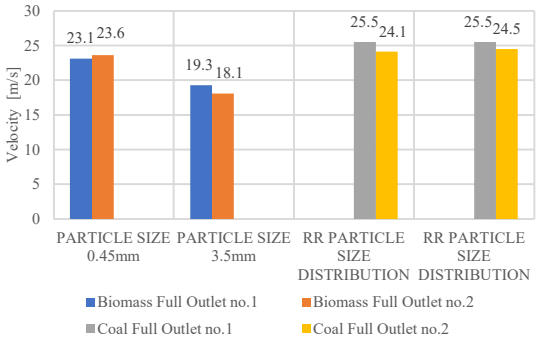

Figure 8. Diagram of biomass and coal particle velocity variation along the burner height

Further supporting this conclusion, Figure 8 presents a detailed diagram of velocity variation for both biomass and coal particles along the height of the burner. This figure provides a vertical profile of particle velocities, enabling a direct comparison of how different particle types accelerate and interact with the flow field at various burner levels. The diagram indicates that as the biomass particle size approaches the 0.45 mm threshold, the velocity profiles of biomass and coal begin to converge, indicating improved synchrony in particle transport. Such convergence is vital for ensuring even fuel distribution, consistent flame front development, and optimal combustion efficiency throughout the burner height. For analyzing the co-combustion process, it is also important to consider the distribution of biomass particles within the air-fuel mixture channel, depending on the angle of the manual control damper.

Figure 9 illustrates the distribution of biomass particles with granulation of 0.45

mm as a function of the damper angle. To analyze the co-combustion process of coal and biomass in a furnace of a steam boiler primarily designed for the combustion of pulverized coal, it is essential to first examine the dynamic behavior of different particles in the aero mixture channels. A clear understanding of how biomass and coal particles behave under varying flow conditions provides valuable insights into how to optimize fuel delivery and combustion efficiency. In this regard, the position of the manual control damper significantly influences the distribution pattern of particles along the burner height.

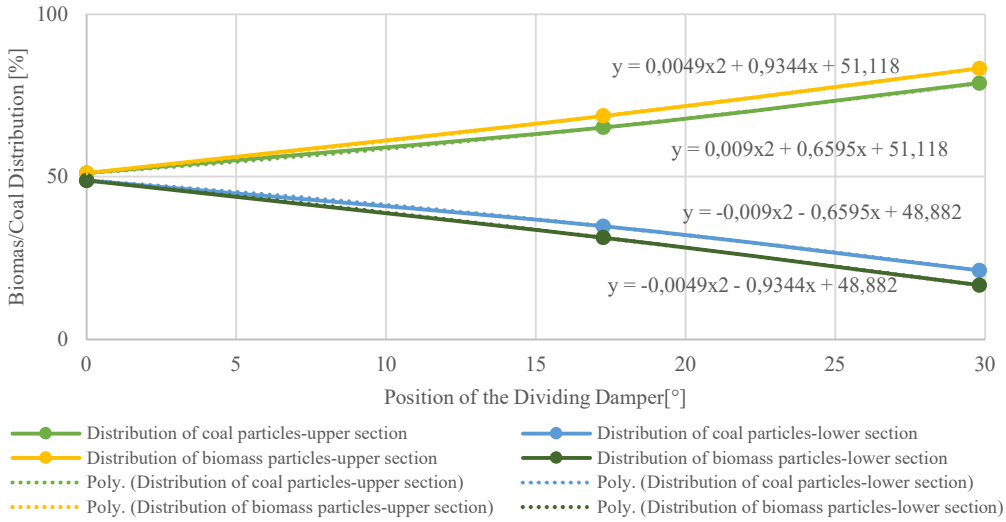

Figure 9. Functional representation of biomass and coal particle distribution for different control damper angles: 0°, 17.24°, 29.8°

By adjusting the damper angle, the velocity field and turbulence intensity within the air-fuel mixture channel change, which directly impacts particle trajectories, especially for biomass particles due to their lower density and greater sensitivity to aerodynamic forces.

The results presented in Figure 9 show a comparative overview of the particle load at the upper and lower burner outlets for both coal and biomass. The observed trends are fitted with linear polynomial functions, revealing a nearly linear correlation between the damper angle and particle distribution. Biomass particles exhibit more pronounced variation with changing damper angles, which is evident from the steeper slopes of the trend lines. For example, with increasing damper inclination, the concentration of biomass at the upper outlets increases, while it decreases at the lower outlets. This redistribution is a consequence of the altered flow field, which affects the inertia-driven behavior of lighter biomass particles. In contrast, the distribution of coal particles remains relatively stable, confirming their higher inertia and weaker response to variations in the flow pattern. This difference between the two fuel types is particularly important when designing co-firing strategies, as it highlights the need for fine-tuning damper settings to achieve a uniform and balanced fuel-air mixture. The established functional relationships shown in the diagram can serve as a basis for defining realistic boundary conditions in future computational simulations of the co-combustion process. In summary, the data demonstrates that the damper angle can be used as a control parameter to fine-tune the dispersion of biomass particles, ultimately improving the consistency and efficiency of

combustion in existing coal-based boiler systems.

4. CONCLUSION

The analysis demonstrates that particle size plays a crucial role in the aerodynamic behavior of biomass within the flow field. Visual observations and computational results reveal that larger biomass particles significantly deviate from the fluid streamlines, unlike finer particles or coal, which are able to conform more closely to the flow dynamics. This discrepancy emphasizes the importance of ensuring a sufficiently small particle diameter approximately 0.45 mm during biomass preprocessing, as only at this size do biomass particles begin to exhibit aerodynamic properties comparable to pulverized coal. Proper particle size control is therefore essential for achieving stable and efficient fuel transport, uniform mixing, and effective combustion in retrofitted coal-fired systems. Larger particles, due to their slower response time and reduced entrainment efficiency, contribute to uneven loading, which may result in local temperature imbalances, delayed ignition, incomplete combustion, and increased pollutant emissions. Furthermore, the distribution of biomass particles within the air-fuel mixture channel is strongly influenced by the angle of the manual control damper. A clear understanding of how these particles behave under varying flow conditions allows for more effective fine-tuning of damper settings to ensure a balanced and homogeneous fuel-air mixture. These findings not only provide valuable insights for optimizing co-firing strategies but also establish functional relationships that can be used to define realistic boundary conditions in future computational simulations of the co-combustion process.

Acknowledgments

The author would like to express his gratitude to JP Elektroprivreda BiH for providing technical support during the course of the research.

Conflicts of Interest

The author declares no conflict of interest.

5. REFERENCES

[1] I. Buljubašić, S. Delalić, Improvement of steam boiler plant efficiency based on results of on-line performance monitoring, Tehnički vjesnik – *Technical Gazette*, 15 (2008) 3, pp. 29–33, https://hrcak.srce.hr/28545

[2] A. Mesić, I. Delić, N. Ganibegović, Numerical modelling of multiphase flow inside aero-mixture channel and low emission burner of boiler OB-650, *Technium*, 2 (2020) 7, pp. 94–106, https://doi.org/10.47577/technium.v2i7.1649 technium

[3] S. Ciukaj, B. Hernik, Field and CFD Study of Fuel Distribution in Pulverised Fuel (PF) Boilers, *Journal of Thermal Science*, 29 (2020) 3, pp. 535–545, https://doi.org/10.1007/s11630-020-1199-0

[4] O. Stamenković, G. Stupar, D. Tucaković, Assessing the impact of specific weight of different-sized particles on operational performance of coal preparation plant, *Thermal Science*, 27 (2023) 1A, pp. 103–119. https://doi.org/10.2298/TSCI2301103S

[5] I. Delić, A. Mesić, N. Ganibegović, M. Osmić, The Influence of Mill Loading on the Distribution of Pulverised Coal Particles, in: Advanced Technologies, *Systems, and Applications*, VIII (2023), pp. 518–532. https://doi.org/10.1007/978-3-031-43056-5_39

[6] A. Elfsakhany, X. S. Bai, Numerical and experimental studies of irregular-shape biomass particle motions in turbulent flows, *Engineering Science and Technology, An International Journal*, 22 (2019), pp. 249–265. https://doi.org/10.1016/j.jestch.2018.10.005

[7] A. Elfaskhany, L. X. Tao, X. S. Bai, Transport of pulverised wood particles in turbulent flow: numerical and experimental studies, *Energy Procedia*, 61 (2014), pp. 1540–1543. https://doi.org/10.1016/j.egypro.2014.12.165

[8] A. R. Mahdi, E. B. Zhukov, H. A. Dhahad, Experimental investigation of aerodynamic behaviour of wood chips in fluidized bed reactors as sustainable biomass fuel, *Results in Engineering*, 23 (2024), 102533. https://doi.org/10.1016/j.rineng.2024.102533

[9] S. Belošević, Modeling Approaches to Predict Biomass Co-firing with Pulverised Coal, *The*

Open Thermodynamics Journal, 4 (2010), pp. 50–704, ttps://doi.org/10.2174/1874396X01004010050

[10] J. Hart, A. A. Bhuiyan, J. Naser, Aerodynamics of burner jet in a tangentially-fired boiler: A CFD modelling and experiment, *International Journal of Thermal Sciences*, 129 (2018), pp. 238–253. https://doi.org/10.1016/j.ijthermalsci.2018.02.030

[11] J. L. Ferrin, L. Saavedra, Distribution of the coal flow in the mill-duct system as the As Pontes Power Plant using CFD modelling, *Fuel Processing Technology*, 106 (2013), pp. 84–94. https://doi.org/10.1016/j.fuproc.2012.07.005

[12] V. L. Babić, *Numerical simulation and analysis of 3-dimensional two-phase flow of gas and solid phase in a coal powder separator*, [PhD thesis], University of Belgrade, Faculty of Mechanical Engineering, 2013. https://doi.org/10.2298/BG20130618BABIC

[13] M. Kozić, M. Puharić, S. Ristić, B. Katavić, Numerička simulacija strujanja u ventilacijskom mlinu i kanalu aerosmjese termoelektrane na lignit Kostolac B, *Strojarstvo*, 53 (2011) 2, pp. 83–90

JST&M 8(2025), 17 – 21
DOI: 10.57131/jstm.2025.8.3

Original scientific paper

EXAMINATION OF THE POSSIBILITY OF ENHANCING THE PHYTOREMEDIATION POTENTIAL OF PLANTS THROUGH COMPLEXATION OF ALKALINE SOIL

Farzet Bikić[1], Muvedet Šišić[1], Sanela Beganović[1], Amira Pašalić[1], Adnan Mujkanović[1], Aida Šapčanin[2], Vedran Stuhli[3], Mirnesa Čorbić[3]

[1]University of Zenica, [2]University of Sarajevo, [3]University of Tuzla
Bosnia and Herzegovina

ABSTRACT

This study presents the results of applied phytoextraction as a soil phytoremediation method, based on the analysis of selected heavy metal content in soil and plant material. The selected locations where phytoextraction was applied as a phytoremediation method (Gradišće, Podbrežje, and Tetovo) are situated in the city of Zenica, in proximity to the ArcelorMittal d.o.o. Zenica plant, identified as a potential major source of soil contamination in the surrounding area. The plant species used as potential phytoremediators were maize, Swiss chard, and alfalfa. The study analyzed the heavy metal content (Zn, Ni, Pb, Cd, Cr, and Cu) in soil samples after plant material extraction, as well as in the root samples of the plant material. Additionally, the study presents the pH values of the soil before sowing (initial state) and after plant extraction. The primary objective of this research was to determine whether soil complexation with an aqueous EDTA solution contributed to the increased uptake of selected heavy metals from soil into the selected plants under real environmental conditions. To assess this, one portion of the land plots was treated with a 0.1 M EDTA solution (from sowing until the late growth stage), while the other portion was left untreated. The results presented in this study indicate that soil complexation with the EDTA solution did not significantly enhance the phytoremediation potential of plants in the majority of analyzed samples. One of the key reasons for the reduced mobility of heavy metals from soil into plant material may be the alkaline nature of the soil at all three study locations, with a pH > 8. The mobility of heavy metals is significantly higher in acidic soils compared to alkaline soils.

Keywords: Phytoextraction, complexation, EDTA solution, heavy metals, plants, soil

Corresponding Author:
Farzet Bikić
University of Zenica, Faculty of Engineering and Natural Sciences
Travnička cesta 1, Zenica, BiH
Tel.: 032 401 831; fax: 032 406 903
E-mail address: farzet.bikic@unze.ba

1. INTRODUCTION

Soil contamination by heavy metals is a worldwide problem for human health and safe food production. Except for uncommon geogenic origins, heavy metal contaminants are inadvertently introduced to soils through anthropogenic activities such as mining, smelting, warfare and military training, electronic industries, fossil fuel consumption, waste disposal, agrochemical use, and irrigation [1]. A promising approach to addressing heavy metal pollution through the use of plants is possible due to the phenomenon of metal hyperaccumulation in certain plant species, which, in addition to their tolerance,

possess the enhanced ability to accumulate heavy metals from the soil into plant tissues [2]. Phytoremediation is an emerging technology that employs the use of higher plants for the cleanup of contaminated environments [3]. The concept of phytoremediation was first introduced in 1983 and still, this technique is at the testing stage [4]. Unlike plants that are merely tolerant to heavy metals, hyperaccumulators actively absorb large amounts of one or more different heavy metals, translocate them to aboveground plant organs, and accumulate them at concentrations 100 to 1,000 times higher than non-hyperaccumulating plants. Unlike roots, metal-enriched shoots can be harvested and safely disposed of, with the potential for metal extraction. Phytoextraction is a phytoremediation method by which contaminants (heavy metals) are absorbed from the soil through the root system and then translocated to other plant tissues [5]. Soil decontamination via phytoextraction can be accelerated by adding complexing chemical compounds (chelators), which enhance metal solubility and mobility in the soil, leading to greater metal uptake by plants [6]. The time required for remediation depends on the concentration of heavy metals in the contaminated soil, the growing season, and the selected plant species, ranging from 1 to 20 years. This method is particularly suitable for decontaminating large areas of contaminated soil at shallow depths with low to moderate levels of contaminants. In soil, heavy metals are present in chemically bound forms (oxides, sulfides, sulfates, and carbonates) that are practically insoluble in water. However, since water is a universal solvent due to the polarity of its molecules, chemical compounds binding heavy metals eventually become soluble in water. The objective of this study is to determine whether soil complexation with an aqueous EDTA solution enhances the uptake of selected heavy metals into plants under real environmental conditions. Complexing agents increase metal solubility and, consequently, the mobility of heavy metals in the soil, allowing for greater accumulation in plants, as plants can absorb nutrients and other substances only in aqueous solutions. EDTA solution is a weak acid, and its solutions exhibit mildly acidic properties. Previous studies conducted under controlled (laboratory) conditions have demonstrated that soil complexation with an EDTA solution can significantly enhance the phytoremediation potential of certain plants, particularly increasing lead accumulation in maize [6]. However, it is important to note that in these controlled studies, in addition to EDTA soil complexation, the soil pH was deliberately lowered using an $Al_2(SO_4)_3$ solution, which was not the case in the present research [6].

2. EXPERIMENTAL PART

Experimental soil plots of 300 m² each were selected at three locations in the Zenica area (Gradišće, Podbrežje, and Tetovo). Each experimental plot was divided into two sections, where maize, Swiss chard, and alfalfa were sown from seed. In one section of each plot, the soil was complexed with a 0.1 M EDTA solution (from the sowing period to the late growth stage), while in the other section, no soil complexation was performed. At the end of the growth period, plant material was manually sampled (aboveground plant parts along with the root), packed in plastic bags on-site, and transported to the laboratory. Soil sampling was conducted by Article 35 of the Regulation on the Determination of Permissible Quantities of Harmful and Hazardous Substances in Soil and Methods for Their Testing (*Official Gazette of the Federation of Bosnia and Herzegovina*, No. 72/09), while soil sample preparation followed Article 36 of the same regulation. A composite soil sample (~2 kg) was collected from 10 to 20 individual samples, taken using a chromed soil probe and plastic hand tools. Soil samples for laboratory analysis were taken from a depth of 0–20 cm. Determination of the total and available content of heavy metals (Zn, Ni, Pb, Cd, Cr, Cu) was performed using an AAS method (using an atomic absorption spectrometer,

PERKIN ELMER 3110). Chemical analysis of heavy metals was done according to standard ISO 11 466. The above analyses were carried out at the "Kemal Kapetanović" Institute at the University of Zenica.

3. RESULTS AND DISCUSSION

The objective of this study is to determine whether soil complexation with an aqueous EDTA solution contributes to an increased uptake of selected heavy metals from the soil into selected plant species (enhancing the phytoremediation potential of plants) under real environmental conditions. Tables 1 and 2 present data on heavy metal concentrations in soil samples (Table 1) and plant material (Table 2). Table 1 provides data for analyzing the effect of soil complexation on the uptake of selected heavy metals by plants indirectly, by comparing heavy metal content in non-complexed and EDTA-complexed soil across different plots. Table 2 provides data for analyzing the effect of soil complexation on the uptake of selected heavy metals by plants directly, by comparing heavy metal content in plants grown in non-complexed and EDTA-complexed soil across different plots.

Table 1. Heavy metal concentrations in soil samples after plant material removal ($mgkg^{-1}$)

Heavy metals	ZPK	ZPKE	ZTK	ZTKE	ZGK	ZGKE	ZPL	ZPLE	ZTL	ZTLE	ZGL	ZGLE	ZGB	ZGBE
Zn	70	80	180	250	**140**	**120**	90	100	170	250	**120**	**110**	**100**	**80**
Ni	**220**	**200**	100	140	70	90	**210**	**190**	**140**	**120**	50	70	60	70
Pb	50	70	100	180	**220**	**80**	70	80	100	150	**80**	**70**	**70**	**60**
Cd	1	1	**2**	**1**	<1	2	1	1	1	2	1	2	1	1
Cr	260	260	70	70	**70**	**60**	**270**	**240**	70	90	70	70	**70**	**40**
Cu	30	20	50	50	40	40	30	30	50	50	**50**	**40**	40	40

Z-Soil, P-Podbrežje, T-Tetovo, G-Gradišće, K-Maize, B-Swiss Chard, L-Alfalfa, E-Complexed with EDTA

Table 2. Heavy metal concentrations in plant root samples ($mgkg^{-1}$)

Heavy metals	KP	KPE	KT	KTE	KG	KGE	LP	LPE	LT	LTE	LG	LGE	BG	BGE
Zn	<1	<1	<1	<1	<1	<1	<1	<1	<1	<1	<1	14	<1	<1
Ni	53	41	**<1**	**16**	13	<1	29	14	**11**	**14**	14	13	39	17
Pb	53	20	52	16	**13**	**14**	15	15	<1	<1	<1	<1	<1	<1
Cd	<1	<1	2	<1	<1	<1	**<1**	**3**	**1**	**3**	1	1	2	1
Cr	**26**	**41**	**<1**	**16**	13	<1	44	44	21	<1	<1	<1	<1	<1
Cu	26	20	**25**	**33**	39	29	<1	<1	<1	<1	<1	<1	<1	<1

P-Podbrežje, T-Tetovo, G-Gradišće, K-Maize, B-Swiss Chard, L-Alfalfa, E-Complexed with EDTA

Analyzing the effect of soil complexation on the uptake of selected heavy metals by plants, indirectly through heavy metal content in the soil, the bolded results in Table 1 show that complexation with the EDTA solution had the greatest effect on soil samples from the Gradišće location, when analyzing all three plant species and all heavy metals. At the Gradišće location, it was observed that the concentration of heavy metals in the soil complexed with the EDTA solution decreased in nine out of the eighteen comparisons, when comparing samples from non-complexed soil with those from EDTA-complexed soil. In four of the eighteen comparisons, there were no changes in concentration, while in five comparisons, a counter-effect was recorded, meaning a reduction in the uptake of selected heavy metals by the plants. At the other locations (Podbrežje and Tetovo), soil complexation did not show the desired effect. One possible reason for the more significant impact of soil complexation on the uptake of selected heavy metals at the Gradišće location could be the soil pH (Tables 3 and 4). The soil from Gradišće shows slightly lower pH

values compared to the soils from Tetovo and Podbrežje. The solubility of heavy metal compounds increases with lower pH, which in turn increases their mobility in the soil in this case [7]. Analyzing the effect of soil complexation on the uptake of selected heavy metals by plants, directly through
heavy metal content in the plants, the bolded results from Table 2 show that complexation with the EDTA solution did not affect increasing the uptake of selected heavy metals by the plants (phytoremediation potential) in the majority of the analyzed samples. These results were unexpected, given that literature data suggests that soil complexation with an EDTA solution can significantly increase the accumulation of certain heavy metals in specific plant species, particularly the increased accumulation of lead in maize [6]. One of the key reasons for the reduced mobility of heavy metals from the soil into plant material is the alkaline soil present at all three locations (Table 3).

Table 3. pH values of soil samples before planting (initial condition)

pH values	ZP	ZT	ZG
pH in H_2O	8.27	8.32	8.10
pH in KCl	7.35	7.66	7.34

P-Podbrežje, T-Tetovo, G-Gradišće

As mentioned, the pH value has a significant impact on the mobility of heavy metals in the soil, and consequently, on the availability of metals to plants. Reducing the pH by one unit increases the solubility, and thus the mobility, of heavy metals in the soil, such as zinc, cadmium, and nickel, by two times [7, 8]. Changing the pH value alters the solubility of these metals, whether they precipitate (usually with an increase in pH) or dissolve from poorly soluble oxides or hydroxides, forming inorganic and organic complexes in the soil. The mobility of lead increases when the pH value drops below 6.5 [9]. Complexing the soil with the EDTA solution did not significantly decrease the soil pH at all locations (Table 4) when compared to the pH values of the soil in its initial condition (Table 3).

Table 4. pH values of soil samples after removal of plant material

Sample	pH in H_2O	pH in KCl
ZPK	8.0	7.6
ZPLE	8.0	7.6
ZPKE	8.1	7.5
ZPL	8.1	7.5
ZTL	8.1	7.8
ZTB	8.0	7.6
ZTLE	8.0	7.7
ZTK	8.0	7.8
ZTKE	8.1	7.6
ZGB	8.0	7.6
ZGBE	8.0	7.7
ZGL	8.0	7.5
ZGLE	7.8	7.5
ZGK	8.1	7.7
ZGKE	8.1	7.7

Z-Soil, P-Podbrežje, T-Tetovo, G-Gradišće, K-Maize, B-Swiss Chard, L-Alfalfa, E- Complexed with EDTA

By conducting experiments in controlled laboratory conditions, the soil in pots was further acidified with an $Al_2(SO_4)_3$ solution [6]. On large land areas, under uncontrolled conditions, it is almost impossible to acidify the soil to the desired pH value. We believe that much better effects in terms of heavy metal mobility in the soil, and thus metal availability to plants, would be achieved if soil parcels with acidic soil were selected.

4. CONCLUSIONS

The goal of the research conducted in this study was to determine whether soil complexation with an EDTA solution contributed to increasing the uptake of selected heavy metals from soil into selected plants, all under real environmental conditions. Analyzing the effect of soil complexation on the uptake of selected heavy metals in the plants, directly through the heavy metal content in the plants, the results show that soil

complexation with the EDTA solution did not have an effect on increasing the uptake of selected heavy metals by the plants (phytoremediation potential) in the majority of analyzed samples. One of the key reasons for the reduced mobility of heavy metals from the soil into plant material is the alkaline soil at all three study locations, with a pH > 8. The mobility of heavy metals is much higher in acidic soils than in alkaline ones. Soil complexation with the EDTA solution did not significantly affect the reduction of soil pH. Possible evidence for this claim is provided by the bolded results in Table 1, which show that soil complexation with the EDTA solution had the greatest effect on soil samples from the Gradišće location, which, in turn, showed a slightly lower pH value compared to the soil pH at the other places.

The general conclusions related to the conducted research are as follows:

- The effect of significantly increasing the mobility of certain heavy metals in the soil, and consequently the availability of metals in certain plants, through soil complexation with an EDTA solution is more likely to occur under controlled laboratory conditions, where it is possible to significantly lower the soil pH, as demonstrated in some studies.
- The effect of increasing the mobility of certain heavy metals in the soil, and thus the availability of metals in certain plants, through soil complexation with an EDTA solution, is likely possible even under uncontrolled conditions, but only in acidic soils. This requires further investigation, and existing literature supports this possibility.

Acknowledgments

This work was supported by the Federal Bosnia and Herzegovina Environmental Protection Fund and was carried out within the framework of the project „Study of the effect of chelate addition to the phytoremediation potential of plants at soils contaminated with heavy metals" (Grant no. 01-09-2-3535/2024, dated 16.07.2024).

Conflicts of Interest

The authors declare no conflict of interest.

5. REFERENCES

[1] L. Lianwen, L. Wei, S. Weiping, G. Mingxin: Remediation techniques for heavy metal-contaminated soils: Principles and applicability, *Science of the Total Environment*, 633 (2018), pp. 206-219,

[2] S. Hemen, Metal Hyperaccumulation in Plants: A Review Focusing on Phytoremediation Technology, *Journal of Environmental Science and Technology*, 4 (2011), pp. 118-138

[3] M. M. Lasat, Phytoextraction of Toxic Metals: A Review of Biological Mechanisms, *Journal of Environmental Quality,* 31 (2002), pp. 109-120

[4] S. Ashraf, Q. Ali, Z.A. Zahir, S. Ashraf, H. N. Asghar, Phytoremediation: Environmentally sustainable way for reclamation of heavy metal polluted soils. *Ecotoxicol. Environ. Saf.* 174 (2019), pp. 714-727

[5] C. Cluis: Junk-greedy greens: phytoremediation as a new option for soil decontamination, *BioTech. J.*, 2 (2004), pp. 60-67

[6] A. Pašalić, *Primjena fitoremedijacije u procesu dekontaminacije tla od teških metal*a, [Master's thesis], University of Zenica, University of Zenica, 2015

[7] N. J. Barrow, Comparing the effects of pH on the sorption of metals by soil and by goethite, and on uptake by plants, *Eur. J. Soil Sci.*, 49 (1998), pp. 683-692

[8] F. Bikić, A. Pašalić, Influence of Soil pH and Addition of a Complexing Agent on the Cadmium Content in Certain Plants, *Kem. Ind.*, 65 (2016) 7-8, pp. 375–378.

[9] A. E. Boekhold, E. J. M. Temminghoff, S. E. A. Vanderzee, Influence of electrolyte composition and pH on cadmium sorption by an acid sandy soil., *J. Soil Sci.,* 44 (1993), pp. 85-96

JST&M 8(2025), 22 – 27
DOI: 10.57131/jstm.2025.8.4

Preliminary communication

INFLUENCE OF CORROSION ON MECHANICAL CHARACTERISTICS OF STEEL SAMPLE (42CrMo4)

Stanica Nedović[1], Ana Alil[2], Sanja Martinović[2], Tatjana Volkov Husović[3]

[1]University of Montenegro, Maritime Faculty, Kotor, Montenegro, [2]University of Belgrade, Institute of Chemistry, Technology and Metallurgy – National Institute of the Republic of Serbia, Belgrade, Serbia, [3]University of Belgrade. Faculty of Technology and Metallurgy, Belgrade, Serbia

ABSTRACT

Specific environmental conditions, such as marine environments, often influence steel applications in marine industries. These conditions are commonly simulated using a NaCl solution in order to simplify the study and eliminate the complexities of seawater's chemical and biological variability. In this study, 42CrMo4 steel samples, a widely utilized material in components subjected to static and dynamic stresses found in vehicles, engines, and machinery, were selected for analysis due to their susceptibility to various forms of corrosion. The corrosion behavior of the samples was monitored using mass loss and corrosion rate. The results were then correlated with changes in mechanical properties, including tensile strength and Brinell hardness. The study provides insight into how corrosion impacts the degradation of mechanical properties.

Keywords: steel sample, corrosion behavior, mechanical properties

Corresponding Author:
Stanica Nedović
University of Montenegro, Maritime Faculty
Put I Bokeljske brigare 44, Kotor, Montengero
E-mail address: snedovic335@gmail.com

1. INTRODUCTION

The corrosion behaviour of various materials is of great importance, particularly for metallic materials, with different types of steel being the most commonly used. Different environmental conditions can induce corrosion. The influence of different fluids and gases that cause corrosion is well studied [1-3]. The process of corrosion influences the degradation of mechanical properties, so monitoring the level of material degradation is important to predict the materials' lifetime and reliability in engineering conditions. In order to assess the degradation level caused by corrosion, many different methods have been developed [4-6].

These methods are based on different approaches and can be divided into seven groups [4-6]:

1. Weight Loss Coupons
2. Electrical Resistance Monitoring
3. Electrochemical Methods
4. Hydrogen Monitoring
5. CEION
6. Non-Destructive Testing (NDT) Techniques
7. Analytical Techniques

WEIGHT LOSS COUPONS: The first technique for determining how corrosive a material is to its surroundings is weight loss coupon monitoring, which entails exposing a specimen (coupon) of the material to the environment for a predetermined amount of time and then measuring the weight loss

that results. The coupons may take the shape of discs, rods, plates, or any other practical form.

ELECTRICAL RESISTANCE (ER) MONITORING: One of the most used methods of corrosion monitoring is the ER method, which measures a metal element's resistance change as it corrodes in a process environment. Corrosion causes the element's cross-sectional area to shrink, which raises the electrical resistance. The element is often a wire, strip, or tube, and a change in resistance is proportional to an increase in corrosion if the corrosion is approximately uniform. Subsequent observations can be used to estimate the overall deterioration over time. An average corrosion rate can be calculated using a straightforward calculation.

ELECTROCHEMICAL METHODS: There are several electrochemical techniques for corrosion monitoring, which is not surprising given that corrosion is an electrochemical process. Galvanic monitoring, commonly referred to as zero resistance amperometry, and linear polarization resistance monitoring are the two electrochemical methods that are most frequently employed. The primary distinction between electrochemical and ER methods is that the former provides information on the rate of material loss, while the latter provides information on the total amount of material lost.

HYDROGEN MONITORING: Since the discovery of hydrogen indicates that corrosion is occurring or has occurred, hydrogen monitoring is a crucial component of corrosion monitoring. The production of hydrogen is a major concern, especially when plants are exposed to wet sour gas (H_2S) or acidic environments. In these circumstances, hydrogen may be immediately absorbed into the plant's structure, leading to scorching, embitterment, stress corrosion, cracking, and other issues caused by hydrogen. There are hydrogen monitoring probes that can be placed within the plant to measure its hydrogen content or, on the other hand, mounted on the outside of the plant in a saddle mode to detect hydrogen diffusion.

CEION: The resolution of the new ratiometric metal loss measurement tool CEION is at least 100 times higher than that of the current ER-based instruments. It is perfect for keeping an eye on systems that produce and process oil and gas. A technology that can function without maintenance in between scheduled shutdowns and drive an inhibitor pump's real-time control loop. Additionally, CEIONTM is the preferred technology for sub-surface and sub-sea applications where quick reaction is still crucial, but access and dependability are crucial. A particular collection of sensor designs has been created specifically for CEION's use in assessing sand erosion in producing systems.

NON-DESTRUCTIVE TESTING (NDT) TECHNIQUES: There is a wide variety of NDT methods that supplement the "instrumentation" methods that were previously discussed. These include eddy current measurement, radiography, thermography, ultrasonics, and many more. These methods are typically found in the field of plant inspection.

ANALYTICAL TECHNIQUES: The chemistry of the process fluid is examined using a variety of analytical techniques. Typically, this entails extracting fluid samples for examination in a lab. This section includes areas of interest like temperature, conductivity, pH, oxygen, iron and chloride counts, and flow measurements.

In this paper, the influence of the marine environment using a usual approach of testing in NaCl solution was studied [7]. Corrosion behaviour was monitored by measuring mass loss and mass loss rate, as well as changes in selected materials' properties during immersion in NaCl solution. Monitored material mechanical properties were: tensile strength (R_m), yield point ($R_{p0.2}$), and Brinell hardness. The time of immersion was from 0 to 120 days.

2. MATERIAL

The material that was tested in this research is low alloy steel 42CrMo4, processed by classical casting - as cast. The chemical composition is given in Table 1. The steel was delivered as hot rolled plates with dimensions of 10 mm × 1000 mm × 2000 mm. All 42CrMo4 low alloy steel samples were not heat treated further for testing.

References in the text are placed in square brackets; separate multiple references with a comma without a space, for example [3,4] or [3-9].

Table 1. Chemical composition 42CrMo4 low alloy steel

	42CrMo4										
Element (wt. %)	C	Cr	Mo	Mn	Si	Ni	Cu	Al	S	P	Fe
	0.40	0.93	0.20	0.65	0.29	0.003	0.04	0.04	0.003	0.009	Bal.

3. METHODS

The corrosion behaviour of structural steel 42CrMo4 was investigated by immersion in a 3.5% NaCl solution according to standard ISO 11130:2017 (E) [7]. Before and after each interval of the corrosion immersion, the mass of the samples was measured using an analytical balance with an accuracy of ± 0.1 mg. Mass loss and corrosion rates are measured and calculated using standard procedures.

The degree or level of corrosion was measured as the mass loss of the steel samples before and after the corrosion tests. The samples were weighed, and the mass loss was calculated using Equation (1) [8,9].

$$W\ (g) = Mi - Mf \quad (1)$$

Where Mi and Mf are the masses (in grams) of the sample before and after corrosion experiments, respectively.

The initial total surface area of the specimen (making corrections for the areas associated with mounting holes) and the mass lost during the test are determined. The average corrosion rate (according to ASTM Standard [7]) may then be obtained using equation (2).

$$CR = (K \times W)/(A \times T \times D) \quad (2)$$

Where CR is corrosion rate in mm/year, K is a constant equal to 8.76 × 104 mm/year, T is time of exposure in hours, A is the area in cm^2, W is the mass loss in grams, and D is the density of steel in g/cm^3.

Mechanical properties were monitored using standard laboratory procedures: MEST EN 6892-1:2018 [10] and SRPS EN ISO 6506-1:2016 [11].

4. RESULTS AND DISCUSSION

Mass loss and mass loss rate were monitored for corrosion behaviour description. In Figure 1, the obtained results for mass loss and mass loss rate are presented.

It can be observed in Figure 1 that the mass loss and corrosion rate increase with the time of immersion, almost as a linear correlation. The results pointed out degradation of the sample, and the results of this degradation on the mechanical properties behaviour are given in Figure 2.

Changes in mechanical properties during the immersion time of 120 days were not significant. Yield point ($R_{p0.2}$) is during testing between 502 and 511 MPa, which is a small increase due to the starting value (479 MPa) (Figure 2). Similar behaviour is observed for tensile strength (R_m), as values vary from 691 to 708 MPa compared to the starting 676 MPa. Brinell hardness showed values from 210 to 217, compared to a starting value below 200. Mechanical characteristics monitored, tensile and yield strength did not exhibit significant changes during testing, as well as Brinell hardness (Figure 2).

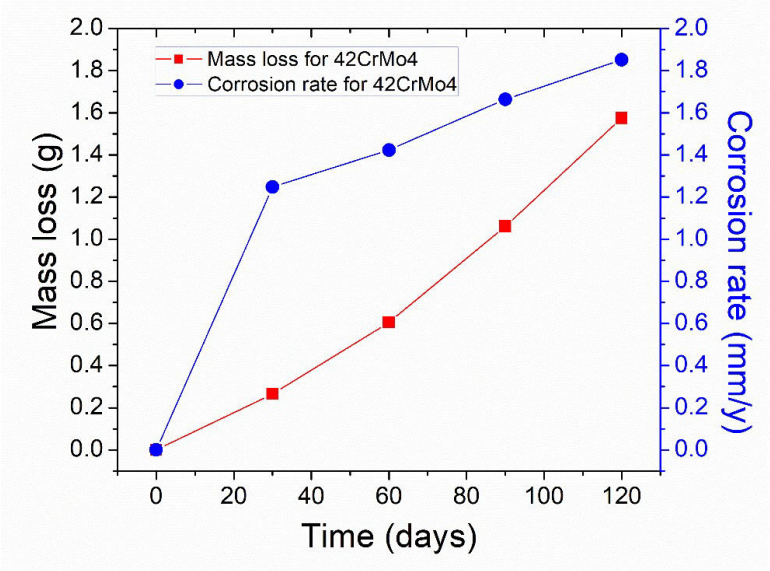

Figure 1. Mass loss and corrosion rate for 42CrMo4

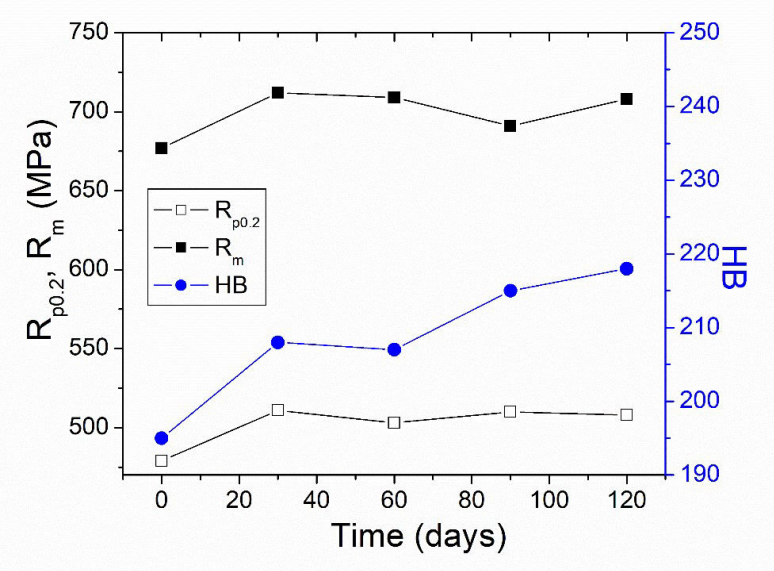

Figure 2. Mechanical properties (yield point ($R_{p0.2}$), tensile strength (R_m) and Brinell hardness) versus time of immersion

However, the influence of immersion and corrosion process on yield strength is mild, decreasing, as well as for tensile strength. Brinell hardness was mildly increased compared to starting values (Fig.2). These results can be explained using chemical analysis in order to discuss the formed oxides and their influence on mechanical properties. Also, the time of immersion could be extended to get better insight into mechanical behaviour during corrosion testing related to longer times of immersion. The diagrams presented in Figure 3 illustrate the correlation between mass loss, mass loss rate, tensile strength (R_m), yield point ($R_{p0.2}$), and Brinell hardness as a function of immersion time.

The cumulative graphs presented in Fig. 3 can be useful for monitoring mass loss and mass loss rate changes to easily and quickly predict the expected changes in mechanical

properties, as well as for different immersion times. The combination of easily measured parameters (mass loss and mass loss rate) can be combined with other relevant parameters significant for corrosion monitoring (surface level of degradation, for example).

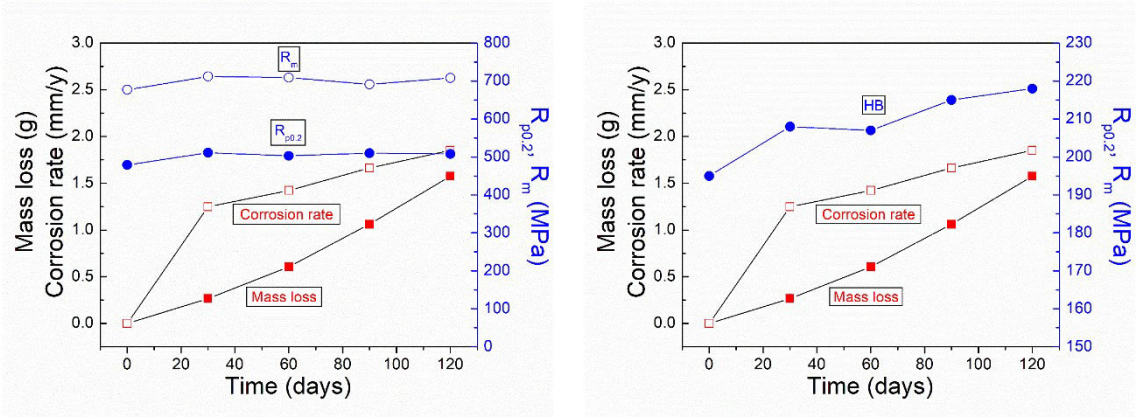

a) b)

Figure 3. Mass loss, mass loss rate and tensile strength (R_m), yield point ($R_{p0.2}$) (a) and Brinell hardness (b) as a function of immersion time

5. CONCLUSION

The corrosion behaviour of the steel sample in NaCl solution was monitored using mass loss and mass loss rate, as well as monitoring of changes in selected material mechanical properties: tensile strength (R_m), yield point ($R_{p0.2}$) and Brinell hardness. The total time of immersion was 120 days.

The results obtained give good insight into the sample behaviour during different periods of immersion. This relationship between mass loss and mass loss rate (corrosion rate), which can be easily measured and monitored, can be related to the degradation of material properties and can be used for modelling appropriate and reliable models for mechanical properties degradation due to corrosion. These models could lead to models for the prediction of the lifetime of a sample/material based on different parameter changes.

Obtained results for mechanical properties changes pointed out that for the time of immersion of 120 days, there were no significant changes. However, longer immersion times are expected to have a more significant influence on the degradation of mechanical properties. Further experiments will take into account longer immersion times and their influence on mechanical characteristics.

Acknowledgements:

This work was supported by the Ministry of Science, Technological Development and Innovation of the Republic of Serbia (Contract No. 451-03-136/2025-03/200135 and 451-03-136/2025-03/200026)

Conflicts of Interest

The authors declare no conflict of interest.

6. REFERENCES

[1] S. Harsimran, K. Santosh, K. Rakesh, Overview of corrosion and its control a critical review, Proceedings on Engineering Sciences, Faculty of Engineering, University of Kragujevac, pp. 13-24

[2] M. Wasim, S. Shoaib, N.M. Mubarak, Factors influencing corrosion of metal pipes in soils, *Environmental Chemistry Letters*, 16 (2018), pp. 861–879

[3] D. Nieves-Mendoza, C. Gaona-Tiburcio, H. L. Z. Hervert, R.C. Mendez, P. Castro-Borges, A. T. Borunda, P. Zambrano Robledo, F. Almeraya-Calderón, Identifying Factors Influencing the Corrosion Rate of Steel Using Nonparametric

Statistics, *International Journal of Electrochemical Science*, 7 (2012), pp. 6343-6352

[4] Corr Science., Corrosion Science Technique. [Online]. 2011. Dostupno na: http://www.corrscience.com/products/corrosion/intro-to-corrosion/corrosion-monitoring-techniques/. [17.6.2025]

[5] A. Berradja, *Electrochemical Techniques for Corrosion and Tribocorrosion Monitoring: Methods for the Assessment of Corrosion Rates. Corrosion Inhibitors,* [Online]. IntechOpen. Dostupno na: https://doi:10.5772/intechopen.86743 [17.6.2025], 2019

[6] N. G. Rathod ASCE, N. C. Moharana, Advanced methods of corrosioon monitoring-A review, *International Journal of Research in Engineering and Technology*, 4 (2015), pp. 413-420

[7] ASTM Committee G-1 on corrosion of metals, ASTM International, Standard practice for preparing, cleaning, and evaluating corrosion test specimens, West Conshohocken: PA, USA, 2003

[8] S. Martinović, A. Alil, S. Milićević, D. Živojinović, T. Volkov Husović, Morphological Assessment of Cavitation Caused Damage of Cordierite and Zircon Based Materials Using Principal Component Analysis*, Engineering Failure Analysis,* 147 (2023)

[9] M. Vlahović, A. Alil, A. Devečerski, D. Živojinović, T. Volkov-Husović, Non-Destructive Examination for Cavitation Resistance of Talc-Based Refractories with Different Zeolite Types Intended for Protective Coatings, *Materials,* 16 (2023), pp. 1-20

[10] MEST EN ISO 6892-1, ISO 6892-1:2016, Metallic materials - Tensile testing - Part 1: Method of test at room temperature, 2016

[11] SRPS EN ISO 6506-1, ISO 6506-1:2016, Metallic materials - Brinell hardness test - Part 1: Test method, 2016

JST&M 8(2025), 28 – 35
DOI: 10.57131/jstm.2025.8.5

Original scientific paper

INVESTIGATION OF THE PORTEVIN-LE CHATELIER EFFECT IN AlMg ALLOYS: EFFECT OF TESTING RATE

Ivan Jandrlić, Lorena Mrkobrada

Faculty of Metallurgy, University of Zagreb, Sisak

ABSTRACT

The study investigates the Portevin–Le Chatelier (PLC) effect in the cold-rolled Al-Mg alloy EN AW-5754. The tensile tests were performed on dog bone specimens at test speeds of 10, 20, and 50 mm/min. Digital image correlation (DIC) and infrared thermography were used to monitor strain rate and temperature changes. The results showed a strong correlation between PLC line propagation, strain rate variations, and temperature changes. Regardless of the test speed, the characteristic jagged shape of the material was observed due to the PLC effect. As the deformation progressed, both the strain rate and the temperature increased, with the changes being more pronounced at higher test speeds. DIC and infrared images show that temperature peaks correspond to moments of increased plastic deformation and sudden drops in strain rate. The formation of overlapping PLC lines also showed the random and unpredictable nature of the phenomenon.

Keywords: AlMg alloy, Portevin-Le Chatelier effect, testing rate, Digital Image Correlation (DIC)

Corresponding Author:
Ivan Jandrlić,
Faculty of Metallurgy, University of Zagreb
Aleja narodnih heroja 3, Sisak, Croatia
Tel.: +385 44 533 378
E-mail address: ijandrli@simet.hr

1. INTRODUCTION

The Aluminum alloys of the 5xxx series, which primarily contain magnesium as the main alloying element, are highly valued in the automotive industry due to their excellent strength-to-weight ratio, corrosion resistance, weldability, and formability [1, 2]. These alloys are increasingly used in the automotive industry, especially in body construction, where their ability to reduce vehicle weight and fuel consumption is crucial [2]. Due to their corrosion resistance, low weight, hardenability, and high recycling potential, aluminum alloys are widely used in various industries [3]. The addition of magnesium improves the strength of these alloys through hardening, which occurs when dislocations interact with each other or with precipitates of dissolved elements and different phases [2, 4]. As a result, the AlMg alloys of the 5xxx series are prone to unstable plastic flow under certain deformation conditions. This unstable flow manifests itself in the form of the Portevin-Le Chatelier (PLC) effect, which causes localized deformation that often occurs in the form of deformation bands [5]. The PLC effect causes the formation of localized deformation bands, which manifest as repetitive serrations in the stress-strain curve during tensile testing [6, 7]. Depending on the nature of serrations, three main types of deformation bands A, B, and C are formed, the appearance of which is influenced by the strain rate and temperature (Figure 1). In some cases, rarer

deformation bands such as types D and E have also been reported in the literature [8, 9].

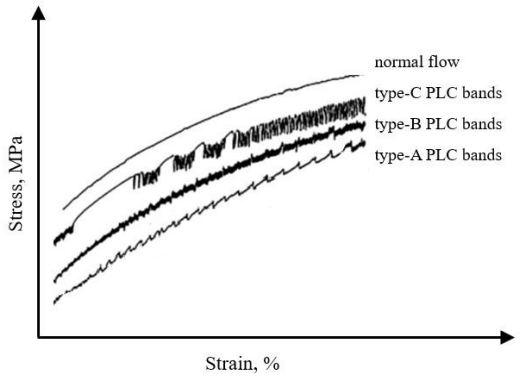

Figure 1. Three main types of deformation lines of the PLC effect

The occurrence of the PLC effect poses a challenge from both optical and structural perspectives. Aluminum alloy products where the PLC effect occurs during deformation can develop rough and undesirable surface marks. These surface irregularities can act as initial cracks and stress concentrators, Initial cracks and stress concentrators may lead to fatigue-induced material failure during subsequent processing stages [10, 11]. Furthermore, while the PLC effect leads to increased stress, hardness, tensile strength, and strain hardening rate, it also reduces ductility, toughness, and sensitivity to strain rates [11]. Since the PLC effect can be observed in a variety of aluminum alloys, AlMg alloys are often chosen as the material for studying these phenomena [12]. Tensile testing is the most common method to investigate the presence of the PLC effect in these alloys [13]. On the microscopic scale, the widely accepted explanation for the PLC effect is based on the Cottrell model, also known as dynamic strain aging (DSA) [14, 15]. When a sufficient number of solute atoms accumulate around dislocations, their movement is constrained. This restriction leads to less mobile dislocations and a corresponding increase in stress. Once the stress level becomes high enough to allow the release or multiplication of these immobilized dislocations, a sudden drop in stress occurs. Recurring stress fluctuations interrupt the strain hardening curve, appearing as serrations on the stress-strain diagram [14, 15, 16].

Among the most important factors influencing the occurrence of the PLC effect are the composition of the alloy and the concentration of solute elements [17, 18]. Precipitates play a notable role in enhancing deformation localization and promoting the PLC effect during plastic deformation. Dislocation density and grain size are also important factors contributing to the manifestation of the PLC phenomenon [8], although their influence is not always pronounced. Researchers have investigated the effect of both temperature and strain rate on AlMg alloys with different magnesium contents [9, 19]. Their results showed that these two parameters substantially influence the occurrence of DSA.

As for strain rate, the PLC effect shows considerable sensitivity due to the interplay between moving dislocations and diffusing solute atoms. In AlMg alloys, this relationship is often characterized by a negative strain rate sensitivity (nSRS), where an increase in strain rate leads to a stress drop — an unusual behavior for metallic materials [9, 19]. It is noteworthy that lower strain rates tend to lead to higher amplitude serrations, while higher strain rates lead to more damped stress fluctuations. This behavior can be attributed to the fact that the solute atoms have more time to interact with the dislocations at lower strain rates, which enhances the serrated flow. Conversely, the limited diffusion of solutes at higher rates weakens or even eliminates the PLC effect.

The manifestation of the PLC effect arises from a complex interplay of variables, underscoring the need for continued research to elucidate the underlying mechanisms and to identify processing

conditions under which this phenomenon can be minimized or avoided. During static tensile testing of metals, the mechanical energy that leads to plastic deformation is converted into heat. This causes an increase in the material temperature and is often observed in various studies using infrared cameras [20, 21]. The Portevin–Le Chatelier (PLC) effect is a major contributor to this phenomenon. The PLC effect is associated with localized plastic deformation, where strain is concentrated in narrow deformation bands. As the dislocations are temporarily held in place by solute atoms (e.g. Mg in AlMg alloys), the stress builds up until the dislocations break free and cause a sudden surge of movement. This abrupt release of energy is converted into heat, which generates a local temperature change in the samples. The cyclic pinning and unpinning of dislocations in the PLC regime can therefore lead to temperature peaks, even in a nominally isothermal test. By using infrared thermography to measure these local temperature increases during PLC events, a clear correlation between stress serrations and temperature rise was confirmed [22, 23].

The occurrence of the PLC effect is a complex phenomenon influenced by numerous factors, necessitating further research to deepen our understanding of its underlying mechanisms. The primary objective of this study was to examine the effect of testing rate on the PLC behavior in an AlMg alloy, as well as its impact on temperature variations during the initiation and propagation of the PLC bands.

2. MATERIAL AND RESEARCH

For the experiment, samples were taken from cold-rolled sheets of the Al-Mg alloy EN AW-5754. By CNC machining, dog bone specimens were produced for the tensile test with the dimensions of the test part of 50 x 20 mm and 3 mm thickness.

To enable temperature and deformation measurements, the specimens were properly prepared by first applying a black matte spray coating, followed by a white speckle pattern necessary for DIC analysis (Figure 2).

Figure 2. Dog-bone specimen prepared for simultaneous tensile strength – DIC - thermography testing

The DIC analysis was performed with the ARAMIS system, Figure 3, and the thermography with the Jenoptik VarioCAM® IR camera, Figure 4. In the DIC analysis of the recorded changes during the appearance and propagation of the PLC lines, the change in the strain rate of the lines themselves was recorded. At the same time, the temperature changes caused by the deformation during the propagation of the PLC lines were monitored with the infrared camera.

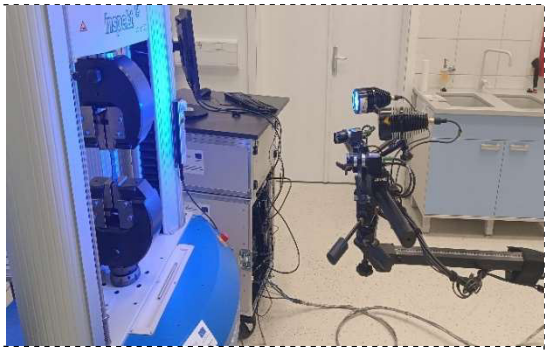

Figure 3. Experimental setup of ARAMIS system and Hegewald & Peschke inspect table 100 tensile testing machine

Figure 4. IR camera Jenoptik VarioCAM®

The tensile test was performed using a universal testing machine (Figure 3). During the tensile test, the deformation and the temperature change were recorded simultaneously. To determine the influence of the test speed on the temperature changes during the formation and propagation of the PLC, the tests were carried out at speeds of 10 mm/min, 20 mm/min, and 50 mm/min.

3. RESULTS AND DISCUSSION

Figure 5 shows the stress-strain curves obtained from static tensile tests at all three test speeds used. The plotted graphs, including the enlarged segment in Figure 5, clearly illustrate the jagged deformation characteristic of the material caused by the PLC phenomenon. These results indicate that the fundamental nature of the PLC effect remains unchanged as the test rate increases. During the static tensile test, the surface of the samples was continuously recorded with an optical camera and an infrared camera, and all images were subsequently analyzed. Figure 6 shows the DIC analysis of the strain rate and IR temperature changes of the PLC lines during the tensile test at a speed of 50 mm/min.

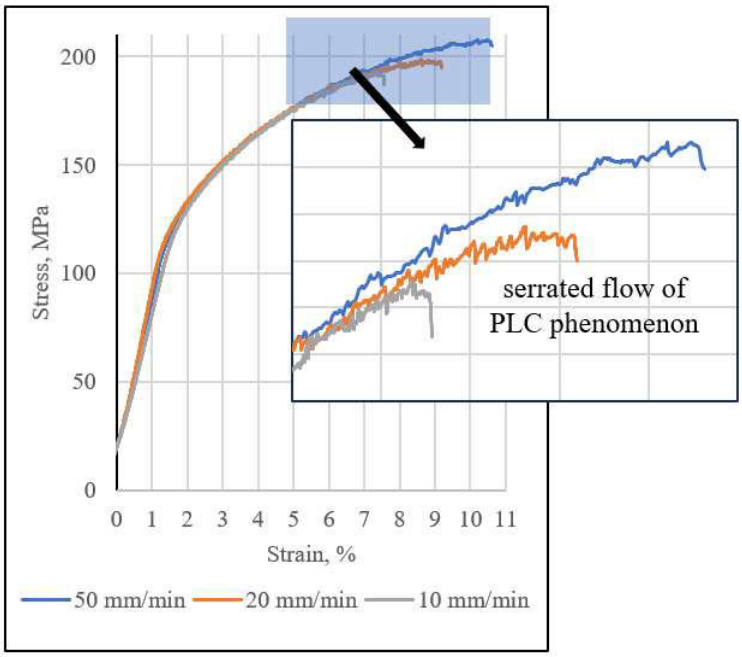

Figure 5. Tensile test results with visible occurrence of the PLC effect

Figure 6a shows a DIC analysis of the PLC lines during the tensile test, which reveals the propagation of a PLC line throughout the sample. Towards the end of the observed period, a second line appears from above, intersecting the first and forming an X-shaped pattern. From this, you can see that the phenomenon itself is very random and unpredictable. Figure 6b shows the same sample taken with an infrared camera. It shows the same phenomenon and correlates with the DIC recording. This confirms that the observed temperature change is directly caused by the deformation caused by the progression of the PLC line.

Figures 7, 8, and 9 show the results of the DIC and thermographic analysis of the recorded deformations at test speeds of 10, 20, and 50 mm/min respectively.

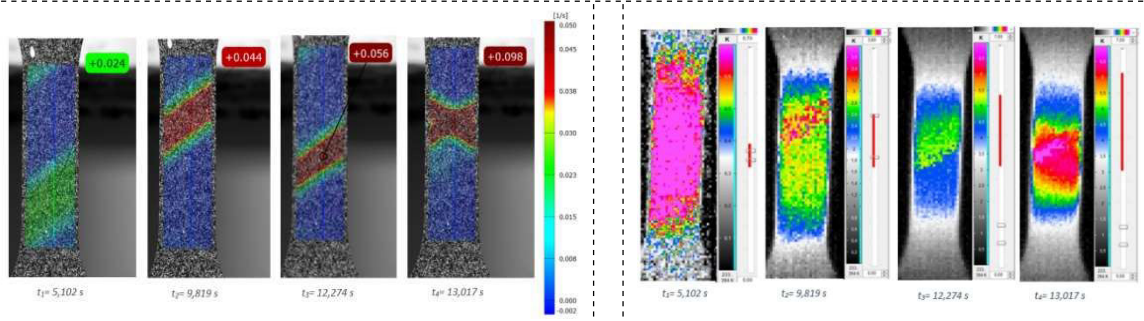

Figure 6. a) DIC representation of the propagation of the PLC line at a speed of 50 mm/min, b) Temperature changes due to the deformation of the PLC line at the same test points as DIC.

The images show comparisons of the strain rate changes and the associated temperature changes. The first thing that can be seen is that as the degree of deformation increases during the experiment, the strain rate and temperature change gradually increase. It can also be observed, as is to be expected, that as the test speed increases, the strain rate and the associated temperature rise increase more sharply.

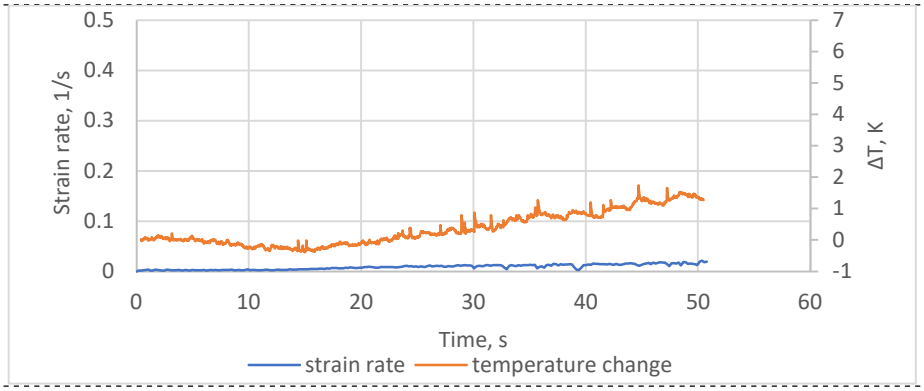

Figure 7. Comparison of change in strain rate and temperature at 10 mm/min

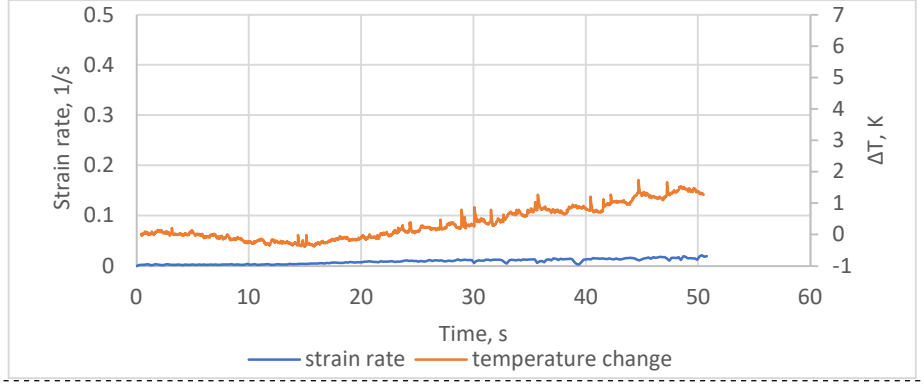

Figure 8. Comparison of change in strain rate and temperature at 20 mm/min

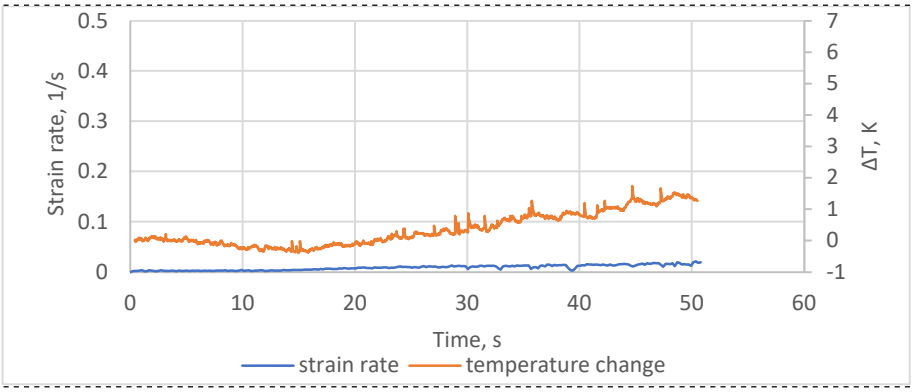

Figure 9. Comparison of change in strain rate and temperature at 50 mm/min

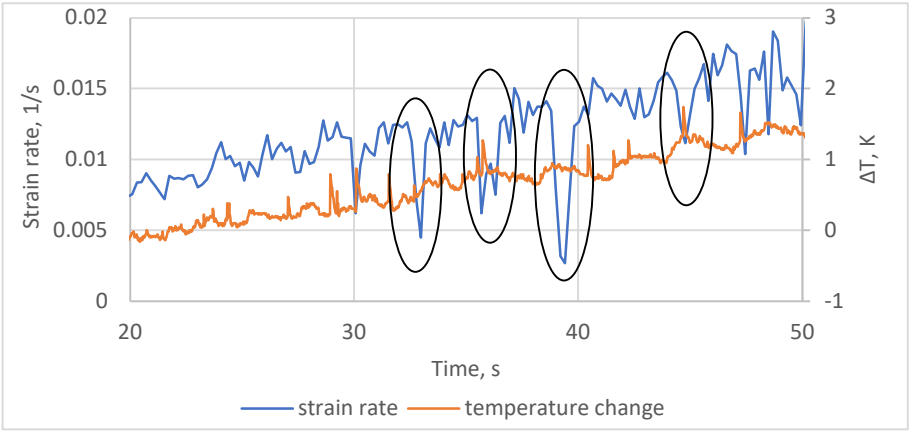

Figure 10. Segment of the comparison between the increase of strain rate and temperature at a test speed of 10 mm/min

What can be observed at all test speeds performed is the close relationship between the temperature change and the strain rate changes caused by the propagation of the PLC lines. This can be seen even more clearly from the enlarged section in Figure 10.

If you observe the changes in the strain rate closely, you can see that the strain rate of the PLC line drops suddenly at certain intervals. At the same time, it can be observed that a peak in the temperature change occurs at these moments. This can be seen at several points in Figure 10.

It is known that the increase in the temperature change is due to the work performed by the mechanical deformation, or more precisely by the plastic deformation of the sample. We can therefore assume that at the moments when we observe an increase in temperature, there is a greater plastic deformation at a constant strain rate. Consequently, we observe a decrease in the change in strain rate. To confirm this unequivocally, further investigations at other test speeds are required and a comparison must be made with the deformation amounts carried out during these periods.

4. CONCLUSION

The study confirmed a strong correlation between the propagation of the PLC bands, the variations in strain rate, and the temperature changes during the tensile test. Regardless of the test speed, the characteristic jagged curve associated with the PLC effect was consistently observed. As the deformation progressed, both the strain rate and the temperature increased, with the variations being more pronounced at higher test speeds.

Analysis of the recorded data revealed that temperature peaks coincided with abrupt drops in strain rate, indicating that localized plastic deformation was the primary cause of the observed thermal variations. Strain rate and temperature changes followed a clear trend, emphasizing the relationship between mechanical deformation and heat generation. These results suggest that the PLC effect remains essentially unchanged at different strain rates but varies in magnitude.

The formation of overlapping PLC lines showed the unpredictability of the PLC phenomenon. Further research is required to quantify the relationship between plastic deformation and temperature changes more accurately, particularly by testing at additional test speeds and comparing distribution patterns of temperature and deformation.

Acknowledgments

Investigations were performed within research project IP-124 University of Zagreb Faculty of Metallurgy, Centre for Foundry Technology—SIMET, KK.01.1.1.02.0020 and VIRTULAB—Integrated laboratory for primary and secondary raw materials, KK.01.1.1.02.0022.

Conflicts of Interest

The authors declare no conflict of interest.

5. REFERENCES

[1] D. Skejić, I. Boko, N. Torić, Aluminij kao materijal za suvremene konstrukcije. *Gradjevinar*. 67(2015) 11, pp. 1075-1085

[2] E. Romhanji, M. Popović, D. Glišić, M. Stefanović, M. Milovanović, On the Al-Mg alloy sheets for automotive application: Problems and solutions, *Metalurgija,* 10 (2024), pp. 205-216.

[3] M. Chiaberge, New Trends and Developments in Automotive System Engineering, Intech Open. E-book, 2011; doi: 10.5772/552,https://www.intechopen.com/books/19

[4] R. E. Smallman, A. H. Ngan, Work hardening and annealing, *Modern Physical Metallurgy*, 2014, pp. 443-471

[5] V. M. Farber, A. N. Morozova, V. A. Khotinov, D. I. Vichuzhanin, M. S. Karabanalov, I. A. Veretennikova, Lüders deformation in specimens made of normalized 09G2S steel, *Procedia Structural Integrity*, 40 (2021), pp. 129-135

[6] D. Zhemchuzhnikova, M. Lebyodkin, D. Yuzbekova, T. Lebedkina, A. Mogucheva, R. Kaibyshev, Interrelation between the Portevin Le-Chatelier effect and necking in AlMg alloys, *International Journal of Plasticity,* 110 (2018), pp. 95-109

[7] S. Szalai, D. Harangozó, I. Czinege, Characterisation of inhomogeneous plastic deformation of AlMg sheet metals during tensile tests, *IOP Conference Series: Materials Science and Engineering*, 903 (2020) 1, paper 012023

[8] D. A. Zhemchuzhnikova, Influence of the extreme grain size reduction on plastic deformation instability in an AlMg and AlMgScZr alloys. Materials, Université de Lorraine, 2018. Available online: http://www.culture.gouv.fr/culture/infos-pratiques/droits/protection.htm

[9] J. Xu, B. Holmedal, O. S. Hopperstad, T. Mánik, K. Marthinsen, Dynamic strain ageing in an AlMg alloy at different strain rates and temperatures: Experiments and constitutive modelling, *International journal of plasticity,* 151 (2022) 4, paper 103215.

[10] M. A. Lebyodkin., T. A. Lebedkina, The Portevin-Le Chatelier Effect and Beyond, Jamieson Brechtl; Peter K. Liaw, High-Entropy Materials: Theory, Experiments, and Applications, Springer Nature Switzerland, 2021. online https://hal.univ-lorraine.fr/hal03360977v1/file/The%20PortevinLe%20Chatelier%20Effect%20and%20Beyond_MLTL.pdf

[11] T. V. Tretyakova, M. P. Tretyakov, E. A. Chechulina, Experimental study of the Portevin-Le Chatelier effect under complex loading of Al-Mg alloy, *procedure issues. Frattura Ed Integrita Strutturale-Fracture and Structural Integrity*, 58 2021, pp. 434-441

[12] Y. Borisova, D. Yuzbekova, A. Mogucheva, Influence of phase composition on Portevin-Le Chatelier effect in Al-Mg alloys, *IOP Conference Series: Materials Science and Engineering,* 8 2019, 597: doi: 10.1088/1757-899X/597/1/012057.

[13] S. Szalai, D. Harangozó, I. Czinege, Characterisation of Inhomogeneous Plastic Deformation of AlMg Sheet Metals during Tensile Tests, *IOP Conference Series: Materials Science and Engineering,* 8 2020, 903: doi: 10.1088/1757-899X/903/1/012023.

[14] D. Yuzbekova, A. Mogucheva, Y. Borisova, R. Kaibyshev, On the mechanisms of nucleation and subsequent development of the PLC bands in an AlMg alloy, *Journal of Alloys and Compounds,* 2021, 868: doi: 10.1016/j.jallcom.2021.159135.

[15] A.H. Cottrell, Theory of dislocations, *Progress in Metal Physics*, 1953; 4: 205-264. doi: https://doi.org/10.1016/0502-8205(53)90018-5.

[16] M. Mehenni, H. Ait-Amokhtar, C. Fressengeas, Spatiotemporal correlations in the Portevin-Le Chatelier band dynamics during the type B - type C transition, *Materials Science and Engineering A*, 756 (2019) 5, pp. 313-318

[17] T. Mäkinen, P. Karppinen, M. Ovaska, L. Laurson, M. J. Alava, Propagating bands of plastic deformation in a metal alloy as critical avalanche, *Science Advances*, 6 2020 (41): doi: 10.1126/sciadv.abc7350

[18] J. Kang, L. Shi, J. Liang, B. Shalchi-Amirkhiz, C. Scott, The Influence of Specimen Geometry and Strain Rate on the Portevin-Le Chatelier Effect and Fracture in an Austenitic FeMnC TWIP Steel, *Metals*, 10 (2020) 9, pp. 1201-1201

[19] C. H. Cho, H. W. Son, J. C. Lee, K.T. Son, J.W. Lee, S. K. Hyun, Effects of high Mg content and processing parameters on Portevin-Le Chatelier and negative strain rate sensitivity effects in Al-Mg alloys. *Materials Science and Engineering A*, 779 (2016) 3, paper: 139151 doi: 10.1016/j.msea.2020.139151.

[20] I. Jandrlić, S. Rešković, T. Brlić, Distribution of stress in deformation zone of niobium micro-alloyed steel, *Metals and materials international,* 24 (2018) 4, pp. 746-751

[21] X.G. Wang, V. Crupi, X.L. Guo, Y.G. Zhao, Quantitative thermographic methodology for fatigue assessment and stress measurement, *International journal of fatigue,* 32 (2010) 12, pp. 1970-1976

[22] J. B. Le Cam, E. Robin, L. Leotoing, D. Guines, Calorimetric analysis of Portevin-Le Chatelier bands under equibiaxial loading conditions in Al-Mg alloys: Kinematics and mechanical dissipation, *Mechanics of Materials,* 105 (2017), pp. 80-88

[23] H. Qi, Q. Zhang, P. Cao, S. Fu, Thermal analyses and simulations of the type A and type B Portevin–Le Chatelier effects in an Al-Mg alloy, *Acta Materialia*, 60 (2012) 4, pp. 1647-1657

JST&M 8(2025), 36 – 42
DOI: 10.57131/jstm.2025.8.6

Original scientific paper

SYNERGY BY MOLYBDENUM AND NIOBIUM ON PERFORMANCE OF COLD WORK TOOL STEELS

Aslan Unal

Steel Test & Research Center – Quality Manager (Retired)
MATIL (Material Testing & Innovation Laboratories) A.S.,
Istanbul Technical University, Maslak, Türkiye

ABSTRACT

For the die industry, where future products have a decisive role in material selection, the subject of steel is an area of interest with high innovation potential. With new production and processing technologies that prioritize knowledge, the quality of materials has improved significantly, and these developments continue. Material selection in die design is a crucial aspect of engineering aimed at developing sustainable and effective solutions to technical challenges. Die manufacturing is open to innovation as the main input is steel. Cold work tool steels (CWTS) are frequently preferred in the die industry. Recently, in addition to traditional CWTS, next-generation CWTS systems have been introduced into use. This article examines the application of one conventional and two next-generation CWTS units as punch tools in sheet metal pressing and thread rolling die for screw manufacturing It has been observed that the new-generation CWTS offers a longer lifespan compared to the traditional one. The microstructures were investigated, and the fine and evenly distributed multiple carbide structures that they can form were evaluated using FactSage® thermodynamic software. The carbides in new-generation CWTS were also rich in molybdenum and niobium. With the use of next-generation materials, modern heat treatments, and advanced coating technologies, it is possible to design specialized products tailored to each specific application. For the innovation approach of modern tool steels in the context of cold-forming dies, traditional and new-generation Cold Work Tool Steels (CWTS) were compared in terms of chemical composition and the use of refractory metals as alloying elements, and their performances were evaluated and interpreted.

Keywords: refractory metals, tool steels, carbides

Corresponding Author:
Dr. Aslan Unal
MATIL Materials Test and Innovation Laboratories Inc.
Istanbul Technical University, Maslak, 34469 Sariyer, Istanbul, Türkiye
Tel.: +905324561380
E-mail: aslunal@gmail.com

1. INTRODUCTION

The word refractory comes from the Latin root "refractorius" and means resistant to high temperatures. Among the many elements that can alter the properties of alloy steels—whose production dates back over a century—*refractory metals* (RM) have particularly significant effects. There are various scientific and commercial studies concerning which metals should be classified as refractory metals (RM), with the number of considered elements ranging from 5 to 14. The melting points of RM are higher than their oxides. They have a body-centered cubic (BCC) structure. According to Calister, niobium, molybdenum, tungsten,

and tantalum are classified as refractory metals [1]. ASM Handbook and Habashi also include hafnium, vanadium, chromium, zirconium, and titanium [2, 3]. The International Journal of Refractory Metals and Hard Materials defines RM as metals with melting points above 1850°C [4].

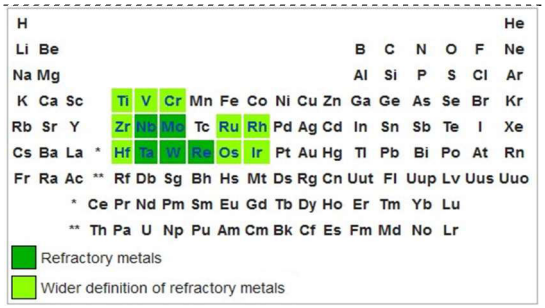

Figure 1. Refractory metals, all [5]

In steels containing both molybdenum and niobium, morphological benefits are particularly evident during thermomechanical processes applied after solidification, such as hot rolling or forging. In low-carbon steels, more successful results are obtained with the addition of boron. The total synergistic effect of niobium and molybdenum is more than the sum of the impacts of each one individually [6]. In another new study completed in 2022, where the words molybdenum, niobium, and synergy are frequently used together; by the addition of these two metals and boron as an alloying element, the gains were examined thermodynamically and phase transformations kinetically. Refined texture provided by the grain reduction effect of the Mo-Nb duo on the microstructure, the contribution of the increases in hardness and toughness properties to ultra-durable steel production was determined. The series of benefits that begin in the controlled hot rolling stage continues in heat treatments such as annealing, quenching, and tempering [7].

Mo and Nb are common elements that improve the microstructure even when used in small amounts, both alone and together. They contribute to mechanical properties with grain reduction and precipitation, providing benefits. With the carbides or carbonitrides they form, hardenability increases starting from the thermomechanical process stage [8].

When it comes to tool steel, the first thing that comes to mind is “carbide”. In all tool steels, the main priority of the alloying elements is to create wear-resistant carbide structures formed by alloying elements within the main matrix of iron. The carbides are the actors that provide different properties to tool steel compared to other types of steel. Carbides work as strength agents, but they can also act as crack initiation sites [9].

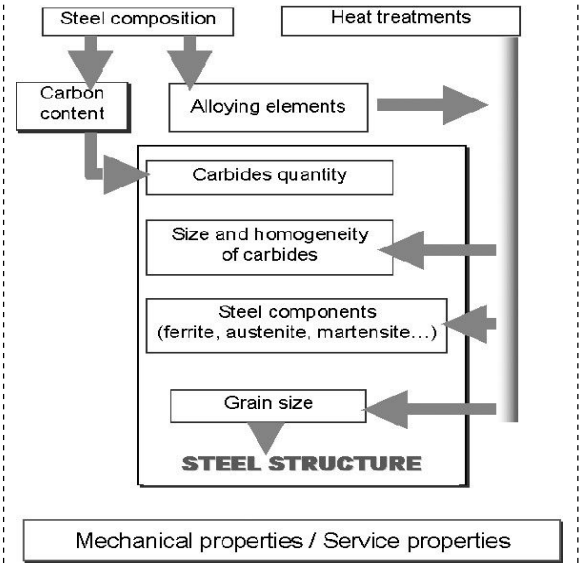

Figure 2. Carbide-structure-property relation [10]

The physical and chemical structures of carbides and how they are distributed in the matrix directly affect the mechanical properties of steel. Depending on the heat treatment and carbon content, seven types of carbides can form, generally represented by the elemental metal symbol 'M'; MC, M_2C, M_3C_2, M_5C_2, M_7C_3, M_6C, and $M_{23}C_6$. M_2C is rich in molybdenum, M_7C_3 is rich in chromium, M_6C is rich in iron and molybdenum and is found close to the outer surfaces. However, other types of carbides are found everywhere [11].

The following transformations occur during the tempering of different M_xC_y carbides;

$M_3C \rightarrow M_2C \rightarrow M_{23}C_6$, and/or (1)
$M_3C \rightarrow M_7C_3 \rightarrow M_{23}C_6$ (2)

This leads to an additional increase in wear resistance [12]. $M_{23}C_6$ is the most thermodynamically stable among Cr-containing carbides. Therefore, it is understood that $M_{23}C_6$ phases will be more durable in wear behavior [13]. To bring together the wear behavior and fracture resistance at the most appropriate point, a microstructure that provides the optimum between the hardness and fracture toughness behaviors of the different primary carbides in the steel should be provided by selecting the most suitable carbide type [14].

2. MATERIALS AND METHOD

Conventional AISI D2 series tool steels have excellent wear resistance and non-deformability, making them very useful as cold work die steels. They are widely used in cold-forming dies. Among these, D2 Steel is by far the most popular grade [15].

New Generation CWTS is offered to users with the names given by the manufacturing companies. Since not only chemical composition but also factors such as heat treatment, mechanical processing, and surface treatments affect product satisfaction, these products, which are patented and not included in the standards, are used instead of company and product names as codes C2 and K2 to avoid a positive or negative perception.

Chemical compositions of 9 products, 3 from each of three different steel types, traditional AISI D2 (1.2379) and new generation C2 and K2 steels were determined and 32 elements were measured with 0.0001% precision by ARL 8860 Optical Emission Spectrometer at R&D Center of MATIL Material Testing and Innovation Laboratories Inc. at Istanbul Technical University (ITU) according to ASTM E415, is shown at Table 1:

Table 1. Analysis of traditional D2 (1.2379) and new generation C2 and K2 steels

D2															
C	Mn	Si	S	P	Cu	Ni	Mo	Cr	V	Co	B	N	Al	Ti	W
1,4194	0,2916	0,234	0,004	0,023	0,133	0,255	0,658	11,396	0,918	0,017	0,00021	0,0177	0,026	0,002	0,028
As	Sn	Pb	Sb	Ta	Zr	Bi	Ca	Mg	Te	Zn	Ce	La	Nb	O	Fe%
0,0068	0,0065	0,002	0,007	1E-04	0,004	0,002	0,015	0,0101	0,002	0,0044	0,0001	0,0002	0,023	0,005	84,5

C2															
C	Mn	Si	S	P	Cu	Ni	Mo	Cr	V	Co	B	N	Al	Ti	W
0,7912	0,2468	0,927	0,002	0,008	0,146	0,166	1,862	7,2964	0,211	0,0167	0,00032	0,0102	0,019	0,002	0,01
As	Sn	Pb	Sb	Ta	Zr	Bi	Ca	Mg	Te	Zn	Ce	La	Nb	O	Fe%
0,0081	0,0085	0,002	0,007	1E-04	0,003	0,003	0,054	0,0096	0,001	0,0026	0,0041	0,0001	0,015	0,001	88,18

K2															
C	Mn	Si	S	P	Cu	Ni	Mo	Cr	V	Co	B	N	Al	Ti	W
0,9641	0,3802	0,775	6E-04	0,01	0,079	0,3	1,853	7,8788	0,409	0,0449	0,00045	0,0141	0,834	0,002	0,07
As	Sn	Pb	Sb	Ta	Zr	Bi	Ca	Mg	Te	Zn	Ce	La	Nb	O	Fe%
0,004	0,0059	0,002	0,009	1E-04	0,004	0,003	0,019	0,0112	0,002	0,0028	0,0043	0,0001	0,111	0,006	86,22

An analysis of all chemical compositions reveals differences between conventional and new-generation CWTS, as well as among the various types of new-generation CWTS themselves. When examined all together;

- It is seen that the manganese (Mn) and nickel (Ni) ratios are similar and close in all.
- New-generation CWTS C2 contains lower amounts of carbon, chromium, and vanadium.
- New-generation CWTS C2 contains higher amounts of silicon and molybdenum.
- New-generation CWTS K2 steel contains aluminum (Al) and niobium (Nb) additions.

By obtaining very high-quality steels with codes D2, C2, and K2;

- three different punches for the manufacture of electric motors lamination rotor sheets from 0.50 mm non-oriented electrical steel (EN 10341), having Vickers microhardness of about 223 HV were manufactured (Figure 3), and

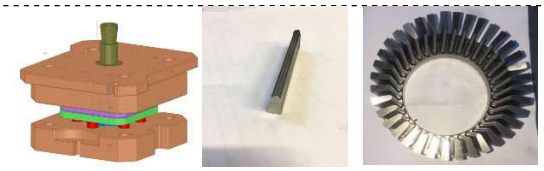

Figure 3. Die press, a single punch, and a set of 36 punches

- three different thread rolling die sets (fixed die; mm 25.2x52x105 and movable die; mm 25.2x52x90) for the manufacture of Ø4x50 mm screws were manufactured (Figures 4 and 5).

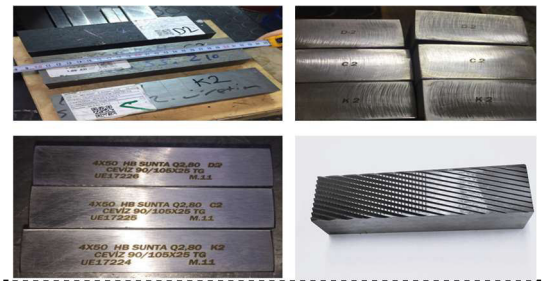

Figure 4. Raw and machined sets of thread-rolling dies

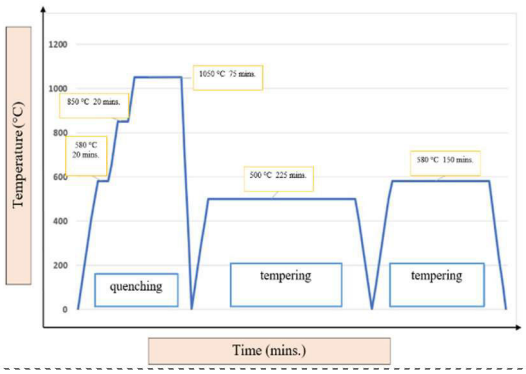

Figure 5. The heat treatment procedures applied

3. RESULTS

Upon performance, tests were carried out the number of reached products during each manufacture is shown in Table 2.

Table 2. Results of pieces manufactured by D2, C2 and K2 CWTS

	As punch material	As thread rolling die
D2 (1.2379)	112.500	983.800
C2	203.000	1.406.000
K2	224.000	1.861.100

FactSage® is a fully integrated thermochemical optimization and modeling information processing system that encompasses Iron-Steel databases with processing modules in materials science, corrosion, glass technology, ceramics, and other fields, particularly metals. It enables a detailed examination of phase formations as they relate to temperature (Figure 6).

A phase diagram was drawn and the phases formed were determined. The amounts of carbides at the tempering temperatures of the D2, C2, and K2 were calculated. Generally, various carbide combinations determine mechanical properties. Mainly M_7C_3 and $M_{23}C_6$ type carbides were taken as the basis.

The effective phase at tempering temperatures is M_7C_3 with 71% in traditional D2 steel, and $M_{23}C_6$ with 90.9% and 75.2% in new generation C2 and K2 steels, respectively. The ratio of chromium carbide (Cr_7C_3) in D2 steel is 54.8%, which is higher than the total of all other carbide formations. Fe_7C_3 is also formed in this steel, with a ratio of 18.6% in its group and 13.2% in the whole steel (Figure 7). Here, the weight and effect are formed by Chromium Carbide (77%), Iron Carbide (11%), and Vanadium Carbide (3%), respectively. Although the weight is in this group, 3 out of every 4 carbides formed in D2 steel (24.1%) are $M_{23}C_6$. The effect of molybdenum is seen here: They are triple carbide clusters formed by molybdenum with chromium (41%) and iron (35%), with a total ratio of 76%.

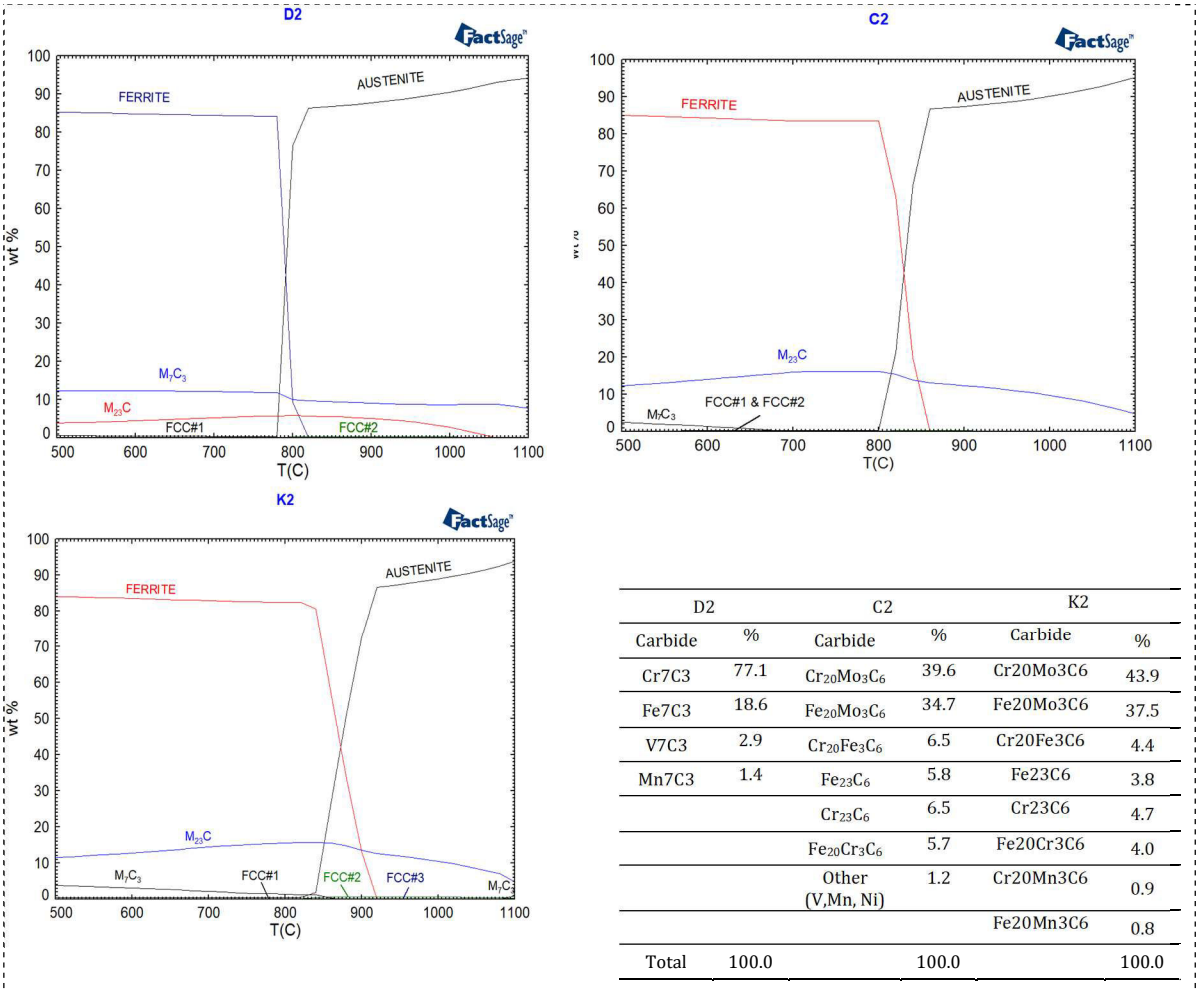

D2		C2		K2	
Carbide	%	Carbide	%	Carbide	%
Cr7C3	77.1	$Cr_{20}Mo_3C_6$	39.6	Cr20Mo3C6	43.9
Fe7C3	18.6	$Fe_{20}Mo_3C_6$	34.7	Fe20Mo3C6	37.5
V7C3	2.9	$Cr_{20}Fe_3C_6$	6.5	Cr20Fe3C6	4.4
Mn7C3	1.4	$Fe_{23}C_6$	5.8	Fe23C6	3.8
		$Cr_{23}C_6$	6.5	Cr23C6	4.7
		$Fe_{20}Cr_3C_6$	5.7	Fe20Cr3C6	4.0
		Other (V,Mn, Ni)	1.2	Cr20Mn3C6	0.9
				Fe20Mn3C6	0.8
Total	100.0		100.0		100.0

Figure 6. FactSage® thermodynamic software carbide phases and ratios of tested samples

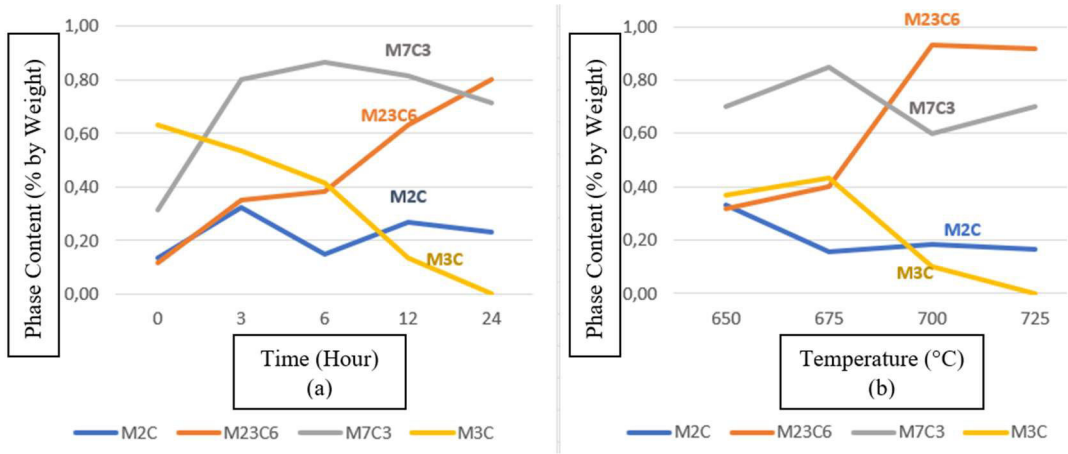

Figure 7. Changes in carbide ratios during tempering for (a) time and (b) temperature

In the New Generation CWTS, the active phases are phases formed by iron and chromium with molybdenum, 67.6% in C2 and 61.2% in K2. Here, the effect of molybdenum is seen clearly. The triple carbide clusters formed by molybdenum with chromium and iron are more than all other total carbides.

In all tool steels, a large number of carbides are formed, which make the steel unique with its microstructure, the amount of metallic elements it contains, and its morphology are different from each other. The most common carbide types encountered in the melting and casting stages in CWTS are M_2C, M_3C, M_7C_3, and $M_{23}C_6$ carbides. During heat treatments, these carbides depending on the heating rate, reached temperature, cooling rate, and time of holding at that temperature dissolved and transformed into their final form in the matrix, taking their place in the texture. During tempering, M_2C and M_3C decrease first, while M_7C_3 and $M_{23}C_6$ ratios increase. These transformations in carbides provide improvements in mechanical properties. Microcarbide islands improve performance [16].

4. CONCLUSIONS

The background of successful performance in steels is generally additional elements. Refractory metals which the world has been working on for a century, should not be overlooked. It is thought that the choice of using molybdenum, niobium, and aluminum in the new generation CWTS is not a coincidence.

Molybdenum, together with niobium, is an element that establishes microstructural control not only in tool steels but also in all alloy steels where superior performance is expected. These steels will become increasingly important in the production of lighter and more durable parts that will provide heavy-duty service conditions in vehicles, machines, and power plants.

The most critical stage is tempering, as it plays a key role in inducing microstructural changes in the carbides, which are essential to the manufacturing process. Successful results can be obtained to the extent that the coarsening of fine carbides can be prevented. The functionality of the ratios of the elements forming the chemical composition depends only on the quantity and quality of the carbide types to be formed, and this directly depends on the temperature and duration of tempering. Here, every few degrees and minutes that can change downward or upward are potential gains or untimely damage, i.e. a source of loss.

In all three steels studied, D2, C2, and K2, the primary elements are chromium, molybdenum, and vanadium, along with carbon, while manganese and silicon serve as supporting elements. In our K2 example, niobium should also be added to these. The knowledge that carbides can transform into each other provides us with valuable data. Since a 'knife-edge' decision that is of critical importance for the development of steel with factors affecting one may hurt another, a performance threshold that combines all positive features and optimizes them by knowing the relevant parameters better can be achieved in order not to 'break one side while doing another'.

Molybdenum and niobium will be the more important alloying elements for future steels. It is inevitable that other elements, especially Boron (B), will be added to them.

Acknowledgments

I would like to sincerely thank MATIL Material Testing and Innovation Laboratories Inc. for their invaluable laboratory facilities and equipment support throughout this study.

Conflicts of Interest

The authors declare no conflict of interest.

5. REFERENCES

[1] W. Callister and D. Rethwisch, Materials Science and Engineering, Wiley, USA 2018

[2] ASM Handbook, Nonferrous Alloys and Special-Purpose Materials, v2, ASM, USA, 1992

[3] F. Habashi, Handbook of Extractive Metallurgy, v.3, Wiley-VCH, Germany, 1997

[4] E. Dokumaci, *Production and Characterization of High Temp. Corrosion Resistant Materials*, [PhD. Thesis], Ege University, Türkey, 2012
https://thermic-edge.de/en/home/vacuum-products/refractory-metals/ (10.12.2024)
https://thermic-edge.de/wp-content/uploads/2021/04/Periodic-Table.jpg(10.12.2024)

[5] Hardy Mohrbacher, Property Optimization in As-Quenched Martensitic Steel by Molybdenum and Niobium Alloying, *MDPI Journal, Metals*, 8 (2018) 234, Sweden

[6] Irati Zurutuza Renom, *Exploitation of synergetic effect of Mo and Nb on high strength quenched and tempered boron steels*, [PhD. Thesis], Tecnun Universidad de Navarra, Spain, 2022

[7] J. G. Speer, Solubility and Prec. of Carbides Containing Nb and Mo in Low Alloy Steels, Proceedings of the 2. International Symposium on Mo and Nb Alloying Steels, V.2, Brasil, 2015

[8] C. Hojerslev, Tool steels, Riso National Laboratory, Denmark, 2001

[9] D. Viale, Optimizing Microstructure for High Toughness Cold-Work Tool Steels, Proceedings of the 6th International Tooling Conference, Karlstad, Sweden, 2002

[10] J. Lecomte-Beckers and J. T. Tchuindjang, Institut de Mécanique et Génie Civil, Matériaux Métalliques Spéciaux, Wiley Analytical Science, Liège Belgium, 2005

[11] N. Medvedeva, V. Aken and J. Medvedeva, Computational Materials Science, 96A, USA, 2015

[12] D. F. West, and N. Saunders, *Ternary Phase Diagrams in Materials Science*, Maney Publishing, UK, 2013

[13] D. Casellas, Fracture toughness of carbides in tool steels evaluated by nanoindentation, *Acta Materialia,* v. 55, Science Direct, Elsevier, Nederland, 2007

[14] R. Colas and G. E. Totten, Encyclopedia of Iron, Steel, and Their Alloys, v4, USA, 2016

[15] S. Depinoy, *Evolution microstructurale d'un acier 2.25 Cr 1 Mo au cours de l'austénitisation et du revenue*, [Ph.D Thesis], Ecole Nationale Sup´erieure des Mines de Paris. France, 2017

JST&M 8(2025), 43 – 53
DOI: 10.57131/jstm.2025.8.7

Original scientific paper

DUCTILITY CAPACITY STUDY OF LARGE-SCALE, BUCKLING-RESTRAINED BRACES IN STEEL STRUCTURES

Mohammad Amin Abdollahzadeh[1], Shima Shamekhi[2]

[1]Department of Mechanical Engineering, Faculty of Engineering, Yeditepe University, Istanbul, Türkey
[2]Department of Civil Engineering, Faculty of Engineering, Ozyegin University, Istanbul, Türkey

ABSTRACT

One of the new methods of anchoring steel structures is the use of large-scale buckling-restrained braces (BRBs) on the lateral system of this type of structure. This study investigates the behavior of BRBs and compares them with buckling braces. In this study, a two-dimensional frame with four stories and four spans was taken and analyzed in eight different ways, and each in the form of buckling and buckling-restrained braces. The results show that making the braces buckling-restrained has a positive effect on increasing ductility and energy dissipation.

Keywords: ductility capacity; steel structures; large-scale buckling-restrained braces

Corresponding Author: Mohammad Amin Abdollahzadeh
Department of Mechanical Engineering, Faculty of Engineering, Yeditepe University, Istanbul, Türkey
Tel.: +90 216 578 0498
E-mail address: mohammadamin.abdollahzadeh@yeditepe.edu.tr

1. INTRODUCTION

The building of metal structures as a symbol of progress and development began in the 1880s with commercial and residential use. The construction of commercial buildings was initially a response to demand from the business community, who wanted to live as close to each other and in the city center as possible. This led to great pressure on horizontal space in the central areas of cities. As metal structures usually have a striking appearance, they are also used by businesspeople as advertising media. On the other hand, the business world and tourism are interested in building high-rise hotels in city centers due to the high number of visitors and favorable economic returns. The rapid increase in the urban population and the lack of space have also had an impact on the architecture of residential buildings. The increase in land prices, the need to limit the horizontal expansion of cities, and the preservation of agricultural land are among the factors that have influenced the development and construction of metal structures.

The analysis and design of metal structures is considered one of the most important fields in civil engineering. Throughout history, earthquakes have always been considered one of the natural disasters that have caused the most material and spiritual losses in human societies. Until a few hundred years ago, this attention was limited to the fear of earthquakes and the attempt to avoid them. But as human societies have progressed, and especially as civil engineering has progressed, they have always looked for a solution to deal with them or to control the damage they cause in the best possible way. Today, engineering science has concluded that by understanding this phenomenon and its effects, as well as by researching and studying appropriate construction methods, recognizing new

materials and using new equipment, and studying the results of past earthquakes, solutions can be found to reduce the effects of earthquakes and the damage they cause in different regions [1].

A brief review of the damage caused to structures in past earthquakes has shown that steel structures are better and more economical than other structures due to the deformability of the materials and their ability to absorb energy. Therefore, the need to select devices to absorb lateral loads from wind and earthquakes so that the optimal shape with the fewest materials absorbs the most energy in the structure has been considered in advance to ensure optimal behavior and reduce damage to structural members.

With the emergence of a new form of braces, called large braces, in recent years, these braces are expected to have a different seismic behavior (in terms of stiffness, efficiency, and ductility) than previous braces due to their geometric shape [2]. In addition, the buckling of these braces improves the behavior of the structure in terms of stability and energy absorption capacity [3]. In contrast to conventional braces, the braces in these structures cover multiple floors and spans as one brace. Therefore, several bracing arrangements of a particular bracing shape (e.g., cross) are possible for each structure, and the results are compared in two cases of non-buckling (buckling-restrained) and normal (buckling) braces. The natural conditions of Turkey and the way buildings are constructed in this country make it necessary for the issue of protecting society from earthquakes to be taken seriously in every respect. With the advances in civil engineering sciences and the emphasis on the resistance of structures to lateral forces, the use of appropriate and reliable devices to cope with these forces becomes noticeable. A bracing system is usually used for this purpose.

Historically, bracing has been used for the lateral stability of most tall buildings in the world since the end of the 19th century [4]. Lateral resistance in braced frames is provided by diagonal members, which, together with the beams, form the web of a vertical truss system. In this system, the columns are the edges of the truss. Since the horizontal shear forces acting on the building are absorbed by the horizontal components of the axial tension or compression forces of the webs, the bracing system is very efficient and useful in absorbing lateral loads. The effectiveness of the bracing system in creating a laterally rigid structure and the use of minimal material have made it an economical form of construction for all types of buildings and at any height. Another advantage of diagonal bracing is that the beams are minimally affected by the lateral loads, so the design of the floor system can be designed and executed repeatedly in the floors, which makes economic sense [5]. However, the main weakness of this system is that the axial force in the vertical columns, which applies the lateral force, deviates from the uniform distribution in the ideal case. The main cause of this phenomenon is the importance of shear deformations in the behavior of the deep edge beams of the structure in this system and the invalidity of the assumption that the panels remain the same after bending; this leads to an increase in stress in the corner columns and a decrease in the middle columns of the wing and web panels [6].

Nowadays, the conventional convergent bracing system is the most common structural system for coping with seismic loads in steel structures, and its use is becoming increasingly popular due to its cost-effectiveness, simplicity of design, and ease of implementation. However, the damage caused by recent earthquakes such as the Loma Prieta, El Centro, and Kobe earthquakes to conventional convergent braced frames has raised concerns about the seismic performance of this system [7].

Conventional bracing undergoes large lateral deformations when subjected to lateral loads, whether from earthquakes or wind. When these deformations exceed a certain limit, they lead to structural and non-structural failure, and the safety and integrity of the

structure are jeopardized. The failure is aggravated by the P-Δ effect, and the destructive deformations increase. To cope with such deformations, different types of elements and systems are used in steel frames [8].

Diagonal elements in conventional concentric bracing systems increase the stiffness and strength of the structure, but do not result in significant energy absorption in the structure during an earthquake. Most conventional bracing with different cross-sections, consisting of a single steel beam, is designed to resist both compression and tension forces. Buckling of these members depends on the slenderness factor λ [9]. Poor behavior after buckling, differences in tensile and compressive capacities, degradation of stiffness and strength under cyclic loading, and fatigue at low cycles are among the most important and fundamental problems in the performance of compression elements. When buckling occurs, the lateral stiffness decreases sharply and the stability of the frame is reduced, resulting in severe damage to structural and non-structural components and, in some cases, structural collapse. Conventional braces, therefore, have limited ductility and asymmetric energy cycles [10].

To overcome the above problems, new types of braces were developed in Japan about 30 years ago to improve the conventional braces and develop braces with more ideal elastoplastic behavior; this idea was first proposed by Yoshino et al. [11]. These braces were widely used in Japan after the Kobe earthquake in 1995. These braces are designed to prevent buckling of the braces by a suitable mechanism and allow yielding of the steel by compression. It is important that yielding does not occur locally and that it is appropriately and evenly distributed over the entire component so that the energy absorbed during a reciprocating load, such as an earthquake, reaches its maximum. While conventionally stiffened frames exhibit irregular behavior and tend to concentrate large deformations in one or more stories (thus forming a soft story), BRBs are much more stable in this respect. This does not necessarily mean that the relative displacement is less, but that the inelastic response of the frame is more uniform than the entire height of the structure. In the United States, buckling-resistant braces were first used in 2000. After engineers in the United States recognized the value of buckling-resistant bracing, a group of researchers from the California Society of Structural Engineers, in collaboration with the American Steel Institute, published proposed criteria for buckling-resistant bracing in 1999. These criteria were incorporated, with minor changes, into the NEHRP Proposed Seismic Criteria in 2003 and the American Steel Code of Practice in 2005 [12].

In order to predict the performance of a structure under seismic forces, a nonlinear time history analysis of earthquake data with acceptable reliability is required to represent various seismic characteristics such as amplitude, frequency content, duration, and so on. Therefore, the aforementioned analysis is complex, time-consuming, and impractical in most cases. To overcome these limitations, it is necessary to develop an evaluation method that is relatively simple but represents the main characteristics of the earthquake and the structure. It also reflects the change in inertial forces and the distribution of deformations resulting from the nonlinear behavior. Nonlinear incremental static analysis is one of the methods that can effectively help achieve this goal for some structures. Nonlinear incremental static analysis provides useful information about the nonlinear behavior of buildings during earthquakes. However, it should be noted that the interpretation of the results of this analysis requires engineering judgment despite the variety of earthquakes, the uncertainty of material properties, and the difficulties in modeling.

In this work, two-dimensional frames were subjected to nonlinear incremental static analysis, and the ductility values as well as the additional strength factor and the ductility reduction factor were calculated for large-

scale and conventional non-buckling and large-scale and conventional buckling structures. All analyses were carried out using SAP2000 software.

2. MODELLING AND MATERIALS

The main functional principles of the operation of the BRB are to prevent the steel core from buckling, to allow the occurrence of compression yielding in it, and thus the possibility of absorbing energy in this component. This is achieved by encasing the entire length of the steel core in a sheathing filled with concrete or mortar. In this type of brace, the compressive load is carried by the steel core, and the concrete sheathing acts only as a lateral support to prevent buckling of the steel core, which causes the lateral distribution of internal pressure in the concrete sheathing. As a result, the buckling resistance of the core is greater than its yield strength, allowing the core to yield in both compression and tension, which significantly increases its energy absorption capacity. To prevent the axial compressive force of the steel core from being transferred to the concrete, this system gives the brace a high inelastic capacity, which absorbs more seismic energy and allows other components to remain within the elastic range. The difference in the behavior of conventional and buckling-resistant braces leads to different hysteresis behavior, which is shown in Figure 1. Different components of a BRB are depicted in Figure 2. As shown in Figure 3 in this study a total of eight two-dimensional 4-story frames are used which are braced with 4*4 X shape brace (covering four stories and four spans), 4*2 X shape brace (covering two stories and four spans), 2*2 X brace (covering two stories and two spans), K shape brace, diamond shape brace, V shape brace, 4*2 inverted V (∧)shape brace, and 1*2 ∧ shape brace, respectively. All these braces are designed and studied once as non-buckling and once as buckling states. The frames have 4 spans with a length of 6 meters and a height of 3.2 meters. The connection of the beam to the columns and the braces to the frame in these models is of the hinge type, and the supports are connected to the foundation in a fixed manner. The dead and live loads of the roof are 4kN/m^2 and 1.5kN/m^2, respectively, and the dead and live loads of the other floors are 4.7kN/m^2 and 2kN/m^2, in the given order. The mechanical properties of the steel material used in these analyses are listed in Table 1.

Table 1. Mechanical properties of materials used in models

Type	ρ	E	υ	σ_y (beams, columns)	σ_y (braces)
JIS-SN400	7830 kg/m^3	200 GPa	0.3	3500 kg/cm^2	2900 kg/cm^2

3. RESULTS AND DISCUSSIONS

Capacity curves obtained for these eight types of braces are shown in Figure 4. As it is observed, in all types of bracing, the area under the load-displacement curves is greater when non-buckling braces are used. Since the area under the curve represents the amount of energy dissipated by the structure, the greater the area under this curve, the greater the structure's ability to absorb and dissipate energy.

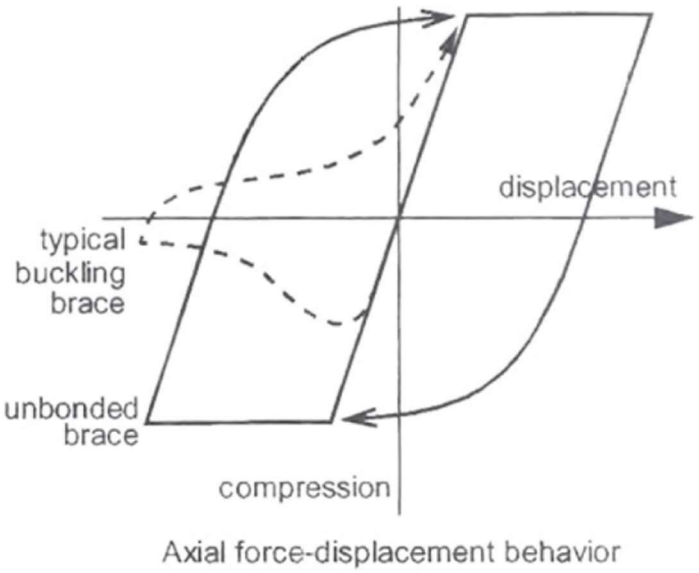

Figure 1. Comparison of load-displacement curves for BRBs and normal braces [3]

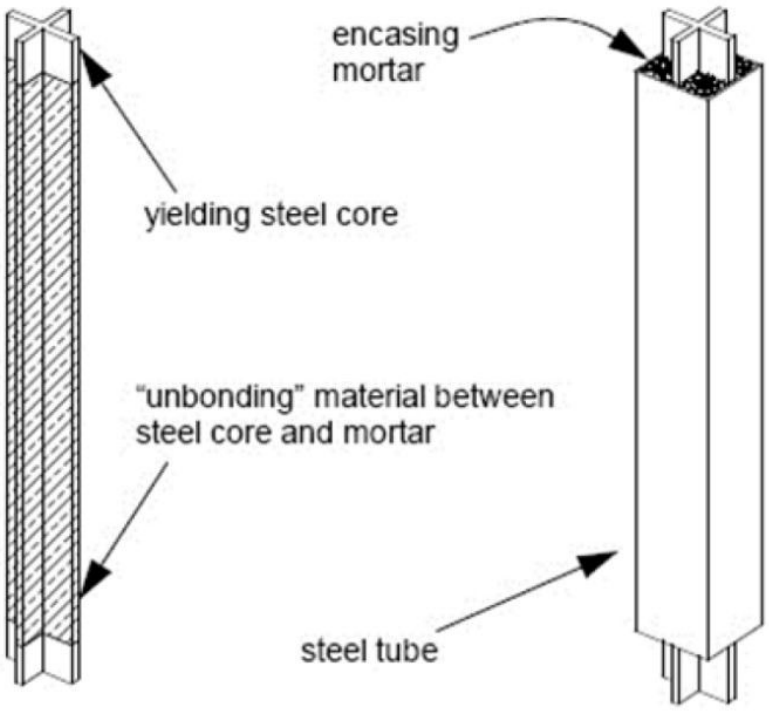

Figure 2. Different parts of the buckling restrained brace [3]

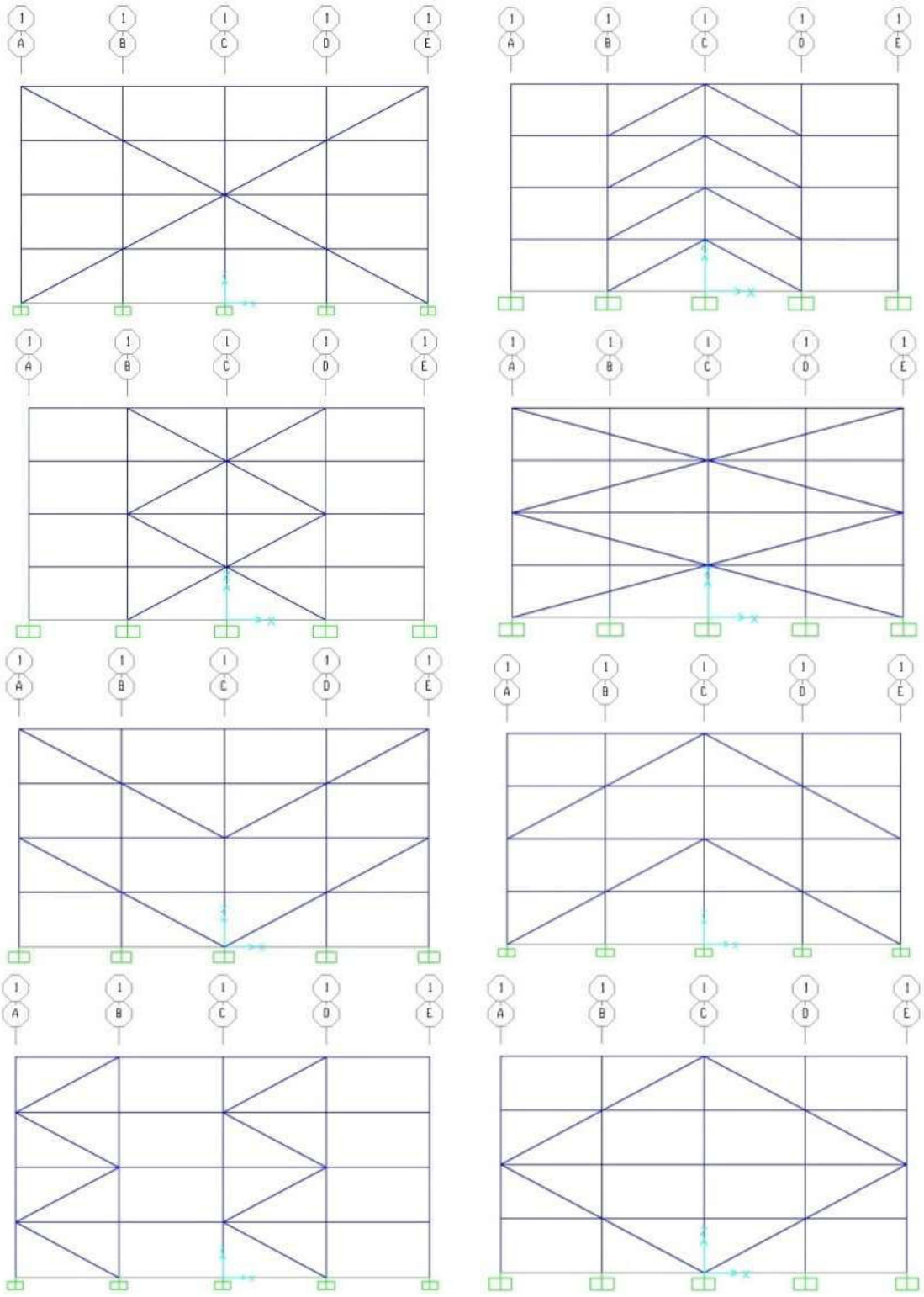

Figure 3. Eight different bracing models were used for analysis

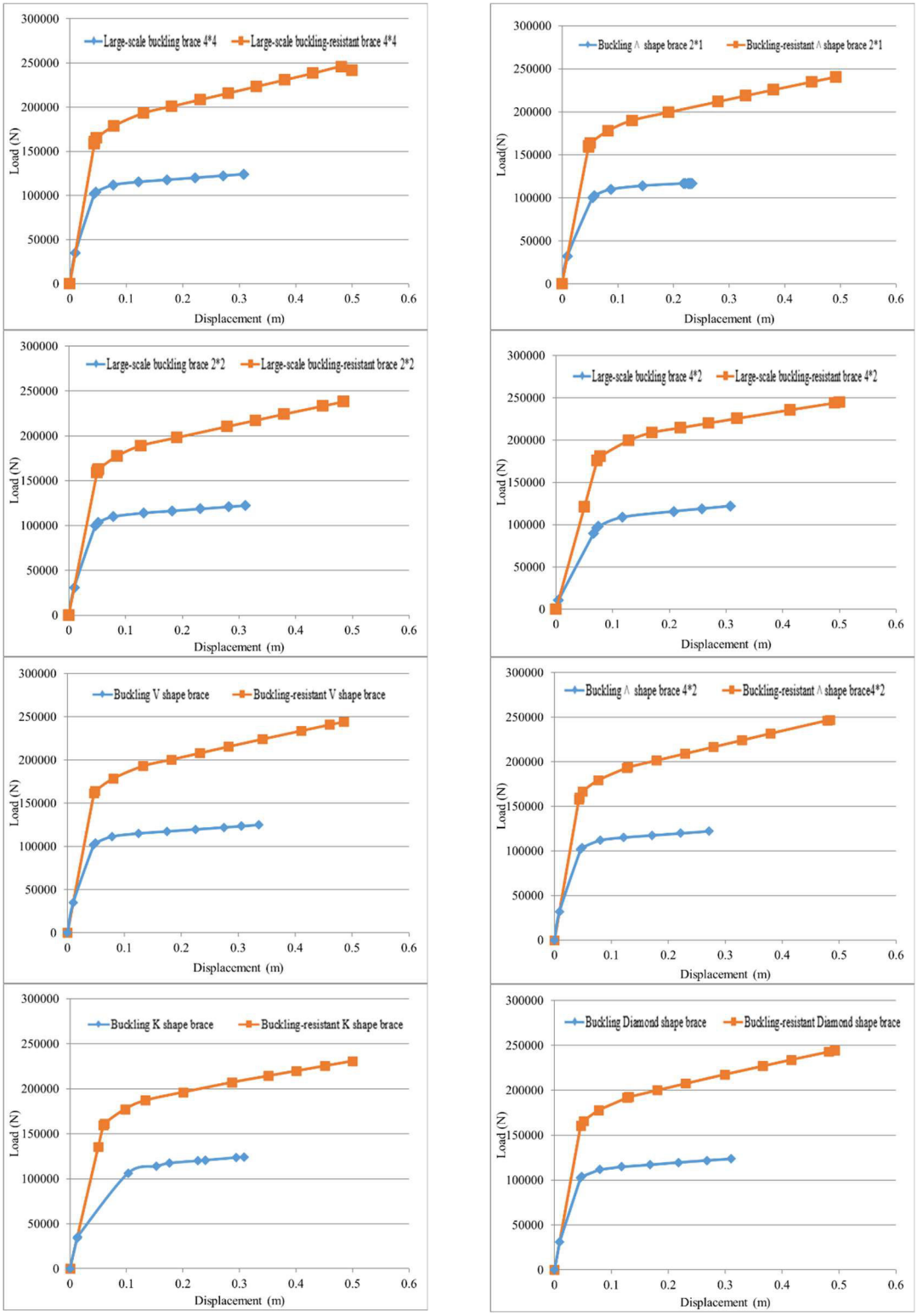

Figure 4. Load-displacement curve of different bracing models in buckling and non-buckling states

When a structure is subjected to large forces caused by an earthquake, it can dissipate the energy introduced by the earthquake to the extent of the area under the base-shear and

lateral displacement curve if it behaves elasto-plastically. The greater this energy dissipation, the lower the vibrations of the structure and the less the structure can react to the vibrations caused by the earthquake. In this section, the trapezoidal integral method was used to determine the area under the load-displacement curves.

Figure 5 shows that among the non-buckling braces, the 4*4 X-shaped, the 2*2 X-shaped, and the diamond-shaped braces dissipate the most energy, respectively. Whereas, among the buckling braces, the 4*2 V-shaped, the 4*4 X-shaped, and then the diamond-shaped braces have the highest energy dissipation in the given order.

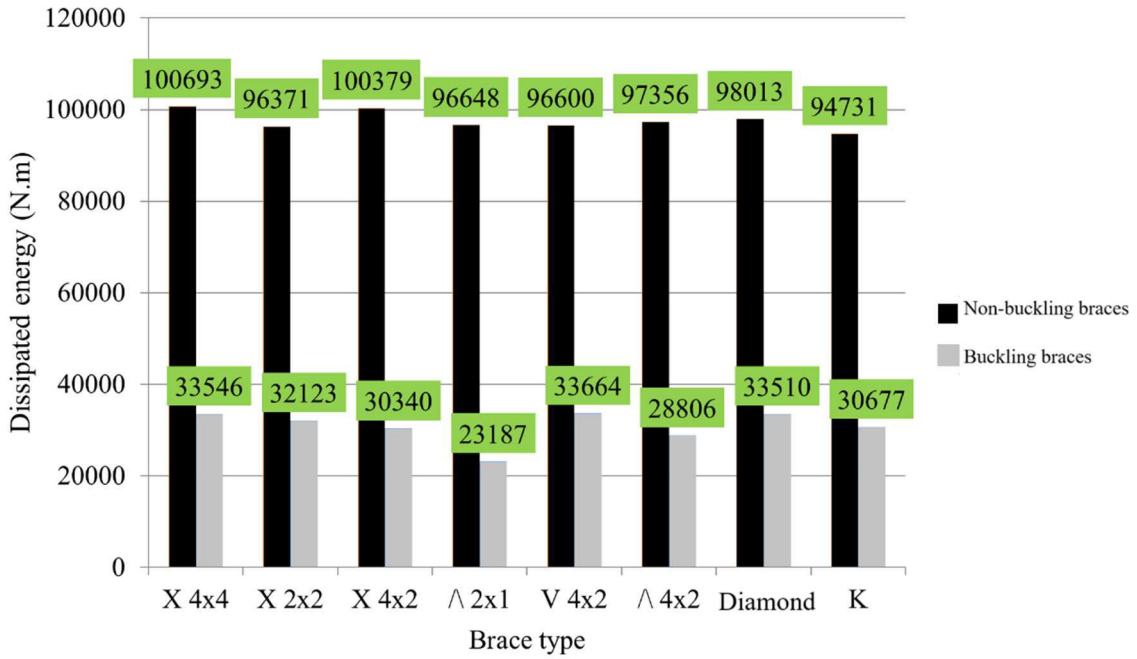

Figure 5. Dissipated energy magnitude of different bracing models in two buckling and non-buckling states

Ductile materials are materials that exhibit large strains while carrying a load. A ductile member must firstly be able to withstand sufficiently large non-reflexive deformations without significantly reducing its resistance, and secondly be able to absorb and dissipate a significant amount of seismic energy through stable behavior cycles. The ductility of flexural frames is defined as the ratio between the ultimate deformation of the frame end (Δu) and the displacement, such as the yield strength of the frame end (Δy), as:

$$\mu = \Delta u / \Delta y \quad (1)$$

Ductility of the frames is calculated using the above equation. The obtained results are illustrated in Figure 6. These results show that all non-buckling braces have a higher ductility than buckling braces. Among the non-buckling braces, the 4*2 ∧ brace has the highest ductility. Then follow the diamond and 4*4 X braces with some lower ductility. The 4*2 brace has the lowest ductility among these braces. Among the buckling braces, the 4*4 X, 4*2 V, and 2*2 X braces have the highest ductility, respectively, and the 2*1 ∧ brace has the lowest ductility.

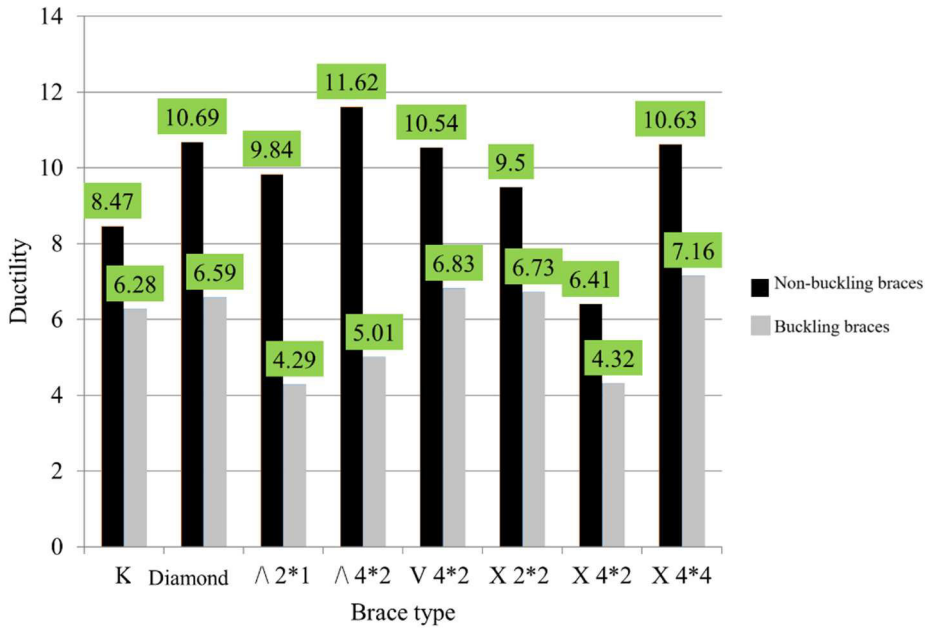

Figure 6. Ductility magnitude of different bracing models in two buckling and non-buckling states

In this study, the ductility reduction coefficient (Rμ) is also calculated using three common methods: Newmark-Hall [6], Krawinkler–Nassar [7], and Vidic [8], and the results are compared to each other. For a structure with a single degree of freedom, Newmark-Hall is calculated as follows:

$R_\mu=\sqrt{2\mu-1},\ T\le 0.5$ sec (2)
$R_\mu=\mu,\ T\ge 0.5$ sec (3)

where μ is ductility and T is the natural period of the structure. In the Krawinkler–Nassar relationship ductility reduction coefficient is calculated as:

$R_\mu=[c(\mu-1)+1]^{(1/c)}$ (4)
$c=(T^n/T^{n+1})+(b/T)$ (5)

where n is an exponent that adjusts the influence of period on the coefficient c. Here, c is an empirical coefficient obtained from regression analysis based on earthquake records, and b is another empirical parameter related to structural and seismic characteristics. Finally, the Vidic method proposes the following relations:

$R_\mu=(M-1)\times(T/T_0)+1$ if $T\le T_0$ (6)
$R_\mu=\mu$ if $T>T_0$ (7)

where M is a ductility-related parameter, often representing the ductility demand, which is the ratio of maximum to yield displacement. T_0 is the reference period, often used as a threshold to differentiate short-period and long-period behaviour. The $R\mu$ results obtained from these three approaches are compared in Figure 7. In design codes, the structures are designed in such a way that none of them exceeds the elastic stage. Otherwise, plastic hinges will form in them. As a result, the overall stiffness of the structure decreases, but it is still able to resist until the formation of hinges causes a mechanism, and the stiffness of the structure tends to zero. At this stage, when the ductility capacity has also reached its limit, the structure is destroyed.

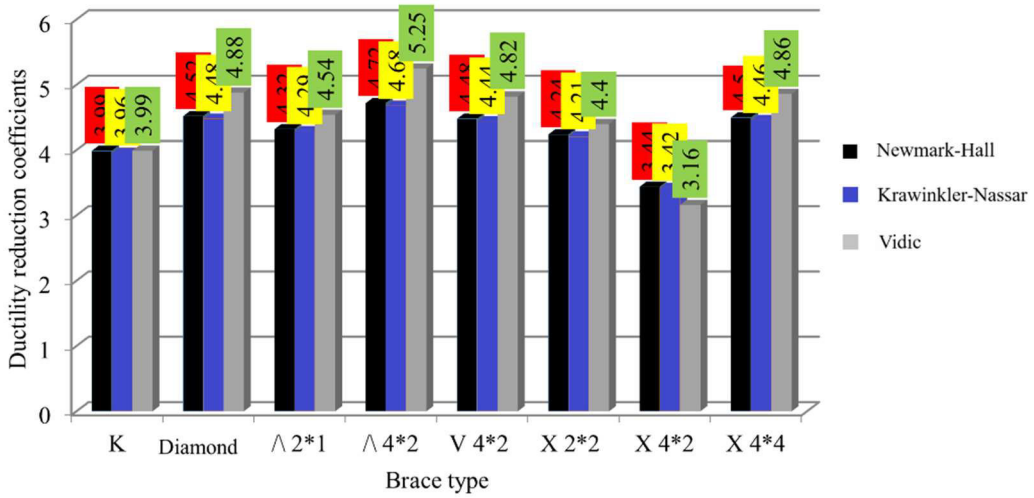

Figure 7. Ductility reduction coefficient values of different bracing models in non-buckling state using Newmark-Hall, Krawinkler-Nassar, and Vidic methods

During this process, the structures withstand additional resistance, which was not considered in the original design of the structure, and is referred to as additional resistance. This Increased resistance coefficient (Ω) is calculated as:

$$\Omega = V_y / V_s \quad (8)$$

where V_y is the force corresponding to the total yield strength of the structure, and V_s is the force corresponding to the formation of the first plastic hinge in the structure. Due to the proximity of the values of V_y and V_s, all values for the additional resistance coefficients are close to each other. The values of these coefficients for non-buckling braces are slightly larger than their values for buckling braces. Figure 8 indicates that the highest Ω value for non-buckling braces is for 4*4 X, followed by 4*2 ∧ and K braces, and the lowest value is for 4*2 V brace. Whereas for buckling braces, the highest value of Ω is for 4*2 ∧, K, and 2*2 X braces respectively, and the lowest value is for 4*2 V brace.

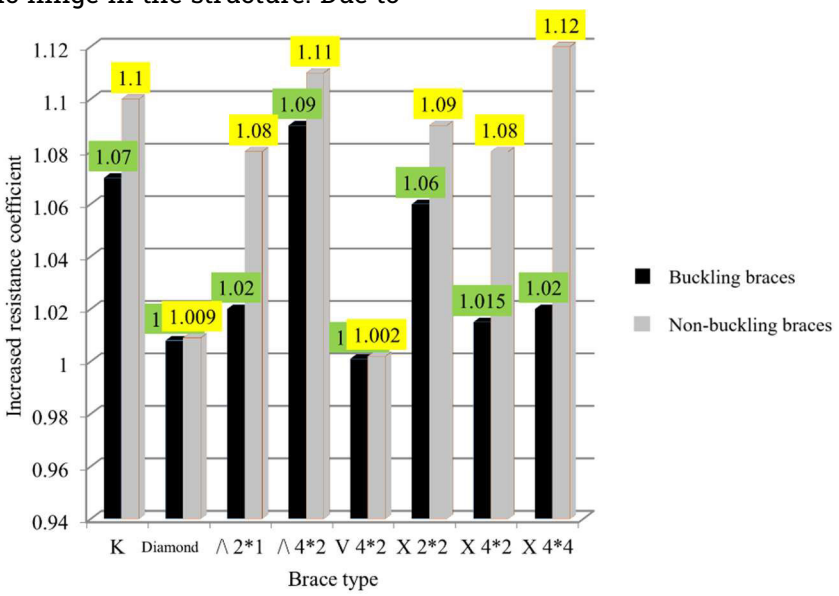

Figure 8. Increased resistance coefficient values of different bracing models in two buckling and non-buckling states

4. CONCLUSION

Due to the importance of load distribution and understanding the real behavior of a braced system under lateral earthquake forces in structures, the effect of buckling in bracing systems is investigated in this paper and compared in two buckling-resistant and buckling-unrestrained conditions for different models. Non-buckling braces have high energy dissipation, ductility, and a high behavior coefficient compared to buckling braces. The scaling of the brace has a favorable effect on the ductility and energy absorption of the structure. Among the non-buckling braces, X and diamond braces exhibit the highest energy dissipation. Among the buckling braces, X, V, and diamond braces have the highest energy dissipation. The ∧ , V, and diamond braces have the highest ductility of the non-buckling braces. The highest ductility among the buckling braces is shown by the 4*4 X- and V-shaped braces.

Conflicts of Interest

The authors declare no conflict of interest.

5. REFERENCES

[1] S. Shamekhi, A. Ansal, A. Kurtuluş, A Comparison Study Between 1D and 2D Site Response Analyses Based on Observed Earthquake Acceleration Records, In: 5th International Conference on New Developments in Soil Mechanics and Geotechnical Engineering. ZM 2022. Lecture Notes in Civil Engineering, 305, Springer, Cham. 2023 https://doi.org/10.1007/978-3-031-20172-1_38

[2] D. Vafaei, R. Eskandari, Seismic response of mega buckling-restrained braces subjected to fling-step and forward-directivity near-fault ground motions. *The structural design of Tall and Special Buildings*, 24 (2015) 9, pp. 672-686. https://doi.org/10.1002/tal.1205

[3] American Institute of Steel Construction, Seismic provisions for structural steel buildings (No. 2). American Institute of Steel Construction, 2002. https://doi.org/10.62913/engj.v44i1.900

[4] J. Bai, J. Zhang, S. Jin, K. Du, Y.H. Wang, A multi-modal-analysis-based simplified seismic design method for high-rise frame-steel plate shear wall dual structures, *Journal of Constructional Steel Research*, 177 (2021), 106484 https://doi.org/10.1016/j.jcsr.2020.106484

[5] M. A. Abdollahzadeh, M. Y. Belur, M. F. Basoglu, A. Kefal, Shape sensing of beam-like structures using the robust iFEM-iQS4 inverse shell element, *IEEE Transactions on Instrumentation and Measurement*, 72 (2023), pp. 1 - 9 https://doi.org/10.1109/TIM.2023.3309367

[6] J. Kim, H. Choi, Response modification factors of chevron-braced frames, *Engineering structures*, 27 (2005) 2, pp. 285 – 300 https://doi.org/10.1016/j.engstruct.2004.10.009

[7] N. Lam, J. Wilson, G. Hutchinson, The ductility reduction factor in the seismic design of buildings, *Earthquake engineering & structural dynamics*, 27 (1998) 7, pp. 749 – 769 https://doi.org/10.1002/(SICI)1096-9845

[8] A. Abdollahi, M. Poursha, K. Abedi, Seismic response modification factors of single-layer diamatic dome structures, *Engineering Structures*, 310 (2024), 118091 https://doi.org/10.1016/j.engstruct.2024.118091

[9] M. Naghavi, M. Malekinejad, A Study of the Behaviour of Steel Moment Frame with Buckling Restrained Bracing, *Soil Structure Interaction Journal*, 3 (2018) 1, pp. 64 - 70.

[10] Y. J. Yua, K. C. Tsaib, C. H. Li, Y. T. Weng, C. Y. Tsai, Analytical Simulations for Shaking Table Tests of a Full Scale Buckling Restrained Braced Frame, *Procedia Engineering* 14 (2011), pp. 2941–2948 https://doi.org/10.1016/j.proeng.2011.07.370

[11] T. Yoshino, Y. Karino, Experimental study on shear wall with braces: Part 2. In: Summaries of technical papers of annual meeting. Architectural Institute of Japan, Structural Engineering Section, 1971, pp. 403 - 404

[12] J. O. Malley, The 2005 AISC seismic provisions for structural steel buildings. *Engineering Journal*, 44 (2007) 1, pp. 3 – 14 https://doi.org/10.62913/engj.v44i1.900

JST&M 8(2025), 54 – 60
DOI: 10.57131/jstm.2025.8.8

Professional paper

INFLUENCE OF THE RATIO OF CALCIUM OXIDE AND SILICA ON MINERALOGICAL AND PHASE CHANGES OF SINTER FROM LIMONITE ORE

Amel Zahirović, Amira Pašalić

University of Zenica, Institute "Kemal Kapetanović" Zenica

ABSTRACT

Improving the quality of iron ore sintering and adding specific components has positive effects on blast furnace productivity. Optimizing basicity in the blast furnace charge is one way to improve all indices of production processes. Adjusting basicity aims to achieve the formation of new phase compounds that are favourable for the metallurgical and mineralogical sinter properties. The chemical analyses are insufficient for controlling the phase transition of multicomponent systems, as it is necessary to know the structure of all constituents. For that reason, X-ray diffraction is used for identifying minerals in sinter. Also, the physico-mechanical properties of sinter are investigated. Based on experimental results, the optimal basicity of limonite ore from mine "Omarska" Prijedor is determined.

Keywords: basicity, sinter, calcium oxide, limonite, phase composition, XRD

Corresponding Author:
Amel Zahirović,
Institute "Kemal Kapetanović", Zenica University
Travnička cesta 2, Zenica, B&H
Tel.: +387 32 247 999
E-mail address: amel.zahirovic@unze.ba

1. INTRODUCTION

For each metallurgical process of extracting metal from ore, to make metallurgical processing possible and economical, certain conditions are set both in terms of chemical composition and in terms of metallurgical and mineralogical characteristics. Small ores, concentrates, and other small raw materials cannot be directly melted in blast furnaces but must be enlarged previously, and the most common way is sintered.

The processes of ore are thermal and take place at temperatures beginning with smelting, which enables the interconnection of mineral grains. At such high temperatures, there are chemical, structural, and mineralogical changes that improve the metallurgical characteristics of the resulting product. To achieve desired phase transformations during the sintering process, it is necessary to add specific chemical compounds during preparation, with $CaCO_3$ being one of the preferred additives. To effectively monitor phase transformations within a multicomponent system, the X-ray diffraction method proved to be the best. This method is based on the fact that any phase or component creates its characteristic X-ray signature, which depends on the specific unit cell and atomic arrangement.

2. PRODUCTION OF SINTER AT A SEMI-INDUSTRIAL PLANT

As part of the planned testing and experimentation, the Department of Ore and Iron at the 'Kemal Kapetanović' Institute of the University of Zenica conducted six experiments using different basicity levels. Sinter production was carried out using a discontinuous-type pilot plant facility with a 70

Figure 1. The semi-industrial plant with a capacity of 70 kg

Table 1. The mark of sinter mix planned basicity

Mark sintered mixtures	M1	M2	M3	M4	M5	M6
Planned basicity	0.0	0.5	1.2	1.5	2.0	2.5

kg capacity (Figure 1). The facility is designed for producing various types of sinter [5]. The mark of the sinter mix with planned basicity is shown in Table 1. Sinter was produced at the Institute. The raw materials used in the experiment are: "Omarska" limonite ore, limestone from the Grapska-Doboj site, and coke from Arcelor Mittal Zenica. All components of the sinter mixture are prepared to the extent required by the technological conditions for the production of the sinter. The produced sinter was created from a sinter mixture according to the percentage of individual components given in Table 2.

After sintering, all samples were cooled in air, and then 20 mm fractions were separated, from which samples for the XRD method were taken by quartering. The samples were tested on a Shimadzu XRD 6000 diffractometer. All samples of the obtained sinter were chemically analyzed with the components given in Table 3.

Table 2. Composition of sintered mixture

Mark of the sample	The composition of the sintered mixture, %					Basicity: CaO/SiO_2
	Iron ore Limonite	Limestone	Coke	Return sinter	Moisture	
M1	66.57	0.00	6.06	19.96	7.41	0.0004
M2	59.80	6.75	6.06	19.97	742	0.49
M3	53.32	13.86	6.12	20.16	6.54	1.20
M4	50.74	16.45	6.11	20.16	6.54	1.49
M5	47.10	20.20	6.13	20.19	6.38	2.00
M6	43.97	23.52	6.15	20.25	6.11	2.48

Table 3. Results of sinter chemical analysis

Mark of the sample	The components, %									
	Fe	FeO	Fe_2O_3	SiO_2	MgO	MnO	CaO	Al_2O_3	S	CaO/ SiO_2
A1	54.23	21.10	61.54	11.42	1.93	1.83	0.005	1.92	0.006	0.0004
A2	52.11	17.63	60.48	9.58	1.82	1.94	4.69	1.68	0.007	0.49
A3	50.10	13.92	59.07	7.86	1.62	2.44	9.43	2.16	0.010	1.20
A4	49.62	14.29	56.13	8.49	1.91	1.99	12.65	1.96	0.018	1.49
A5	47.16	10.16	58.42	8.21	1.91	1.93	17.24	1.89	0.019	2.10
A6	46.29	8.66	56.21	11.28	1.84	1.86	27.97	1.84	0.029	2.48

3. PROPERTIES OF PRODUCED SINTERS

3.1 Physical and mechanical properties of sinter

As part of the examination of the physical and mechanical properties of the sinter, a granulometric analysis was conducted using sieves with openings of 40 mm, 20 mm, 16 mm, 10 mm, and 6.3 mm. Additionally, the strength index and abrasion index were examined. Furthermore, the porosity and density of the sinter, as well as the melting and softening temperatures, were tested on the examined samples.

3.1.1 Granulometric composition for sinter

The diagram in Figure 2 shows the granulometric composition of the sinter depending on basicity. The data illustrate a direct relationship between basicity and particle size composition. As the basicity increases, the quality of the sinter decreases; that is, with a lower basicity, the granulomer composition of the sinter is better because the permeability of gases in the iron production process will be better [5-7].

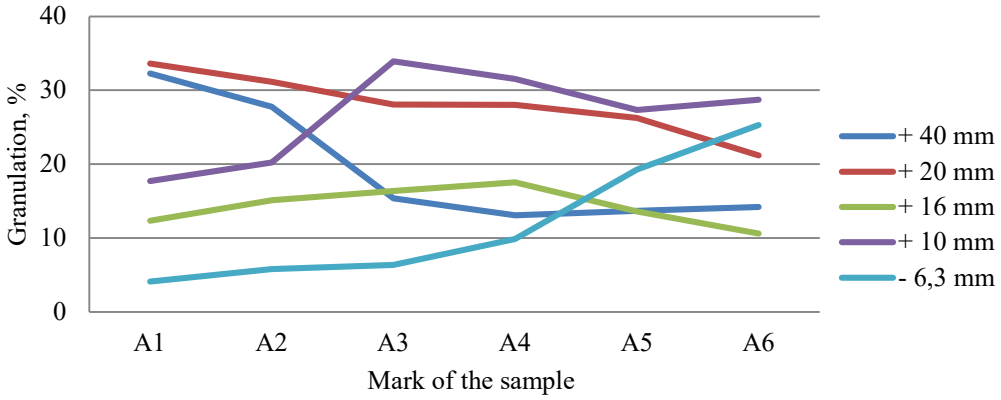

Figure 2. Particle size distribution of sinter

3.1.2 Granularity and strength of sinter

The sinter strength test is performed according to ISO TC (102)-SC3 in a drum Ø1000 mm, length 500 mm with two partitions. After rotation of 200 revolutions per minute for four minutes, sieving is carried out on sieves of 6.3 and 0.5 mm. The strength of the sinter is shown through the strength index T_i and the abrasion index A_i.

$$T_i = \frac{m_1}{m_1 + m_2 + m_3} \times 100 \quad (1)$$

$$A_i = \frac{m_3}{m_1 + m_2 + m_3} \times 100 \quad (2)$$

Where is:

T_i – strength index

A_i – abrasion index

m_1 – sample mass +6.3 mm, g
m2 – sample mass -6.3+0.5 mm, g
m3 – sample mass -0.5 mm, g
The strength index (T_i) of sinter A1 is 67.45% at a basicity of 1.2, while the strength index of sinter A3 is 74.25%. With increasing basicity, the strength index continuously decreases, and the lowest value is for sinter A6, which is 56.25% (Figure 3). The abrasion index (A_i) increased continuously with increasing basicity, and for sinter marked A5, it is around 10.93%. The best value for this parameter is around 5%.

3.1.3 The density and porosity
The results presented in Figure 4 indicate that changing the basicity has little effect on the sinter density, with only a slight change reflected in an increase in porosity ranging from 1-6%.

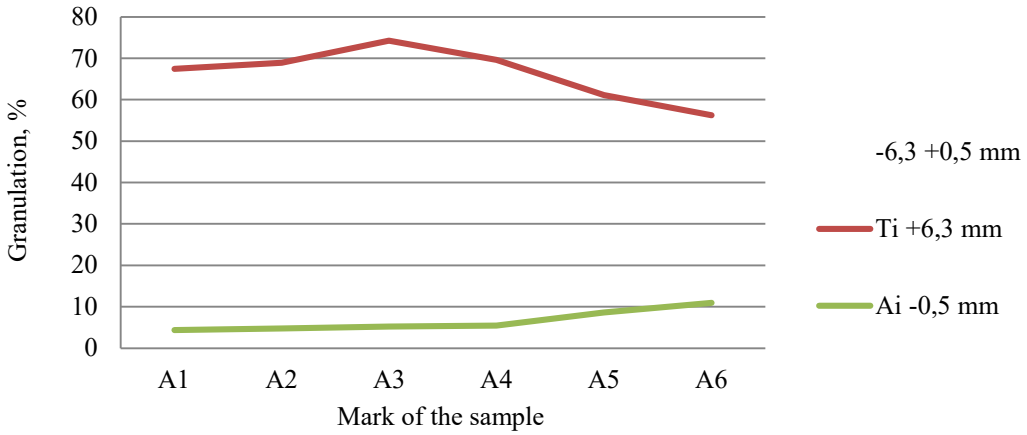

Figure 3. Graphic representation of the strength and abrasion index of sinter

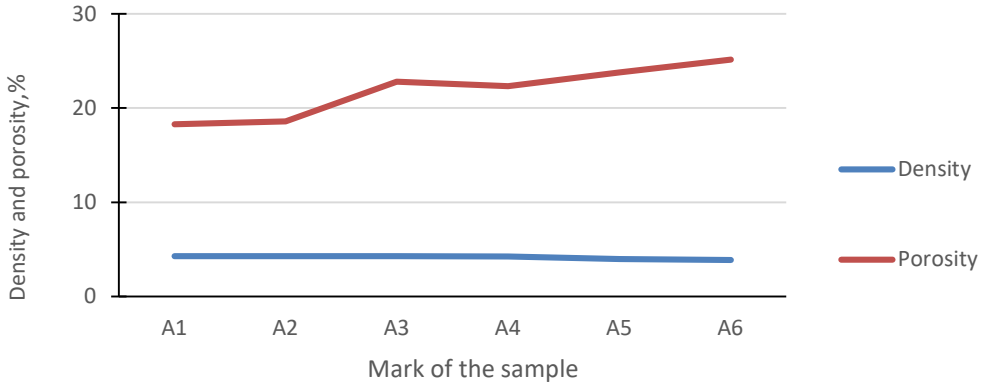

Figure 4. Graphic representation of the density and porosity of the sinter

3.1.4. Metallurgical properties of sinter
For sinter, a high melting point and a narrow softening interval are essential properties. The softening and melting temperatures are influenced by several factors, among which the most significant are mineral composition, porosity, ore type, and ore granulation. Observing the test samples of sinter, it can be concluded that the softening interval for basic sinter (A3-A6) is small, ranging from 20°C to 60°C, while for samples (A1-A2), it can extend up to 160°C.

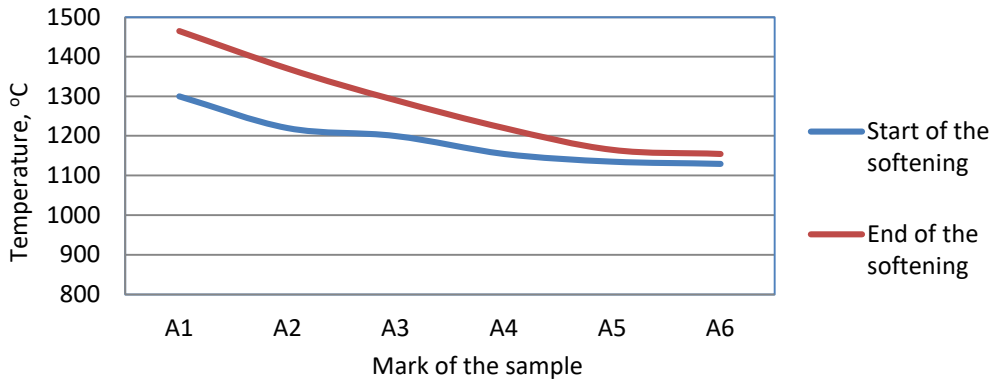

Figure 5. Graphic representation of the softening and melting temperatures of sinter

4. MONITORING THE PHASE TRANSITIONS USING X-RAY DIFFRACTION

Figures 6 to 11 show X-ray images of the obtained sinter. In Figure 6, it can be observed that magnetite predominates and plays a leading role in the mineral composition of the sinter, followed by fayalite and quartz. This is because no limestone was added during the sintering process, and instead, the natural basicity of the raw material was utilized. The results shown in Figures 7 and 8 indicate the formation of new compounds, such as hematite and SCAF (calcium silicate), as well as dicalcium silicate [4].

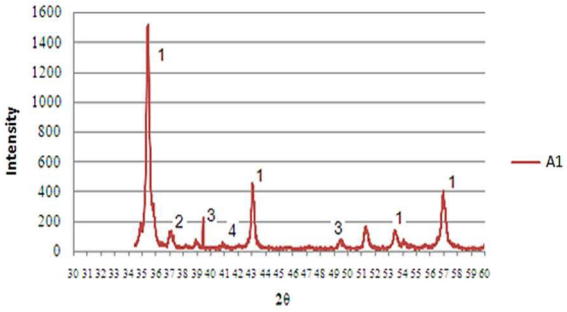

Figure 6. X-ray of sinter mark A1; 1-Magnetite, 2-Fayalite, 3-Quartz, 4-Anortite

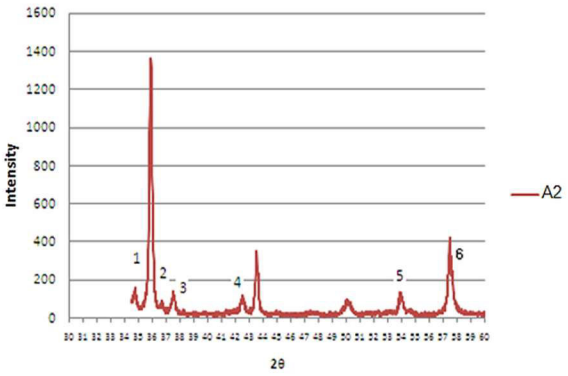

Figure 7. X-ray of sinter mark A2; 1–Magnetite, 2–SCAF, 3-Fayalite, 4-Anorthite, 5- Hematite, 6-Calcite

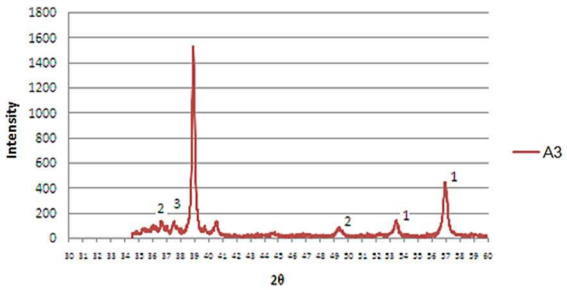

Figure 8. X-ray of sinter mark A3; 1-Magnetite, 2-Dicalcium silicate, 3-Anortite

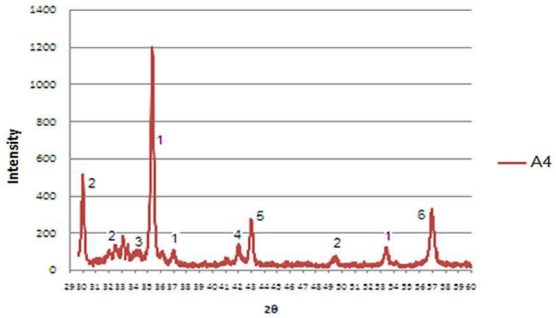

Figure 9. X-ray of the sinter mark A4; 1-Magnetite, 2-Dicalcium silicate, 3-SCAF, 4-Wustite, 5-Perclase, 6-Calcite

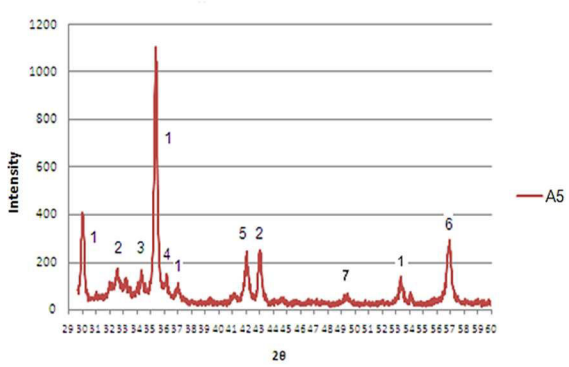

Figure 10. X-ray of sinter mark A5; 1-Magnetite, 2-Dicalcium silicate, 3-SCAF, 4-Wustite, 5-Periclase, 6-Calcite

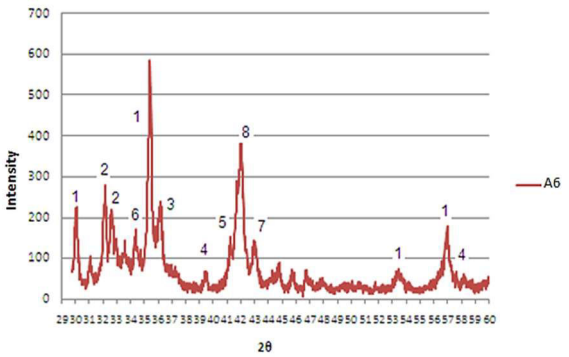

Figure 11. X-ray of the sinter mark A6; 1-Magnetite, 2-Dicalcium silicate, 3-SCAF, 4-Calcite, 5-Hematite, 6-Anortite, 7-Periclase, 8-Wustite

In Figure 9, a new phase can be noted as a result of the addition of limestone or increasing basicity through periclase and FeO-wustite, which was created after the completion of the magnetite reduction.

The results shown in Figures 10 and 11 demonstrate that an increase in basicity leads to a change in the mineral composition of the sinter. Fayalite essentially binds into other compounds or disappears. This happens because all the calcium ferrite is converted into calcium silicate [4].

5. CONCLUSIONS

Based on the results of the tests, it can be concluded that basicity significantly modifies the properties of sinter. It can be observed that the granulometric composition quality deteriorates with increasing basicity. The abrasion index and strength index are acceptable only for sinters labeled A3 and A4. An increase in basicity results in a moderate increase in porosity, while the sinter density remains unchanged. It can be concluded that changes in basicity have a significant impact on the onset and end of sinter softening. Specifically, the sintering softening interval decreases with increasing basicity. Based on the experiments and the results obtained from the research, it is concluded that the optimal basicity for the used raw materials (Limonite from Prijedor, coke from Zenica, and Dolomite from Doboj) is 1.2, marked as A3. Increasing or decreasing the basicity from the optimal value would lead to a deterioration in the properties of the sinter and could disrupt the potential iron production process.

Conflicts of Interest

The authors declare no conflict of interest.

6. REFERENCE

[1] T. Umadevi and others, Influence of iron ore fines size on microstructure, productivity and quality of iron ore sinter, *ISIJ International*, 51 (2001) 6, pp. 922–929

[2] A. Zahirović, Exploring the impact of basicity sinter mixture on mineralogical and metallurgical characteristics of sinter produced from limonite ore, [Master Thesis], University of Zenica, Faculty of Metallurgy and Materials, Zenica, 2013

[3] Huang X, LV X and Xue Z, Interpretation on Iron ore granulation process based on particle size analysis, *ISIJ International,* 56, (2016), pp. 1964-1972

[4] V. Suresh, C. Sarkar, A. Vishnuvardhan, M. K. Sharma, S. Chakraborty, Modification of wet granulation process during Iron ore sintering, XVIII Mineral Processing Technology 2019, Hyderabad

[5] V. Suresh, C. Sarkar, M. K. Sharma, and S. Chakraborty, "Study of Iron Ore size fraction on Sinter structure "Vizag Steel Quest 2019, pp.79-87, RINL, Visakhapatnam, India 2019.

[6] Deqing Zhu, Dingzheng Wang, Jian PAN, Zhengqi Guo and Congcong YANG, Utilization of Hydrated Lime as Binder and Fluxing Agent for the Production of High Basicity Magnesium Fluxed Pellets, *ISIJ International*, 62 (2022) 4, pp. 632–641

[7] V. Suresh, Mahesh Kumar Sharma, R. Bhaktavastala Rao, U. Parui, Optimisation of Slag chemistry to produce low Sulphur Hot metal in Blast furnace, 2nd International Conference on Advances in Minerals, Metals, Materials, Manufacturing and Modeling (ICAM5 2023) 22nd-23nd September 2023

[8] Amit Kumar Singh, Biswajit Mishra, and Om Prakash Sinha, Reduction Kinetics of Fluxed Iron Ore Pellets Made of Coarse Iron Ore Particles, *Steel Research International*, March 2024

[9] Jun Gi Seo, Jae Min Song, Do Yeon Lee, Han Jung Kwon, Effect of Al_2O_3 Content and Particle Size of Iron Ore on the Assimilation Characteristics of Sintered Ore, *Korean Journal of Metals and Materials,* 62(2004)9:696-704

JST&M 8(2025), 61 – 66
DOI: 10.57131/jstm.2025.8.9

Case study

EDUCATING FOR SUSTAINABLE PLASTIC MANAGEMENT IN A CIRCULAR AND CLIMATE-NEUTRAL ECONOMY

Katrin Školnik Škrabe[1], Anja Bubik[1], Špela Dermol[2], Santiago Ferrándiz[3], Dana Perniu[4], Elena Cristina Rada[5], Anca Draghici[6]

[1]Faculty of Environmental Protection, Velenje, Slovenia,
[2]Dermol svetovanje d.o.o., Šmartno pri Litiji, Slovenia,
[3]Department of Mechanical and Materials Engineering, Valencia Polytechnic University, Spain,
[4]Faculty of Product Design and Environment, Transylvania University of Brasov, Romania,
[5]Department of Theoretical and Applied Sciences, University of Insubria, Varese, Italy,
[6]Faculty of Management in Production and Transportation, Politehnica University Timisoara, Romania

ABSTRACT

Plastic has become indispensable since its introduction in the late 1800s, valued for its flexibility, durability, and affordability. Global plastic production has grown exponentially, reaching 400.3 million metric tons in 2022, despite a temporary decline in early 2020 due to the Covid-19 pandemic. However, only 9% of all plastics ever produced have been recycled, with 60% accumulating in landfills or the environment, underscoring an urgent need for sustainable solutions to manage plastic waste.

To address this challenge, the Erasmus+ project EDU4PlasticCircular aims to bridge the gap in sustainable development education related to plastics. Through collaboration with six organizations across four countries, the initiative is developing a comprehensive training program targeting higher education staff, students, and industry professionals. Employing innovative methodologies and an open-access online platform, the program emphasizes the transition to a circular and climate-neutral economy with a focus on plastics. This paper outlines the project's objectives, methodologies, and anticipated outcomes, including equipping learners with the skills needed to advance sustainable practices. By fostering a deeper understanding of the circular economy, the initiative aims to promote sustainable practices and raise awareness about the critical issues surrounding plastics.

Keywords: plastics, plastic waste, circular and neutral economy, training programme, green skills/competences

Corresponding Author:
Anja Bubik
Faculty of Environmental Protection
Trg mladosti 7, 3320 Velenje, Slovenia
Tel.: +38638986424; fax: /
E-mail address: anja.bubik@fvo.si

1. INTRODUCTION

Plastic has become an indispensable material across various economic sectors and daily life, including construction, transportation, renewable energy, packaging, healthcare, clothing, and sports [1]. In 2022, global plastic production reached 400.3 million metric tons (Mt) [2]. However, an estimated 60% of all plastics produced have ended up in landfills or dispersed in the environment, while only 10% have been recycled. Approximately 30% of all plastics

ever produced are still in use [2,3]. This has led to plastic pollution emerging as a critical global environmental issue, largely driven by the widespread use of single-use plastics [4]. These products are typically designed for short lifespans and are often discarded within a year of production [4,5]. Single-use plastics, particularly plastic packaging, are a major concern. Globally, only 14% of plastic packaging is collected for recycling, and of that, just 5% retains its material value for reuse. The leakage of plastics into the environment (Figure 1), particularly into marine ecosystems, is a significant problem [6]. Plastic production not only harms the environment but also plays a significant role in driving climate change. In the European Union, plastic manufacturing generates approximately 13.4 million tonnes of CO_2 emissions annually, accounting for roughly 20% of the total emissions from the EU's chemicals industry [7,8].

Figure 1. Plastic litter on the Savinja riverbanks, Slovenia (Faculty of Environmental Protection)

To address this challenge, a shift towards a circular economy is being advocated, aiming to minimize plastic waste and environmental harm by considering every stage of the value chain, from product design to disposal. This approach promotes a sustainable, waste-reducing system and aligns with the European Green Deal, launched in December 2019 [9], which seeks to make the EU climate-neutral by 2050. The European Green Deal supports the transformation to a fair and competitive economy by integrating policies across various sectors, an approach endorsed by the European Council to tackle climate and environmental challenges [4,10].

Today, there is an urgent need to address this problem at the educational level as well. Raising awareness and integrating environmental education are important steps toward achieving the EU's Green Goals. Projects targeting various learners, including those in higher education institutions (HEIs), play a significant role in this effort and are important for today's society.

2. ABOUT THE EDU4PLASTICIRCULAR PROJECT

EDU4PlastiCircular - Education for Plastic in a Circular and Climate Neutral Economy - Preventing Waste Ending Up in the Environment (EDU4PlastiCircular) [11] is a

pioneering Erasmus+ initiative that aims to transform attitudes and behaviours toward plastic use through education. Bringing together six partners from four countries, this project is a significant milestone in addressing global plastic waste and its impact on achieving a circular and climate-neutral economy. By providing target groups across the EU with essential knowledge and skills, EDU4PlastiCircular is dedicated to advancing circular economy principles and fostering eco-responsible citizenship.

The lead partner of the project is Politehnica University Timisoara (Romania), with the other partners, including Valencia Polytechnic University (Spain), Transylvania University of Brasov (Romania), University of Insubria (Italy), Dermol Svetovanje d.o.o. (Slovenia), and the Faculty of Environmental Protection (Slovenia).

Figure 2. Logo of the EDU4PlastiCircular project

The project (Figure 2) aims to enhance green skills among educators and students in higher education institutions, as well as among managers and employees, with a focus on sustainable plastic practices within the framework of a circular economy. It provides a comprehensive overview of the plastics lifecycle, from production to recycling, to foster awareness and responsibility. By incorporating digital technologies and innovative pedagogies, the project adapts established methodologies in plastic circularity to various educational settings. It also promotes equitable access to educational opportunities through online and remote learning, allowing trainers to teach without geographic limitations.

In addition, the project also supports the EU's digital transformation by:

- Developing innovative training methods and frameworks based on best educational practices.
- Providing open-access training materials, an e-learning platform, and upskilling opportunities for at least 200 learners.

3. GREEN SKILLS IN A CIRCULAR, CLIMATE-NEUTRAL ECONOMY

A circular economy is a system in which the value of products, materials, and resources is maintained in the economy for as long as possible while minimizing waste generation. It encompasses all stages of the value chain – from production and consumption to repair, remanufacturing, waste management, and the utilization of secondary raw materials. This model seeks to establish a sustainable, low-carbon, resource-efficient, and competitive economy by circulating materials in a manner analogous to the reuse, recycling, and recovery of water [1]. A climate-neutral economy refers to an economic system where overall activities don't harm the climate, aiming to achieve net-zero greenhouse gas emissions.

For the transition to a circular economy, green skills are essential. They include the technical expertise, knowledge, values, and attitudes necessary for green jobs that support a sustainable economy, society, and environment. These skills play a critical role in various industries, businesses, and communities, helping to prevent climate change and pollution [12]. Moreover, green skills are vital for reducing greenhouse gases and fostering sustainability, particularly as many industries have adopted eco-friendly practices to cut emissions [12]. The development and improvement of such green skills within various educational projects are essential for

advancing environmental sustainability, economic competitiveness, and social development in the future.

4. EXPECTED RESULTS OF THE PROJECT

Firstly, an analysis of existing training programs, curricula, courses, and syllabi will be conducted. This will result in a report compiling best practices from all partner countries. Based on this analysis and a gap analysis survey to evaluate the usefulness and knowledge of various topics, learning content will be developed. The topics are divided into five chapters, each containing 4 to 6 subchapters, including:

- Introduction to the Plastic World
- Plastic Waste Management
- Plastic in Circular Economy & Climate Neutral Economy
- Innovation in the Plastic World
- Awareness of Plastic Waste Impact & Responsible Behaviour

To implement and advance the developed learning content, the project will focus on several key activities:

- Develop innovative training methods tailored for staff, students, managers, and employees at higher education institutions, which will be compiled into a comprehensive handbook.
- Creating and making accessible training materials through online and mobile platforms, including a digital library, e-learning content, and an e-learning platform.
- Assessing the effectiveness of the learning methods, materials, and online/mobile learning platform. This phase will result in a tested e-learning platform, the delivery of both online and live courses, and training for 200 pilot learners.
- Ensuring the long-term sustainability and impact of the EDU4PlastiCircular training program by formulating a sustainability plan, and a post-project business model, and establishing future collaborations with partners, remote work companies, or public bodies through signed agreements and letters of cooperation.

Figure 3. EDU4PlastiCircular project website: https://microplastics.today/

The project will pilot the e-learning platform by integrating five training modules and enrolling 200 adult learners from various target groups, including HEI teachers, students, managers, and employees. The platform's effectiveness and the quality of the courses will be evaluated through learner feedback, which will be used to refine the courses and ensure their seamless integration into HEI e-learning systems and open educational resources (OER) platforms. Additionally, the project will include two Learning, Teaching, and Training Activities (LTTA) to upskill trainers. These face-to-face training events will prepare a total of 28 trainers, equipping them with the skills needed for the successful delivery of the newly developed e-learning content. An overview of the project is also available on our official website (Figure 3).

5. CONCLUSION

The EDU4PlastiCircular project is perfectly aligned with the Council Recommendation on Learning for the Green Transition, which was adopted in June 2022. This project will provide training opportunities for learners of all ages, with a strong emphasis on developing green skills and competencies within higher education institutions The Council's Recommendation urges Member States to integrate sustainability into all aspects of education and training, emphasizing the need for climate and sustainability education across both formal education (for example, schools and higher education) and non-formal education (such as extra-curricular activities, and youth work). It serves as a key policy statement supporting the goals of the European Green Deal [9,13].

Beyond its policy alignment, the EDU4PlastiCircular project delivers significant benefits to its target groups by equipping them with essential skills and resources for sustainable practices. Through activities such as gap analysis, best practice collection, and the creation of innovative training methodologies, the project provides participants with valuable knowledge about green jobs, materials, and technologies. The development of learning content, a digital library, and an e-handbook ensures that these resources are accessible, reusable, and adaptable, thereby empowering learners and institutions to integrate sustainability into their operations and promote green careers. The project is particularly significant in the context of managing plastic waste and mitigating its environmental impact. Plastics, especially microplastics, are widespread pollutants that damage ecosystems, wildlife, and human health. By offering education and training to individuals in higher education institutions, as well as managers and employees, EDU4PlastiCircular promotes sustainable practices that reduce plastic use, enhance waste management, and support the circular economy. This education is vital for developing solutions to the plastic crisis, fostering innovating in eco-friendly materials, and raising awareness about responsible plastic use.

Acknowledgment

The work presented in this paper was co-funded by the EU Erasmus+ project EDU4PlastiCircular: "Education for Plastics in a Circular and Climate Neutral Economy - Preventing Waste from Ending Up in the Environment" (Erasmus+ 2023-1-RO01-KA220-HED-000166242). The content of this paper and any related communication reflect the views of the authors alone, and the European Commission cannot be held responsible for any use made of the information provided herein.

Conflicts of Interest

The authors declare no conflict of interest.

6. REFERENCES

[1] B. Mrowiec, Plastics in the circular economy (CE), *Environmental Protection and Natural Resources*, 29 (2018) 4, pp. 16-19 https://doi.org/10.2478/oszn-2018-0017

[2] Plastic Europe, Plastics Europe launches Plastics – the fast Facts 2023, [Online]. Available: https://plasticseurope.org/media/plastics-europe-launches-the-plastics-the-fast-facts-2023/ [07. 08. 2024]

[3] R. Geyer, J. R. Jambeck, K. L. Law, Production, use, and fate of all plastics ever made, *Science Advances*, 3 (2017) 7, e1700782, https://doi.org/10.1126/sciadv.1700782

[4] K. Syberg, M. B. Nielsen, L. P. Westergaard Clausen, G. Van Calster, A. Van Wezel, C. Rochman, A. A. Koelmans, R. Cronin, S. Pahl, S. F. Hansen, Regulation of plastic from a circular economy perspective, *Current Opinion in Green and Sustainable Chemistry*, 29 (2021), 100462,https://doi.org/10.1016/j.cogsc.2021.100462

[5] J. Pichtel, M. E. Simpson, *Microplastics: Behavior, fate, and remediation.* Globe Pequot Publishing Group Inc/Bloomsbury, 2023, pp. 416.

[6] S. King, K. E. S. Locock, A circular economy framework for plastics: A semi-systematic review, *Journal of Cleaner Production*, 364 (2022), 132503. https://doi.org/10.1016/j.jclepro.2022.132503

[7] European Environment Agency, Plastics, the circular economy and Europe's environment – A priority for action. EEA Report 18/2020. Copenhagen, Denmark, 2021, pp. 76. https://www.eea.europa.eu/en/analysis/publications/plastics-the-circular-economy-and.

[8] European Environment Agency, Plastics, [Online], Available: https://www.eea.europa.eu/en/topics/in-depth/plastics [07. 08. 2024].

[9] European Commission, The European Green Deal (COM/2019/640 final), Brussels, Belgium, 2019. https://eur-lex.europa.eu/legal-content/EN/TXT/?uri=CELEX%3A52019DC0640&qid=1725443003845

[10] European Council. European Green Deal. [Online], 2024, https://www.consilium europa.eu/en/policies/green-deal/#what [13. 08. 2024].

[11] Microplastics.Today: EDU4PlastiCircular Project 2023, [Online] https://microplastics.today/ [22.08. 2024].

[12] Z. Ibrahim, C.S. Lai, A.F. Zaime, M.F. Lee, N.M. Othman, Green's skills in the knowledge and attitude dimensions from the industrial perspective. *IOP Conference Series: Materials Science and Engineering*, 917 (2020), 012025. https://doi.org/10.1088/1757-899X/917/1/012025

[13] European Commission, European Education Area. Learning for the green transition and sustainable development. [Online], https://education.ec.europa.eu/focus-topics/green-education/learning-for-the-green-transition [13. 08. 2024].